Acute and Chronic Volume Changes in Astrocytes

Inaugural-Dissertation

zur Erlangung des Doktorgrades
der Mathematisch-Naturwissenschaftlichen Fakultät
der Heinrich-Heine-Universität Düsseldorf

vorgelegt von

Eric Berlinger

aus Rastatt

Düsseldorf, März 2016

Aus dem Institut für Neurobiologie

der Heinrich-Heine-Universität Düsseldorf

Gedruckt mit der Genehmigung der

Mathematisch-Naturwissenschaftlichen Fakultät der

Heinrich-Heine-Universität Düsseldorf

Referentin: Prof. Dr. Christine R. Rose

Koreferent: Prof. Dr. Dieter Willbold

Tag der mündlichen Prüfung: 29.06.2016

Introductory Remarks

Parts of this doctoral thesis contain results from experiments carried out with hippocampal slice cultures of GFAP/GFP-expressing mice that have been published in:

Alexandra E. Schreiner, Eric Berlinger, Julia Langer, Karl W. Kafitz, and Christine R. Rose, "Lesion-induced alterations in astrocyte glutamate transporter expression and function in the hippocampus," ISRN Neurology, Vol. 2013, article ID 893605, 16 pages, 2013. doi:10.1155/2013/893605.

Abstract

The loss of the ability for volume regulation in astrocytes in the course a variety of pathologies, such as hepatic encephalopathy, leads to life-threatening cerebral edema. As in other cells, volume regulation in astrocytes is primarily based on the control of the intracellular and extracellular ion milieu, which predominantly determines the water content of the respective compartment. One part of this study was the establishment of a method for monitoring of acute volume changes in astrocytes, stained with the vital marker sulforhodamine 101, in hippocampal slices of mice by using confocal laser scanning microscopy. In this model system, astrocytes showed a significant reduction in cell volume under isotonic conditions during a period of six hours. Reducing or increasing the osmolarity of the extracellular saline caused a significant swelling or shrinkage of the cells, respectively. Swollen astrocytes reacted with regulatory volume decrease upon the osmotic challenge, while in shrunken astrocytes, no regulatory volume increase was observed. Volume changes induced by iso- and hypotonic conditions were prevented by inhibiting the Na^+-K^+-Cl^--Cotransporter 1 (NKCC1) with the loop diuretic bumetanide, indicating a substantial involvement of NKCC1 in volume maintenance and regulation. During addition of ammonium (5 mM), the reduction of astrocyte cell volumes under isotonic conditions was prevented. This might relate to the early phase of an NH_4^+-induced cell swelling. Chronic volume changes of astrocytes were studied using hippocampal slice cultures of mice expressing glial fibrillary acidic protein labelled with green fluorescent protein (GFAP/GFP). Following a mechanical lesion in the CA1 region, the size of astrocyte somata increased in direct proximity to the lesion site over an observation period of six days. This is indicative of a cellular hypertrophy and the development of a mild to severe reactive gliosis. In addition, a glial scar formed, which represents a cellular barrier consisting of hypertrophic astrocytes with overlapping cellular domains. Immunohistochemical staining for GFAP in fixed brain slices of transgenic mice over-expressing the Alzheimer´s disease-specific the human APP751 with the Aß dimer mutation Aß-S8C revealed no evidence for an elevated GFAP content. That indicates, that the neurotoxic dimer in this mouse model is not responsible for the development of reactive astrocytosis which can be found in brains suffering from Alzheimer´s disease. Taken together these results show that the method established here generally is suitable for the determination of acute, as well as chronic cellular volume changes in brain slices of murine brains. Furthermore these results indicate that the transporter NKCC1 is significantly involved in acute volume changes in astrocytes.

Zusammenfassung

Der Verlust der Fähigkeit von Astrozyten zur Volumenregulation im Verlauf verschiedenster Pathologien, wie z. B. der hepatischen Enzephalopathie, führt zu einem lebensbedrohlichen Hirnödem. Wie bei allen Zellen beruht die Volumenregulation bei Astrozyten auf der Kontrolle des intra- und extrazellulären Ionenmilieus und damit des Wasserhaushalts. In dieser Arbeit wurde eine Methode zur Messung von Volumenveränderung von mit Sulforhodamin 101 vital gefärbten Astrozyten in akuten Gehirnschnitten von Mäusen mittels konfokaler Laserscan-mikroskopie etabliert. In diesem Modellsystem zeigten Astrozyten unter isotonen Bedingungen eine signifikante Verminderung des Zellvolumens im Verlauf von sechs Stunden. Verminderung bzw. Erhöhung der Osmolarität der extrazellulären Blutersatzlösung führten zu einer signifikanten Schwellung bzw. Schrumpfung der Astrozyten. Geschwollene Zellen reagierten darauf mit regulatorischer Volumenabnahme, während bei geschrumpften Zellen eine regulatorische Volumenzunahme ausblieb. Diese akuten Volumenänderungen waren bei Hemmung des Na^+-K^+-Cl^-Cotransporters 1 (NKCC1) durch das Schleifendiuretikum Bumetanid unterdrückt, was auf eine maßgebliche Beteiligung des NKCC1 an der Aufrechterhaltung und Regulation des Zellvolumens schließen lässt. Die Verminderung des Zellvolumens unter isotonen Bedingungen war in Gegenwart von Ammonium (5 mM) unterbunden, worin sich möglicherweise die Frühphase einer Ammonium-induzierten Zellschwellung verbarg Chronische Volumenveränderungen wurden an hippokampalen Schnittkulturen von Mäusen, die mit „green fluorescent protein“ markiertes „glial fibrillary acidic protein“ exprimierten, analysiert Hier führte eine mechanische Läsion in der CA1-Region zu einer über sechs Tage anhaltenden Vergrößerung des Somas der Astrozyten, also einer chronischen zellulären Hypertrophie und der Entstehung einer milden bis schweren reaktiven Gliose. Zusätzlich entwickelte sich eine Glianarbe; eine zelluläre Barriere bestehend aus hypertrophen Astrozyten mit überlappenden Domänen in direkter Umgebung zur Schnittstelle. Die konfokal-fluoreszenzmikroskopische Untersuchung des immunhistochemischen GFAP-Färbemusters in fixierten Gehirnschnitten von transgenen Mäusen, die das Alzheimer-spezifische humane APP751 mit der Aß-Dimer Mutation Aß-S8C überexprimieren, ergab kein Anzeichen für die Erhöhung des GFAP-Gehaltes und somit keinen Hinweis für die Beteiligung dieses Dimers an der Entstehung einer reaktiven Astrozytose, wie sie in Gehirnen von Alzheimerpatienten gefunden werden kann. Zusammenfassend zeigen diese Methoden also, dass die hier etablierte Methode grundsätzlich zur Bestimmung akuter sowie chronischer zellulärer Volumenveränderungen in Hirnschnitten des Maushirns geeignet ist. Weiterhin weisen sie darauf hin, dass der Transporter NKCC1 maßgeblich an akuten Volumenveränderungen in Astrozyten beteiligt ist.

Contents

Abbreviations

aa	amino acids
Aß	amyloid ß protein
ACSF	artificial cerebrospinal fluid
AD	Alzheimer´s disease
ALF	acute liver failure
ANLSH	astrocyte neuronal lactate shuttle hypothesis
APP	amyloid precursor protein
AQP4	aquaporin-4 water channel
BBB	blood-brain barrier
CA1, 3	*Cornu ammonis,* Area 1, Area 3
Ca^{2+}	calcium ion
$CaCl_2$	calcium chloride
CaMKII	calcium/calmodulin-dependent protein kinase II
cAMP-PK	cAMP-dependent protein kinase (PKA)
CCC	cation chloride cotransporter
Cl^-	chloride ion
CLF	chronic liver failure
CNS	central nervous system
CO_2	carbon dioxide
DAPI	4´,6-diamidino-2-phenylidol
DG	dentate gyrus (lat. *Gyrus dentatus*)
DIV	days *in vitro*
DMEM	Dulbecco´s modified eagle medium
DNA	deoxyribonucleic acid
ECF	extracellular fluid
E_m	membrane potential
FHF	fulminant hepatic failure
GABA	γ-aminobutyric acid
GFAP	glial fibrillary acidic protein
GFP	green fluorescent protein

HEPES	N-(2-hydroxyethyl) piperazine-N′-2-ethanesulfonic acid
hf	hippocampal fissure
ICF	intracellular fluid
Il6	interleukin 6
ISF	interstitial fluid
JAK2	Janus Kinase 2
K^+	potassium ion
$K_{ir}4.1$	inwardly rectifying potassium channel 4.1
$K\text{-}MeSO_3$	potassium methane sulfonate
KCl	potassium chloride
Kv1.5	voltage-gated potassium channel 1.5
LTP	long-term potentiation
MAPK	mitogen activated protein kinase
MF	mossy fibers
Mg-ATP	magnesium adenosine triphosphate
$MgCl_2$	magnesium chloride
MIP	maximum intensity projection
mM	millimol (SI derived unit for concentration)
mOsm	milliosmol (non-SI unit, moles of solute adding to osmotic pressure)
n	number of analyzed cells
N	number of analyzed slices
Na^+	sodium ion
Na^+-K^+-pump	sodium-potassium pump
NaH_2PO_4	sodium dihydrogen phosphate
Na_3-GTP	sodium guanosine triphosphate
NaCl	sodium chloride
$NaHCO_3$	sodium hydrogen carbonate
NaOH	sodium hydroxide
NGS	normal goat serum
NH_3	ammonia
NH_4^+	ammonium
NH_4Cl	ammonium chloride

NO	nitric oxide
NOS	nitric oxide synthase
OAP	orthogonal arrays of particles
OHSC	organotypic hippocampal slice culture
OSR1	oxidative stress response kinase 1
PAG	phosphate-activated glutaminase
PBS	phosphate-buffered saline
PKA	protein kinase A
PKC	protein kinase C
PMT	photomultiplier tube
PP	perforant path
RGB	red-green-blue
ROS	reactive oxygen species
RT	room temperature
RVD	regulatory volume decrease
RVI	regulatory volume increase
S	*Subiculum*
S100ß	Ca^{2+} binding protein in astrocytes
SC	Schaffer collaterals
Slm	*stratum lacunosum moleculare*
SPAK	STE20/SPS-1-related, prolin-alanine-rich kinase
Sp	*stratum pyramidale*
SPM	synaptic plasticity and memory hypothesis
Sr	*stratum radiatum*
SR101	sulforhodamine 101
TBI	traumatic brain injury
TGF-β	transforming growth factor beta
Thr	threonine
TNF-α	tumor necrosis factor alpha
TM	transmembrane domain

1 Introduction

Life in the biological meaning is based on compartmentation, i.e the separation of biochemical reaction spaces by semipermeable phospholipid membranes which allow for selective passage of organic and anorganic substances, as it can be found in cells from the most primitive to the most highly developed forms of life. The higher developed the life-forms are, the more complex is the compartmentation, so that a eukaryotic cell consists of a cell membrane, which separates extra- from intracellular space, as well as various intracellular compartments, the so called organelles, with different specialized functions and properties. The active separation of ions and molecules between the extra- and intracellular space and between the different intracellular compartments results in concentration differences across the membranes and the establishment of osmotic and electrochemical gradients. These gradients then serve as driving forces for various cellular functions. Changes in the molecular compositions of the intra- and extracellular fluids, as they occur regularly in living systems due to cellular metabolism, the synthesis and degradation of proteins, transport processes, signaling events, and so on may lead to alterations of the osmolarity on one or both sides of the cell membrane. Although the dimensions of cells of the diverse organisms vary drastically, they all form an enclosed space and hence osmotic changes will lead to osmotic pressure, to whom cells are able to oppose merely limited resistance. Nonetheless evolution endowed cells with different strategies to react to such perturbations, for example via volume changes. However changes in cell volume need to be restricted and so the development of mechanisms for volume regulation was inevitable. Besides the formation and accumulation of organic osmolytes, directed ion and subsequent water movements serve the purpose to counteract osmotic pressure differences.

Ion movements in turn represent the basis for electrical excitability. All cell types are able to produce differences in the concentration of intra- and extracellular ion composition to establish membrane potentials, which nerve cells use to create action potentials through changes in permeability of their plasma membrane and subsequent ion currents. These processes are the basis for information transmission and processing in nervous systems. Vertebrates contain the main parts of their information processing structures, the central nervous system (CNS) mechanically protected within an osseous skull. Besides the advances of this arrangement, it is of essential significance to possess precise mechanisms for the regulation of the volume of the brain tissue, since disturbances of volume regulation lead to de- or increases in intracranial pressure. Such an increase can, when not dismantled immediately, lead to life threatening situations. So, swelling of brain tissue, a so called brain edema, is known to be a common harassment accompanying several pathological states of which some will be discussed here in more detail. Most of these pathologies are accompanied by a disturbance of memory what leads to the conclusion, that the development of brain edema also affects the hippocampus, a special brain region necessary for a proper memory function, amongst other things. Not least because of that the hippocampus and its cellular components and functions have become a coveted research object and is also used for this study.

The understanding of the cellular mechanisms, which underlie these pathologies, holds the key for the development of therapeutic approaches and in a final step hopefully to the preservation of human lives. Inasmuch the research into these cellular mechanisms needs to be performed in animal model systems, mammals, and especially rodents came in the focus of scientific interest due to their developmental affinity to human.

The study, which is presented here, therefore focuses on the hippocampus of mice and so the structure of this brain region, as well as its cellular components and functions will be described in the following chapter.

1.1 The hippocampus

This central part of the limbic system is itself a part of the median telencephalon. Phylogenetically relatively old and conserved, it depicts a bilaterally symmetric structure in both hemispheres of the mammalian brain (Amaral & Witter 1989). The term hippocampal formation comprises four cytoarchitectonically distinguishable regions (see Fig. 1.1): 1) the dentate gyrus (DG, *gyrus dentatus*), 2) hippocampus proper, with the subregions CA1, CA2, CA3 of the *cornu ammonis* (CA, lat.: ammon´s horn,), 3) the *subiculum* (S) complex and 4) the entorhinal cortex (EC). The hippocampal formation is found directly underneath the cortex in the rear area of the rodent brain. The appearance of the hippocampal formation can be described as a three dimensional “C-shaped elongated structure with its long-axis bending from the septal nuclei rostrodorsally to the temporal lobe caudoventrally” (Amaral & Witter 1989; Fig. 1.1 A). The anatomical structures of this formation are linked by an intrinsic connectivity that is an axonal connection between the prominent populations of neurons found within the different regions. These connections are classically referred to as the “trisynaptic excitatory circuit of the hippocampal formation” (Amaral & Witter 1989, Fig. 1.1 C). Beginning with the perforant path, which connects the entorhinal cortex with the granule cells of the dentate gyrus (1st synaptic connection; Fig. 1.1 C), the information flow is relayed further via the granule cell´s mossy fibers to the CA3 region of the hippocampus proper (2nd synaptic connection; Fig. 1.1 C). Axonal projections of the CA3 pyramidal neurons, the so-called Schaffer collaterals, then provide the major input to the dendrites of the CA1 pyramidal neurons in the *strata radiatum* and *lacunosum moleculare* (3rd synaptic connection; Fig. 1.1 C) and project to further regions septo-temporal in the three dimensional structure of the hippocampal formation outside the plane of the shown slice (indicated in Fig. 1.1 C, CA3 light blue pyramidal cells).

This circuitry served as a basis for the hypothesis of the lamellar organization, which argues that the hippocampal cortex is organized in parallel laminae, each of which contains the described circuitry that can operate individually with additional transverse information processing connections. These findings led to the development of the model system of hippocampal tissue slices and cultures, which preserve this circuitry and information processing properties (Anderson et al. 1971, Stoppini et al. 1991). Amaral (1993) later described additional connections within the hippocampal formation, thereby making the circuitry more complex. In fact, there are three fiber projections from the EC to the CA1 and 3 fields and to the subiculum. The connections between the CA regions are made of highly collateralized subsets of CA3 to CA1 projecting axons of pyramidal neurons (Schaffer collaterals), innervating CA1 subsets on their part, and there is also a projection from the CA1 region to the subiculum (Aamaral 1993; Fig. 1.1 B). This and the additional connections between the lamellae in this complex three-dimensional structure, the associational/commissural fibers, have been shown to be essential for the major functions of the hippocampal formation in mammals: explicit learning and memory consolidation. Thus, it has been shown that the hippocampal formation serves as a relay for the processing and consolidation of information, which is memorized in other brain areas (Lavenex et al. 2007).

In the mature mammalian CNS glutamate serves as the excitatory neurotransmitter in the hippocampus and acts through activation of AMPA and NMDA receptors in glutamatergic synapses. γ-amminobutyric acids (GABA) in contrast is the inhibitory neurotransmitter that conveys its depolarizing effect by activating GABA receptors (Lledo et al. 2006). Learning and memory consolidation not only require the ability for the transmission of incoming information, but also the ability to expand the transmitting structures. This can be observed, when the stimulation of the monosynaptic projections of the perforant path evokes a suprathreshold activation in pyramidal neurons, which is considered to be necessary to provide the information

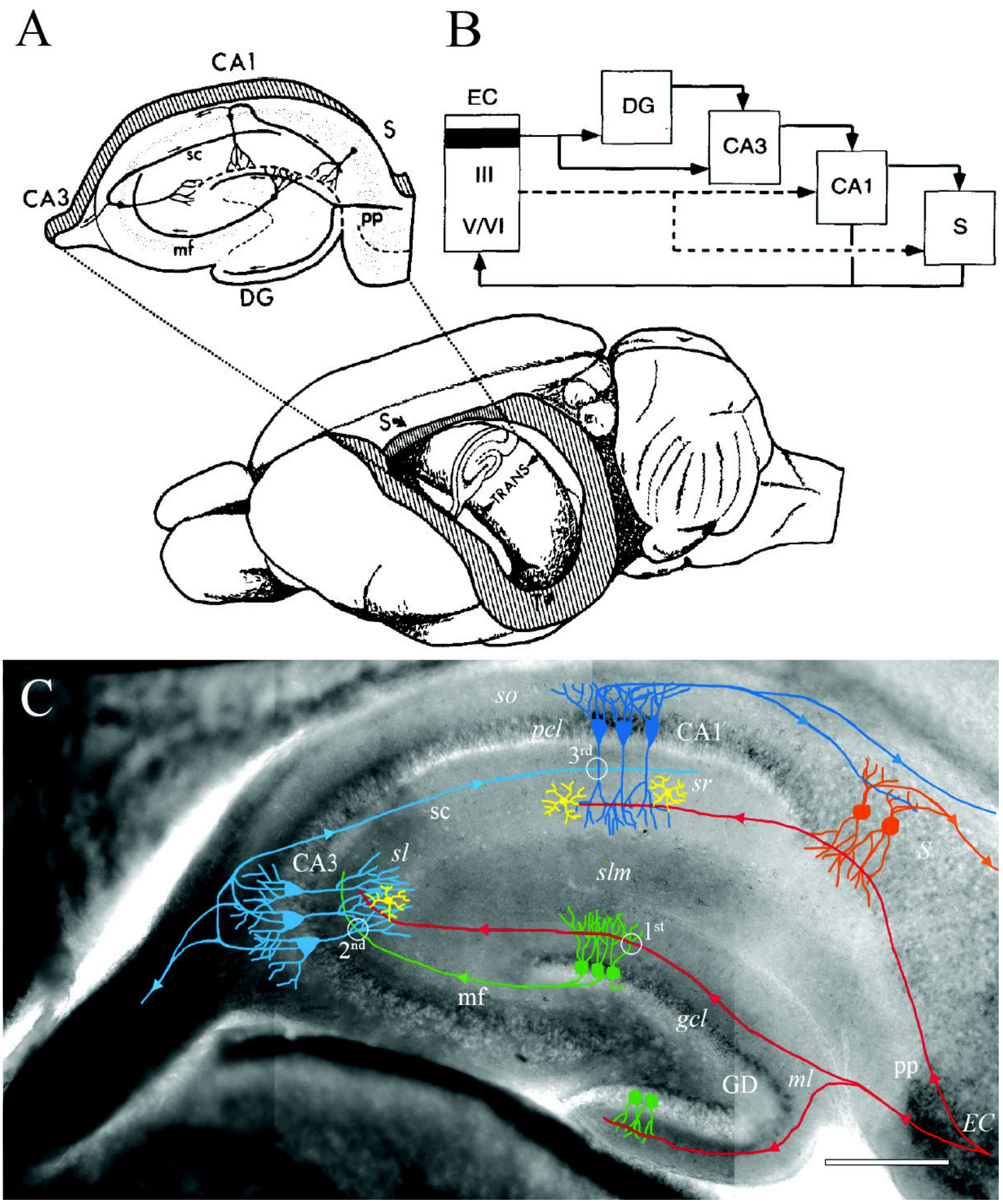

Figure 1.1**: Illustration of the intrinsic circuitry preserved within hippocampal slices. A)** Location of the hippocampal formation in the rodent brain and orientation of the slice plane of a lammelar hippocampal slice. Prominent regions and the connecting fiber pathways that form the trisynaptic excitatory circuitry of the hippocampal formation are illustrated (from Amaral & Witter 1989). **B)** Diagram of the information flow along the intrinsic connections within the circuitry. Main monosynaptical connection from DG to CA3, CA1 and S. Layer II of the EC projects to the GD and CA3. EC layer III projects to CA1 and S, from where a projection back to EC layers V/VI exists. (from Amaral 1993). **C)** Composite microscope image of an acute hippocampal slice, with illustration of the main neuronal connections. 1st, 2nd and 3rd show the synaptic connections of the circuitry (own image, Institute of Neurobiology, Düsseldorf). Green: granule cells, light blue CA3 pyramidal neurons, dark blue: CA3 pyramidal neurons, yellow: astrocytes. Scale bar: 250 µm; CA1,3: *cornu ammonis* region 1, 3, EC: entorhinal cortex, black bar: layer II, III, V/VI: EC layers, gcl: granule cell layer, GD: *gyrus dentatus* (dentate gyrus), mf: mossy fibers, ml: molecular layer, pcl: pyramidal cell layer, pp: perforanth pathway, S: *subiculum*, sc: Schaffer collaterals, sl: *stratum lacunosum*, slm: *stratum lacunosum -moleculare*, so: *stratum oriens*, sr: *stratum radiatum*.

flow to the hippocampus, *subiculum* and in other brain regions. The competence to strengthen and consolidate these pathways is thought to be essential therefore (Lledo et al. 2006). The underlying principle for these modifications is the so-called plasticity, i. e. the ability of the brain cells to adapt their structural and functional properties according to persisting repetitive stimuli (synaptic plasticity and memory (SPM) hypothesis): “Activity-dependent synaptic plasticity is induced at appropriate synapses during memory formation, and it is both necessary and sufficient for the information storage underlying the type of memory mediated by the brain area in which that plasticity is observed” (Martin et al. 2000, Neves et al. 2008).

The electrophysiological correlates for these processes necessary for information storage are the long term potentiation (LTP) and depression (LTD; Bear 1996, Goh & Vaughan 2013), defined through bidirectional plasticity of hippocampal synapses. High-frequency stimulation leads to NMDA receptor-mediated augmentation of AMPA receptor expression and activity, and thereby the potentiation of these synapses (LTP; Whithlock et al. 2006), whereas low frequency-induced LTD results in a decrease of the efficacy of AMPA receptors and the weakening of synaptic transmission (Neves 2008). Synaptic transmission can also be modified by astrocytes (Simard & Nedergaard 2004), which are representatives of the other prominent cell type and function within the nervous system, the glial cells.

A detailed description of astrocyte function will be presented in the following chapters. Inasmuch disturbances of function of the hippocampal formation lead to dramatic impairments of learning and memory tasks (Kandel, 1991), as they occur under pathological conditions such as hepatic encephalopathy or Alzheimer´s disease, the cellular components of the hippocampal formation are in the focus of this study.

1.2 Astrocytes

Besides neurons there exists another cell type in the CNS with distinct functions and properties, the so called glial cells or neuroglia. Glial cells outnumber neurons by up to 10 fold and are divided into micro- and macroglia. Microglia are of mesodermal origin and present the brain immune system. Macroglia derive from ectodermal tissue and can be subdivided into astrocytes, oligodendrocytes and Schwann cells (Simard & Nedergaard 2004). Astrocytes represent the numerous subpopulation among the glial cells, at least accounting for approximately one third of the brain mass (Kandel 1991). Astrocytes received their name due to their more or less star-like shaped morphology, but meanwhile it has been shown, that they show a highly heterogeneous morphology and functionality and can be found as protoplasmic and fibrous astrocytes in the grey and white matter of the CNS (Kimelberg 2010). Astrocytes form numerous processes that can contact the surface of the brain and spinal cord in a membrane-like manner (*glia limitans*); furthermore, they use their endfeet to ensheath blood vessels thereby participating in the formation of the blood-brain-barrier (BBB, Strange 1992), and they contact most (~60%) chemical synapses with their perisynaptic processes (Simard & Nedergaard 2004).

Astrocytes are directly involved in synaptic transmission, but by enclosing synaptic structures they are able to modulate and control synaptic activity (tripartite synapse concept; Perea et al. 2009). Astrocytes are responsible for the maintenance of ion homeostasis, water content and volume regulation in the brain, they control neurotransmitter metabolism and provide energy support to neurons (Simard & Nedergaard 2004, Kimelberg 2010, Verkhratsky et al. 2014). In several neurological diseases the observed pathologies could be ascribed to disturbances of the functional abilities of astrocytes. So far, astrocytic functions are of interest for this study and will therefore be described in the following.

1.2.1 Characteristics of astrocytes

Astrocytes contain high amounts of intermediate filaments, among them the glial fibrillary acidic protein (GFAP) which is commonly used as a histochemical marker for this cell type (Kimelberg 2010). The most prominent attribute of astrocytes is that they are electro-physiologically passive, i. e. they cannot generate action potentials (Kimelberg 2010). Astrocytes have a high membrane potential due to the high K^+ selectivity of their plasma membrane. They are coupled to neighboring astrocytes via gap junctions, made up of connexones, consisting of connexins 43 and 30, thereby forming a functional syncytium (Kimelberg 2010). This allows for the redistribution of K^+ from regions with high extracellular K^+ concentration, due to intense neural activity, to regions with low extracellular K^+ concentration (“spatial buffering”; Kofuji & Newman 2004).

Astrocytes express a set of amino acid transporters that enable the uptake of neurotransmitters, and hence the control of extracellular neurotransmitter concentration. They are also able to release neurotransmitters (gliotransmission; Halassa et al. 2007), which allows for a direct signaling to neurons. In addition, astrocytes participate in the neurovascular unit, coupling neuronal activity with local blood flow. Through their contact to blood vessels, they are able to mediate vasoconstriction and vasodilatation in reaction to neuronal activity by Ca^{2+}-triggered release of vasoactive substances (Koehler et al 2009). The direct contact to the brain vasculature leads to an additional function of astrocytes, the metabolic function and the astrocyte neuronal lactate shuttle hypothesis (ANLSH; Pellerin & Magistretti 2003). According to this hypothesis, astrocytes take up glucose from the blood stream via endothelial cells, convert it into lactate by glycolysis and transfer this energy substrate to neurons for metabolization via oxidative phosphorylation (Pellerin & Magistretti 2003). Additionally, glycogen granules can be found in astrocytes, serving as energy storage (Kimmelberg 2010). Finally, there is evidence for an antioxidant function of astrocytes, since they inhabit a number of antioxidant systems (Kimmelberg 2010). All these properties lead to a formulation of astrocyte characteristics and functions as it is described by the general support function theory (Kimelberg 2010). In this study, astrocytes were identified either via the red fluorescent dye sulforhodamine 101 (SR101), which specifically labels vital astrocytes (Nimmerjahn et al. 2004, Kafitz et al. 2008), or via immunoreactive fluorescence for GFAP and S100ß, an additional marker for mature astrocytes (Raponi 2007; Fig 1.2). Here, the mechanisms of ion homeostasis in the brain and volume regulation in astrocytes, as well as the role of astrocytes in the development of reactive gliosis and the pathological states of hepatic encephalopathy and Alzheimer´s disease are of further interest and will be discussed below.

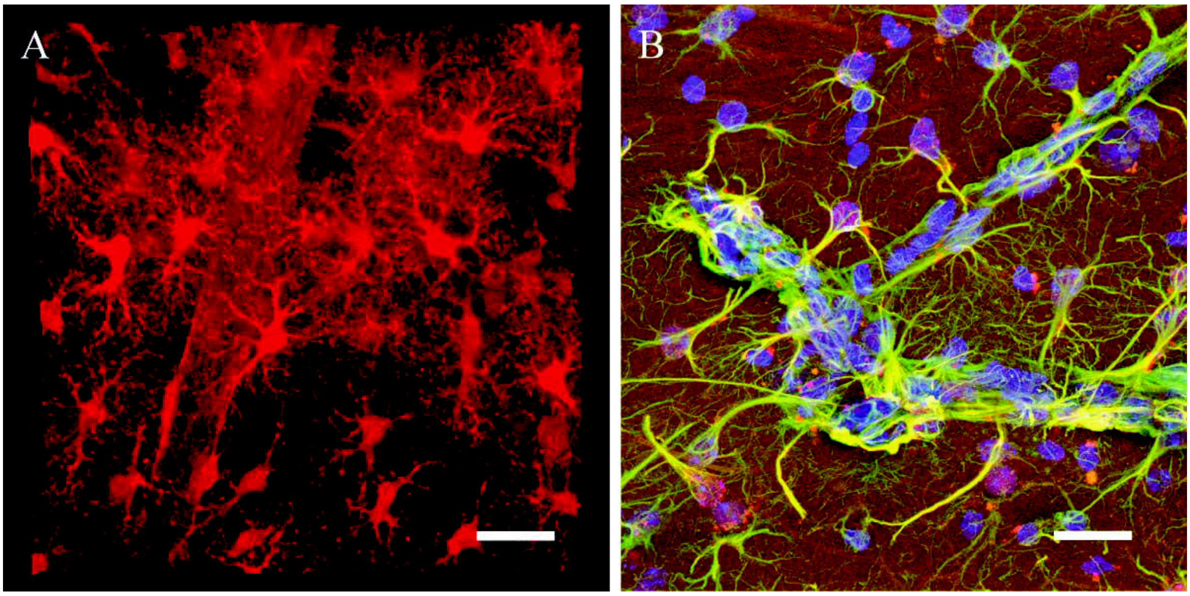

Figure 1.2: **Labelling of astrocytes in the *stratum radiatum* of the rodent hippocampus A)** Sulforhodamin 101 vital staining, revealing astrocyte morphology in an acute brain slice **B)** Immunoreactive fluorescence for GFAP (green), S100ß (red) and DAPI (blue). A dense meshwork of GFAP intermediate filaments and S100ß-containing astrocytes contacting branching capillaries can be seen here. Colocalization of GFAP and S100ß immunefluorescence appear as yellow structures, S100ß- and DAPI-stained nuclei of astrocytes appear in orange. DAPI stained nuclei (blue) within the capillary lumen belong to epithelial cells. Scale bar: 300 µm. [own image, Institute of Neurobiology, Düsseldorf]

1.2.2 Ion homeostasis and volume regulation

Neuronal function is based on ion movements, primarily of Na^+ and K^+ across the cell membrane. Essential for the function of neurons is that the extracellular K^+ concentration is maintained at $[K^+]_e$ of ~2.5 mM (Kofuji & Newman 2009, Deitmer & Rose 2010), and glial cells, especially astrocytes serve this purpose. The theory of "spatial buffering" describes the ability of the astrocyte network to take up excessive K^+ flooded into extracellular space during neuronal activity and redistribute it intracellularly via gap junctions throughout the syncytium into regions with low $[K^+]_e$ or via perivascular connections into the blood lumen (Simard & Nedergaard 2004). A set of transporters and channels located in the membrane of astrocytes were identified as participants in that process. The uptake is predominantly mediated by inwardly rectifying K^+ channels (K_{ir} 4.1; Simard & Nedergaard 2004) and K_{ir}4.1 has been identified in brain astrocytes to be located close to synapses or blood vessels (Higashi et al. 2001, Simard & Nedergaard 2004).

A further type of K^+ channel, presumably also involved in K^+ spatial buffering, is the so called rSlo Ca^{2+}-activated K^+ channel. Located in the perivascular endfeet of astrocytes, this channel type can be activated through depolarization of the cell membrane and an increase in $[Ca^{2+}]_i$ (Price et al. 2002, Simard & Nedergaard 2004). Finally, also voltage-gated K^+ channel, called Kv1.5, have been identified in the perivascular end-feet (Roy et al. 1996, Simard & Nedergaard 2004). The Kv 1.5 channels are also able to drain excess K^+ to the vasculature via swelling-activated K^+ currents that occur upon regulatory volume decrease (RVD; Simard & Nedergaard 2004).

Active transport mechanisms participating in the maintenance of $[K^+]_e$ are represented by the Na^+-K^+-ATPase that uses ATP to transport K^+ in exchange to Na^+ into the cell. Cotransport, combining Na^+, K^+ and Cl^- transport into the cell via the activity of the NKCC1 represents a further mechanism for ion homeostasis (Chen & Sun 2005) and is described in more detail in the next chapter.

Na^+ homeostasis is also essential for control of the intra- and extracellular ion milieu by astrocytes. The $Na^{+-}K^+$-ATPase needs to be adequately supplied with Na^+ to fulfil its role in K^+ homeostasis. To secure this, astrocytes express, despite their electrophysiological passiveness, voltage-gated Na^+ channels, which facilitate the influx of Na^+ to maintain $[Na^+]_i$ high enough for $Na^{+-}K^+$-ATPase activity, which is then exported by the ATPase in exchange for K^+ in spatial buffering (Sontheimer 1992, Simard & Nedergaard 2004). The Na^+-K^+-ATPase generates an in inwardly directed gradient for Na^+, with $[Na]_e$ ~145 mM and $[Na]_i$ = 8-15 mM (Rose 1997, Deitmer & Rose 2010), which delivers the driving force for additional secondary transport, such as Na^+-Ca^{2+}-exchange (Rose et al. 1998), Na^+-K^+-Cl^- cotransport (Chen & Sun 2005) or H^+/Na^+ antiport (Simard & Nedergaard 2004).

The intracellular Cl^- concentration in astrocytes can vary between 20 and 60 mM (Walz 1995, Ben-Ari et al. 2007, Deitmer & Rose 2010) and there are several routes for Cl^- to pass the cell membrane. The most important are inwardly or outwardly rectifying anion channels, Cl^-/HCO_3^- exchanger, and swell-activated Cl^- channels, the latter mediating outward Cl^- current during RVD (Simard & Nedergaard 2004).

Astrocytes regulate their intracellular pH in between 7.0 and 7.4, which is close to the extracellular pH of 7.1 to 7.3 in the CNS tissue. Due to the negative membrane potential, protons tend to flow into the cytoplasm and to cause an acidification (Deitmer & Rose 2010). In order to maintain the intracellular pH, astrocytes express a set of membrane transporters to extrude H^+. The most important are the H^+/Na^+ exchanger, Na^+/HCO_3^- cotransporter and Cl^-/HCO_3^- antiporters, which can be Na^+-dependent or Na^+-independent (Deitmer & Rose 1996, Brookes 1997, Simard & Nedergaard 2004). HCO_3^- gains importance for pH regulation, since H^+/HCO_3^- and CO_2, of which the latter is mainly produced by neurons being the main consumers of ATP, are reversibly converted ($CO_2 + H_2O \leftrightarrow HCO_3^- + H^+$) by carbonic anhydrase, functioning as the so called CO_2/HCO_3^- buffer system (Simard & Nedergaard 2004, Deitmer & Rose 2010). The extrusion mechanisms for H^+ and HCO_3^- then are linked to the homeostasis mechanisms for Na^+ and Cl^-, represented by the H^+/Na^+-antiport and the Cl^-/HCO_3^- exchanger (Simard & Nedergaard 2004; Fig. 1.3).

Relevant for the ability of astrocytes to maintain ion homeostasis is their sensitivity to detect alterations in intra- and extracellular osmolarity (Pasantes-Morales 1996, Pasantes-Morales et al. 2000). Challenged by hypoosmolarity, astrocytes react with a fast increase of cell volume that is followed by a volume reduction process, RVD (Strange 1992, Simard & Nedergaard 2004). It has been shown that buffering of excess K^+ via uptake leads to a decrease of the osmolarity of the extracellular space (Dietzel et al. 1980, 1989, Simard & Nedergaard 2004).

Nagelhus et al. (1999) showed that in rat Müller cells K^+ and water transport were linked to the co-existence of $K_{ir}4.1$ channels and AQP4, a tetrameric water channel, in close proximity (Amiry-Moghaddam et al. 2003, Simard & Nedergaard 2004). AQP4 is also present in astrocytic endfeet, which contact the vasculature (Nielsen et al. 1997, Simard et al 2003, Furman et al. 2003, Simard & Nedergaard 2004), where it is arranged in large groups called orthogonal arrays of particles (OAP; Nagelhus & Ottersen 2013, Thrane et al. 2014).

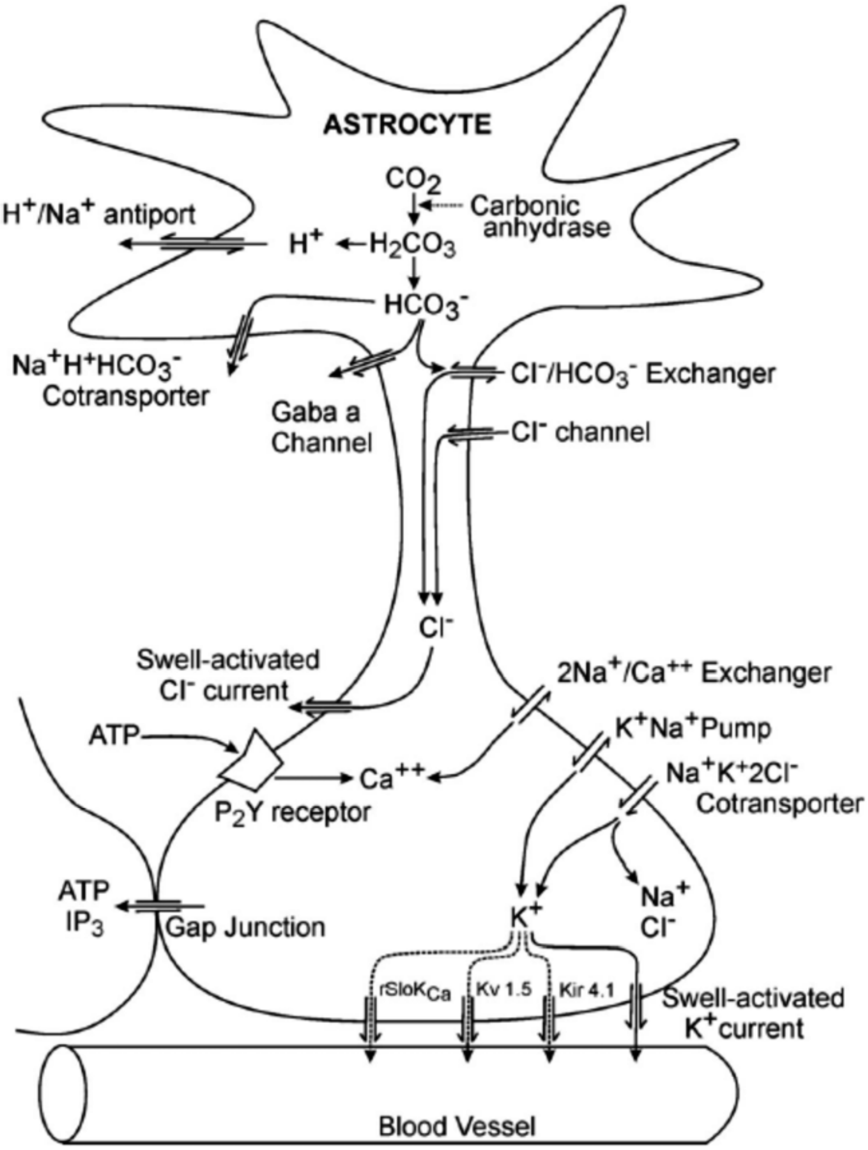

Figure1.3: **Ion homeostasis in astrocytes.** Overview of the main transport processes involved in ion homeostasis and volume regulation in astrocytes. While transporters like H^+/Na^+ antiport, Na^+/HCO_3^- cotransporter and Cl^-/HCO_3^- antiport are located in the soma region, others, like swell-activated mechanisms, transporters for K^+ buffering and siphoning into the blood lumen and gap junctions for the interconnection of astrocytes are found in the fine processes and endfeet that contact the vasculature. For further explanation see text. [From Simard & Nedergaard 2004]

Astrocytes are essential for the regulation of water movements and interstitial fluid turnover between the compartments of the brain, since deletion of the AQP4 channel resulted in a more than 60% reduction of solute movement (Amiry-Moghaddam et al.2003, Simard & Nedergaard 2004, Iliff 2012, Thrane et al 2014). AQP4 channels control bidirectional rapid transmembrane water movements, which is following osmotic gradients. Disturbances of the cellular and molecular mechanisms of cell volume control thus may lead to the development of brain edema, representing an net accumulation of water in brain tissue (Amiry-Moghaddam & Ottersen 2003, Simard & Nedergaard 2004), what is confirmed by data, showing that knockout of AQP4 resulted in an decrease in swelling of astrocytes upon hypoosmotic perturbations (Manley et al. 2000, Simard & Nedergaard 2004).

But the transport of water in the brain is not only addressed to aquaporins, also cotransporters, like NKCC might be involved in water movement (Amiry-Moghaddam & Ottersen 2003) Recent findings emphasize the importance for electroneutral ion cotransporters, with NKCC1 in first place, for the regulation of water transport (Chen & Sun 2005, Simard & Nedergaard 2004) and subsequence impact in the development of brain edema in several pathologies, Kahle et al. 2009, Jayakumar & Norenberg 2010, Kelly & Rose 2010, Thrane et al 2014).

1.2.3 The Na^+-K^+-Cl^- cotransporter 1 and its role in volume regulation

The Na^+-K^+-Cl^- cotransporter (NKCC) is a member of the SLC12 gene family of cation-chloride cotransporters (CCC). It transports Na^+ and K^+ together with Cl^- electroneutrally into cells, with a stoichiometry of 1:1:2 (Haas & Forbush 2000). There are two NKCC isoforms, NKCC1 and NKCC2. NKCC2 is expressed in the kidney, specifically in the apical membrane of the thick ascending limb of Henle´s loop, while NKCC1 can be found in most other cell types, especially in astrocytes, where it functions in ion homeostasis and cell volume regulation (Haas & Forbush 2000, Russel 2000, Chen & Sun 2005). NKCC1 consists of ~1200 amino acids (aa) and forms 12 transmembrane domains (TM 1-12); it has potential N-linked extracellular glycosylation sites between TM 7 and 8 and large intracellular amino and carboxy termini, containing four threonine phosphorylation sites (Payne et al. 1995, Russel 2000; Fig. 1.4).

The inwardly directed Na^+ gradient represents the main driving force, and an additional driving force is delivered by the Cl^- gradient, at least in some secretory epithelial cells. The binding

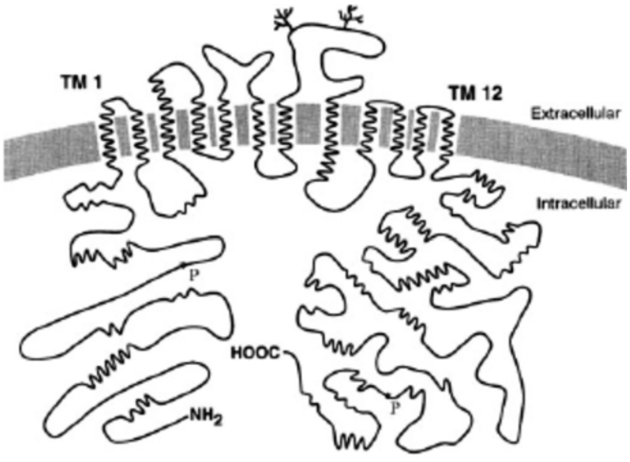

Figure 1.4: **Hydropathy-based model of Na^+-K^+-Cl^- cotransporter isoform 1 (NKCC1).** The NKCC1 protein consists of about 1200 amino acids and contains 12 transmembrane domains (TM1-12). Extracellular glycolysation sites are indicated between TM 7 and TM 8; P marks intracellular threonine phosphorylation sites Thr^{184}, Thr^{189}, Thr^{202} and Thr^{1114}. For further explanation see text. [From Chen & Sun 2005]

sites for Na^+ and K^+ are supposed to be located in TM 2 and the two binding sites for Cl^- between TM 4-7. One of the binding sides for Cl^- is the target for the sulfamoylbenzoic acid loop diuretic bumetanide, the most potent NKCC1 inhibitor. Site-directed mutagenesis studies could show that NKCC1 affinity for bumetanide is affected by the replacement of ammino acids in TM 2-7 as well as TM 11 and 12 (Haas & Forbush 2000, Russel 2000, Chen & Sun 2005; Fig. 1.4). Among the stimuli that activate NKCC are hypertonic stress, decrease in intracellular Cl^-, increase in intracellular Ca^{2+}, cytoskeletal reorganization, receptor activation, and various hormones (Payne et al. 1995, Russel 2000, Chen & Sun 2005, Kahle et al. 2009, Jayakumar & Norenberg 2010). Factors involved in the regulation of NKCC1 activity are supposed to be oxidative and nitrosative stress, increases in protein expression, and phosphorylation. The activation of NKCC1 by oxidation and nitration in cultured astrocytes has been demonstrated by applying the oxidant H_2O_2 and nitric oxide (NO) donors, whose effects were significantly diminished by antioxidants and NO synthase (NOS) inhibitors (Jayakumar et al. 2008a). Ammonia treatment promotes the formation of free radicals (Murthy et al. 2001, Ramao Rao et al. 2003), also resulted in the oxidation and nitration of NKCC1 and hence its activation (Jayakumar et al. 2008a, Jayakumar & Norenberg 2010).

Activation of NKCC1 via phosphorylation has been shown to be due to its increased membrane translocation (Gimenez & Forebush 2003, Jayakumar & Norenberg 2010; Fig. 1.5), which occurs in response to cell shrinkage (Lytle & Forbush 1992, Klein et al. 1993, Di Ciano-Oliveira et al. 2003), ischemia (O´Donnel et al. 2006, Abbruscato et al. 2004), and ammonia toxicity, (Kurihara et al. 1999, Jayakumar et al. 2008a, Jayakumar & Norenberg 2010). A set of kinases responsible for NKCC1 phosphorylation has been identified, including the oxidative stress response kinase (OSR1) and STE20/SPS-1 related, prolin-alanine-rich kinase (SPAK, Piechotta et al. 2003, Moriguchi et al. 2005, Flatman 2008), which both function as serine/

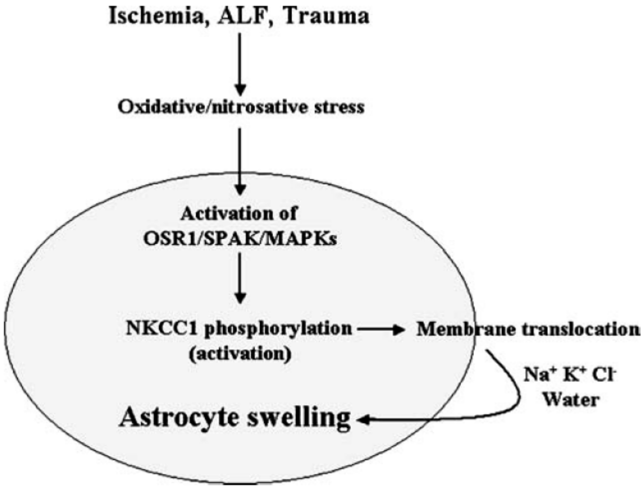

Figure 1.5**: Mechanisms of NKCC1 activation induced astrocyte swelling.** Various pathological conditions (ischemia, liver failure, traumatic brain injuries) lead to oxidative stress, resulting in phosphorylation and activation of NKCC1 by various kinases. Phosphorylation of NKCC1 leads to its membrane translocation, what causes the increased import of Na^+, K^+ and Cl^- together with water into the astrocyte, resulting in cell swelling. For further explanation see text. [From Jayakumar & Norenberg 2010]

threonine kinases and can themselves be activated through phosphorylation (Gagnon et al. 2006a, 2006b, Vitari et al. 2005, Jayakumar & Norenberg 2010). Mitogen-activated protein kinases (MAPKs, Wong et al. 2001, Piechotta et al. 2003, Andersen et al. 2004), the protein kinases A and C (PKA, PKC, Diecke et al. 2005), and calcium/calmodulin-dependent protein kinase II (CaMKII, Akimova et al. 2006) also contribute to the phosphorylation-induced activation of NKCC1, as do Rho (Di Ciano-Oliveira et al. 2003), Janus kinase 2 (JAK2, Selvaraj et al. 2000), cAMP-PK (Pewitt et al. 1990) and myosin light chain kinase (Jayakumar & Norenberg 2010). Ammonia treatment lead to the activation of MAPKs and CaMKII in astrocyte cultures (Jayakumar et al. 2008a), and additional treatment with oxidants and NO donors resulted in a significant increase in NKCC1 activation (Jayakumar & Norenberg 2010). Several lines of evidence link the activation of NKCC1 with the swelling of astrocytes and the development of brain edema under various pathophysiological circumstances. Among these are ischemic insults, and of special interest for this work, traumatic brain injuries (TBI) and hyperammonemia caused by acute liver failure (ALF).

1.3 Volume changes in astrocytes in hepatic encephalopathy

Since acute or chronic liver failure (ALF, CLF), as well as fulminant hepatic failure (FHF) lead to severe, and in many cases lethal brain edema (Schiodt et al. 1999), the cellular and molecular mechanisms of ammonia-induced brain swelling and the role of astrocyte volume regulation mechanisms came into the focus of interest in order to find a target for the development of treatments for this pathologic condition (Blei et al. 1994).

Ammonium (NH_4^+) is a generated in the course of amino acid degradation has either to be reintegrated into freshly synthesized substances or needs to be detoxified. Detoxification usually takes place in the urea cycle in hepatocytes, but if this process is disturbed, as in liver failure caused for example by alcohol abuse or an infection with hepatitis C, blood levels of NH_4^+ in Patients with ALF can increase from 0.05–0.1 mM to 0.3–0.5 mM (hyperammonemia, Clemmesen et al. 1999). Since NH_4^+ is able to pass the blood-brain-barrier (Ott & Larsen 2004), this leads to a massive elevation of NH_4^+ in brain tissue. An elevation of NH_4^+ to up to 5 mM could have been measured in the brain tissue of rats with induced ALF (Swain et al. 1992).

Here, NH_4^+ drastically hampers the ability of the astrocyte for ion homeostasis and volume regulation (Jayakumar & Norenberg 2010) as well as the glutamate and energy metabolism, leading to astrocyte swelling and the development of life threatening brain edema (Jayakumar et al. 2006, Stephan 2011).

Due to its positive charge, $NH_4^+$is not able to diffuse through the lipid bilayer of the plasma membrane. However, the ion radius of NH_4^+ is similar to that of K^+, which allows NH_4^+ to compete with K^+ to be imported via channels (Hille 1973, Latorre & Miller 1983, Allert et al. 1998, Nagaraja & Brookes 1998) and transporters (Yan et al. 2001, Bergeron et al. 2003, Titz et al. 2006, Kelly et al. 2009, Stephan, 2011). Ammonium import into astrocytes is mainly caused by the activity of the NKCC1 and the Na^+-K^+-pump (Kelly & Rose 2010; Fig 1.6), but an entrance via additional cation-chloride cotransport mechanisms, K^+-channels and aquaporins (Holm et al. 2005) or glycoproteins (Huang & Ye 2010) has also be taken into consideration (Kelly & Rose 2010).

NH_4^+ causes an increase in extracellular K^+ concentration, due to a loss of intracellular K^+ (Alger & Nicoll 1983, Benjamin et al. 1978, Stephan 2011). In addition NH_4^+ evokes an intracellular acidification in astrocytes caused by the release of H^+ during the conversion of NH_4^+ into NH_3, as well as an intracellular accumulation of Na^+ caused by bumetanide-inhibitable activity (Kelly & Rose 2010). The elevation of $[Na^+]_i$ then means a reduction of the inward driving force for Na^+, which contributes to the impairment of ion homeostasis observed during HE. As described before, the NKCC1 plays a critical role in the pathology of HE, since its activation or respectively increase in expression is responsible for the increase in $[Na^+]_i$, which contribute to the increase in cell volume of cultured astrocytes after 24h of NH_4^+ treatment (Jayakumar et al. 2008, Kelly & Rose 2010), but also within minutes (Alvarez-Leefmans et al. 2006, Reinehr et al. 2007, Kelly & Rose 2010). Even for this rapid volume increase an increase in $[Na^+]_i$ might be a possible explanation (Dierkes et al. 2006, Kelly et al. 2009, Kelly & Rose 2010).

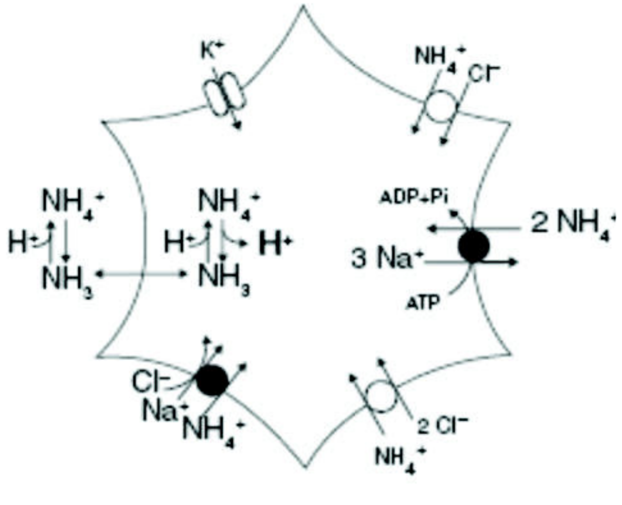

Figure 1.6: **NH_4^+/NH_3 influx pathways in astrocytes.** Influx is predominantly by NKCC1 and the Na^+-K^+-ATPase, but may also be possible via K^+ channels and Cl^--dependent and Cl^--independent mechanisms. For further explanation see text. [From Kelly & Rose 2010]

It has been suggested that astrocytes, as a part of the blood-brain-barrier are responsible for the import of NH_4^+ (Ott & Larsen 2004). Since their endfeet, which contact the vasculature, contain NKCC1 (Yan et al. 2001), it has been proposed that this transport system is one possible mechanism for NH_4^+ uptake (Ngarya & Brookes 19989, Ott & Larsen 2004).

It has also been shown that astrocytes are responsible for NH_4^+ detoxification (Cooper et al. 1979). NH_4^+ is incorporated into previously released glutamate by glutamine synthethase (GS) after the reuptake by astrocytes, yielding glutamine at the expense of ATP. This reaction is part of the glutamine-glutamate-cycle, which describes the recycling of glutamate released into the synaptic cleft upon neuronal activity. Using the Na^+ gradient as a driving force, excess glutamate is transported back into the intracellular compartment of neurons, but also into astrocytes via specific glutamate transporters, where the conversion to glutamine through ATP consumption and NH_4^+ incorporation takes place. Glutamine is, in first place, transferred back to the presynaptic terminals of neurons, where the phosphate-activated glutaminase (PAG) hydrolyzes glutamine into NH_4^+ and glutamate, which is again used for synaptic transmission (Bak et al. 2006).

Under hyperammonic conditions, the balance of the glutamine-glutamate-cycle is disturbed, leading to an increase in glutamine and a decrease in glutamate concentrations (Lavoie et al. 1987, Swain et al. 1992a, Kosenko et al. 1993, Ratnakumari et al. 1994, Blei et al. 1994, Stephan 2011). Additionally, it has been described, that increased NH_4^+ levels cannot be detoxified due to an exceedance of the synthesis capacity of GS, which it is already working near its maximum under physiological conditions (Felipo & Butterworth 2002, Stephan 2011). Glutamine hydrolysis by PAG also takes place in the mitochondria of astrocytes. The hypothesis of the "Trojan horse" describes the sequence of events, by which the hydrolyzation of glutamine results in the production of toxic amounts of NH_4^+ in the mitochondrial matrix, leading to oxidative and nitrosative stress and the so called mitochondria permeability transition (MPT, Rama Rao & Norenberg 2014). These processes are supposed to contribute, beside the increase in $[Na^+]_i$, and subsequent NKCC1 activation, to the NH_4^+-induced astrocyte swelling (Jayakumar et al. 2006, Kelly & Rose 2010, Rama Rao & Norenberg 2014). Although the exact mechanisms leading to HE-induced brain edema still need to be elucidated, the processes described above can give an idea, how complex the mechanisms might be.

1.4 Astrocyte reactivity and the development of astrogliosis

The term reactive astrogliosis describes the ability of astrocytes to perform marked morphological and physiological changes in reaction to various pathological stimuli (Eddleston & Mucke 1993, Correa-Cerro & Mandell 2007), i.e. infections, ischemia, traumatic brain injuries (TBI, Pekny & Nilsson 2005) and neuro-degenerative diseases, such as Alzheimer´s disease (AD; Sofroniew 2005, Maragakis & Rothstein 2006, Sofroniew 2009, Verkhratsky et al. 2010).

Reactive astrogliosis can be observed in various model systems *in vitro* as well as *in vivo* (Ridet et al 1997, Sofroniew 2009), showing as major hallmarks a cellular hypertrophy, described as a significant increase in cell volume at the soma level, as well as a tremendous increase in the expression of GFAP (Pekny & Nielson 2005, Sofroniew 2009, Middeldorp & Hol 2011, Schreiner et al. 2013). The more severe the insults become, the more reactive astrogliosis results in the formation of a glial scar (Ridetet al. 1997, Sofroniew 2009, Kawano, Kimura-Kuroda et al. 2012, Schreiner et al. 2013). In contrast to the previous opinion of having negative consequences for cells and tissue, there is now evidence that astrocyte reactivity is in most cases a protective and reparative response of astrocytes in reaction to injuries and inflammation within the CNS (Sofroniew 2009).

If insults are less severe, astrocytes exhibit a mild astrogliosis, which is characterized by a cellular hypertrophy, i.e. an increase in soma size. In addition, changes in the expression and physiological functions of proteins can be observed, for example the upregulation of structural components like GFAP, vimentin and nestin (Eddleston & Mucke 1993, Pekny & Nilsson 2005, Sofroniew 2009). Transcriptional factors like NFκB (Brambilla et al. 2005), STAT3 (Herrmann et al. 2008) and the second messenger cAMP are also upregulated (Sofroniew 2009). And changes in AQP4 content and the expression of Na^+/K^+ transport mechanisms (Simard & Nedergaard 2004, Zador et al. 2009), responsible for water and ion homeostasis, on which lies a special interest here, have been reported (Sofroniew 2009).

Also changes in glutamate transporter regulation (Rothstein et al. 1996, Maragakis & Rothstein 2006, Sofroniew 2009, Schreiner et al. 2013), energy supply via lactate (Pellerin et al. 2007, Sofroniew 2009), gap junction proteins (Retamal et al. 2007, Sofroniew 2009), extracellular matrix and cell-cell interactions (Silver & Miller 2004, Gris et al. 2007, Wanner et al. 2008, Hsu et al. 2008, Sofroniew 2009), synapse formation and remodeling (Christopherson et al. 2005, Stevens 2007, Sofroniew 2009), and inflammatory cell regulators (Eddleston & Mucke

1993, Chen et al. 2001, Gris et al. 2007, Sofroniew 2009) have been reported to occur in the course of mild astrogliosis. Although these are quite complex processes, most changes are reversed when the triggering stimulus disappears (Sofroniew 2009).

With increasing severity and duration of the incident, as it is the case of a mechanical lesion, the development and persistence of a glial scar, in direct proximity of the site of tissue damage can be observed. This scar consists of proliferated hypertrophic astrocytes with overlapping cellular domains, and other cell types, bordering along the sites of the tissue damage (Sofroniew

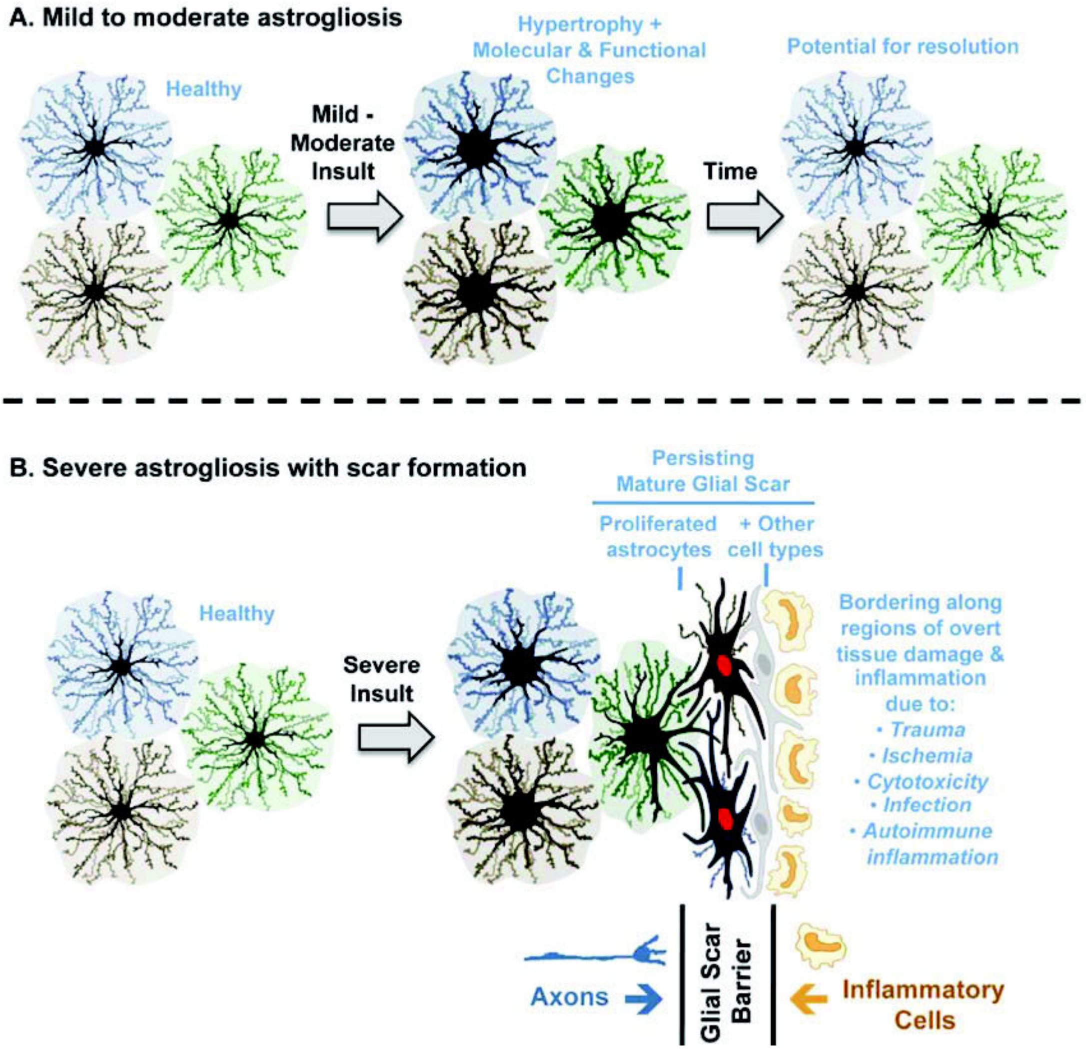

Figure 1.7: **Schematic representations of different gradations of reactive astrogliosis. A)** Mild to moderate insults result in mild to moderate astrogliosis that is characterized by cellular hypertrophy, accompanied by changes in molecular composition or functional activity. The more severe the insult is, the more severe are these changes, including a moderate tendency for overlapping of astrocytic domains. When the pathological stimulus disappears, retrogression to healthy morphology and physiology is possible. **B)** The more severe the insult is, the more severe is the reactive gliosis, including hypertrophy, molecular rearrangements and the formation of a dense glial scar in the direct proximity of the site of the insult. Astrocytes in direct proximity to the lesion tend to exhibit overlapping processes. Proliferated cells can be found here (red nuclei). Persistent glial scars prevent axon regeneration, but also serve to protect healthy tissue more distant to the lesion site. [From Sofroniew 2009]

2009; Fig. 1.7). Then astrocytes not only exhibit an enlargement of cell soma and increased GFAP expression (Schreiner et al. 2013), amongst other phenomena mentioned above, but also display a marked morphological and physiological reorganization, accompanied with a partial reentrance into the cell cycle and proliferation (Sofroniew 2009, Schreiner et al. 2013; Fig. 1.7). The scar together with the population of reactive astrocytes surrounding the lesion site is regarded as a protective and regeneration-supporting reaction, although the obviation of axon growth gives a negative connotation to the function of reactive astrogliosis (Sofroniew 2009). With increasing distance to the lesion site and the scarred tissue, the less severe are the hypertrophy and the morphological changes of astrocytes (Schreiner et al. 2013). Several molecular mediators that are released by neurons and glial cells in reaction to certain types of pathological stimuli could have been identified as triggers the development of a reactive astrogliosis. These are cytokines and growth factors, like Il6, TGFß and TNFα (John 2003, Di Giorgio 2007, Sofroniew 2009), neurotransmitters like glutamate and noradrenalin (Bekar et al. 2008, Sofroniew 2009), ATP that is released upon cell injury (Neary et al. 2003, Sofroniew 2009), mediators of oxidative stress like NO and reactive oxygen species (Sofroniew 2009), putative toxic molecules like NH_4^+ (Norenberg et al. 2009, Sofroniew 2009), and also the Alzheimer's disease-related amyloid-beta (Maragakis & Rothstein 2006, Simpson et al. 2008, Sofroniew 2009), both of which play a prominent role, as far as this study is concerned.

1.5 The role of astrocytes in Alzheimer´s disease

Astrocytes play an essential role in various neurodegenerative diseases (Maragakis & Rothstein 2006, Verkhratsky et al. 2010), of which AD is the most prominent one. The increasing number of diagnosed Alzheimer´s diseases among the more and more aging population in our society and the severity of degradation of the personalities of the affected persons, due to the destructive processes taking place in the affected brains, make the understanding of this degenerative disease one of the biggest challenge of brain research.

In 1910 Alois Alzheimer showed, that neuroglia play an essential role in the pathology of the disease later named after him, in that he found enlarged numbers of neuroglia surrounding abnormal extracellular protein deposits, which were named neuritic plaques (Alzheimer 1910). Later it became obvious that the development of reactive astrogliosis is a typical symptom of the late stages in an "Alzheimer´s brain" (Meda et al. 2001, Mrak & Griffin 2005). Thus cellular hypertrophy (Rodriguez et al. 2009), as well as overexpression of GFAP (Beach &

McGeer 1988) and S100ß (Griffin et al. 1989, Sheng et al. 1996) were found postmortem in brain tissue of patients, but also after AD induction in animal model systems (Nagele et al. 2003, 2004, Olabarria et al. 2010, Kashon et al. 2004, Verkhratsky et al. 2010). Furthermore there exists a correlation between the severity of astrogliosis and the cognitive impairment observed in patients (Kashon et al. 2004). Reactive astrocytes were found in connection with neuritic plaques, which have been shown to be extracellular deposited aggregates of the insoluble fibrillary amyloid beta protein (Aß). These plaques represent an AD hallmark (Simpson et al. 2008, Verkhratsky et al. 2010). Aß aggregates were identified, besides signals from damaged or dying cells, as triggers for reactive astrogliosis. Aß was found to induce $[Ca^{2+}]_i$ oscillations *in vitro* and *in vivo*, which play an important role in amyloid neurotoxicity, due to an impairment of astrocyte´s ability to support neurons (Abramov et al. 2003, 2004, Kuchibhotla et al. 2009, Verkhratsky et al. 2010).

Also other triggers for the development of astrogliosis, as cytokines, NO and reactive oxygen species (ROS), and the release of inflammatory and neurotoxic factors by reactive astrocytes participate in neuro-inflammatory processes in the AD pathology (Heneka et al. 2010, Verkhratsky et al. 2010). A study that used transgenic animals (3xTg-AD) expressing the three mutant gene variants: for the swedish familial Alzheimer’s disease amyloid precursor protein mutation (APP_{Swe}), presilin $1PS1_{M146V}$, and tau $_{P301L}$ found that astrocytes exhibited a morphological atrophy, i.e. a decrease in the staining pattern for GFAP and a reduction in the size of cell somata and the number of processes (Oddo et al. 2003, Verkhratsky et al 2010). This study also revealed, that the presence of senile Aß plaques leads to reactive astrogliosis in the direct proximity, whereas remote astrocytes exhibited the morphological atrophy (Rodriguez et al. 2009, Olabarria et al. 2010, Verkhratsky et al. 2010).

The presence of reactive astrocytes in the direct neighborhood to Aß plaques might be due to the fact, that astrocytes play a role in removing Aß protein (Rossner et al. 2005, Guenette 2003, Nicoll & Weller 2003, Verkratsky et al. 2010). The examination of transgenic animals expressing the amyloid precursor protein (APP) revealed that reactive astrocytes close to Aß plaques contained an enzyme called neprilsyn, which enables them to degrade Aß. Furthermore *in vitro* experiments also demonstrated the ability of astrocytes to phagocytize and degrade Aß aggregates (Apelt et al. 2003, Wyss-Coray 2003, Nagele et al. 2003). Since astrocyte reactivity has been demonstrated to be linked to Aß plaques, the question arose, what exactly is the role of Aß, besides the other putative players APP and tau, in Alzheimer´s pathology. Due to the high conformational heterogeneity of Aß, complicating a functional characterization of specific oligomers, it became of interest, to create a mouse, overexpressing an exclusive, homogeneous and neurotoxic dimer version of Aß. In 2011, Müller-Schiffman and colleagues managed to synthesize a stable functional dimeric transition state of Aß, called Aß-S8C. In a further step they established a mouse expressing this soluble and highly synaptotoxic Aß peptide version in high amounts, thereby demonstrating the role of dimeric Aß in the cognitive impairment associated with AD (Müller-Schiffmann et al. 2011). The question arose, what impact this genetic modification for the tentative development of reactive gliosis in this mouse model system had.

1.6 Aim of the study

The aims of this study were to develop reliable methods to measure changes in the volume and morphology of astrocytes in acute hippocampal brain slices over minutes up to hours and in hippocampal slice-cultures over days to weeks, as well as to detect chronic changes in the cytoskeleton of the cells.

The first question was, whether the labeling of single astrocytes with fluorescent dyes by using the patch-clamp technique, as described by Bushong et al. (2002), who successfully revealed astrocyte morphology in fixed brain slices of rats, could be adopted to label vital cells in acute hippocampal slices of mice, in order to investigate dynamic changes by confocal laser scanning fluorescence microscopy.

In a next step, it was tried to adopt the technique of real-time detection of volume changes in brain slices, a described by Risher et al. (2009), into the model system of SR101-stained acute hippocampal brain slices of mice. The question was, whether a system for the documentation of volume changes over a period of one to six hours could be developed in order to investigate the mechanisms of volume regulation in astrocytes, the NKCC1. Then, the effect of NH_4^+ on the volume regulation of astrocytes was investigated as an example for the development of NH_4^+-induced brain edema at early stages.

Hippocampal slice cultures of GFAP/GFP-expressing transgenic mice were used to induce reactive gliosis by setting a lesion in the CA1 region of the hippocampus and to investigate astrocyte morphology in the direct neighborhood and the periphery of the accrued glial scar. The question was, whether astrocyte reactivity is accompanied by a chronic change in cell volume over days to weeks in culture.

A final set of experiments addressed to the question, whether overexpression of the AD specific human APP751, including the familial Swedish (APP_{Swe}) and the Aß dimer mutation (Aß-S8C), under the control of the neuron-specific Thy1-promoter alters the number of S100ß-positive astrocytes and the content and expression of GFAP in the hippocampus of aged mice. To answer these questions, fixed tissue slices of transgenic and wild type mice were immune-histochemically labeled against GFAP and S100ß and compared to each other.

2 Materials and Methods

For the present work, several techniques for tissue-preparation, -culture and imaging of fluorescent labelled cells were used and the deployed animals, applied chemicals and solutions, as well as methodological approaches are explained in this chapter.

2.1 Ethics statement

All experimental procedures within were executed in consistence with the institutional guidelines of the Heinrich-Heine-University (HHU) Düsseldorf, the European Community Council Directive (86/609/EEC) and the approbation of the Animal Welfare Office at the Animal Care and Use Facility of the HHU (Institutional Act number: 052/05). Following the recommendation of the European Commission (Euthanasia of experimental animals, Luxembourg: Office for Official Publications of the European Communities, 1997; ISBN 92-827-9694-9), mice were quickly decapitated for the generation of acute tissue slices, tissue slice cultures and fixed tissue slices. Mice at the age or older than P 14, as used for acute or immunohistochemical experiments were anesthetized with CO_2 before decapitation. As the decapitation represents a postmortem removal of brain tissue no further formal approval was necessary.

2.2 Acute tissue slices and solutions

For the preparation of acute hippocampal brain slices, 14 to 16 days old (P14-16) Balb/c mice (*Mus musculus*) of both genders where used under application of standard preparation techniques (Meier et al. 2006, Kafitz et al. 2008). After explantation, brains were embedded in ice-cold artificial cerebrospinal fluid (ACSF) containing (in mM) 125 NaCl, 2.5 KCl, 2 $CaCl_2$, 1 $MgCl_2$, 1.25 NaH_2PO_4, 26 $NaHCO_3$ and 20 glucose, bubbled with 95% O_2 and 5% CO_2 (carbogen) and adjusted to pH 7.4. Brain hemispheres were separated, trimmed and sectioned transversally into slices with 250 µm thickness by using a vibratome (Microm HM650V, Thermo Fisher Scientific, Walldorf, Germany), including the entorhinal cortex, hippocampus proper and dentate gyrus. For whole-cell patch-clamp and live-cell confocal imaging experiments, slices where incubated for 20 min in ACSF (34°C) containing ~2 µM sulforhodamine 101 (SR101) for astrocyte specific vital staining and then transferred in SR101-free ACSF (34°C) for additional 10 min (Kafitz et al. 2008).

The experiments done at an upright fixed-stage confocal laser scanning microscope (Nikon E600 FN C1; Nikon Instruments, Düsseldorf, Germany). Slices were kept in a perfusion chamber and continuously perfused with carbogen-bubbled ACSF. The measured osmolarity of ACSF was ~316 mOsm.

To induce cell swelling hypoosmolar ACSF with an measured osmolarity of ~222 mOsm containing (mM) 83.3 NaCl, 1.7 KCl, 1.3 $CaCl_2$, 0.7 $MgCl_2$, 0.8 NaH_2PO_4, 17.3 $NaHCO_3$ and 20 glucose was used.

To induce cell shrinkage a hyperosmolar ACSF with ~450 mOsm (measured) was used containing (mM) 227 NaCl, 4.5 KCl, 3.6 $CaCl_2$, 1.8 $MgCl_2$, 2.3 NaH_2PO_4, 47.3 $NaHCO_3$ and 20 glucose.

NH_4^+ experiments were performed with an ACSF in which 5 mM NaCl was substituted by NH_4Cl, as this represents standard NH_4^+ concentration for experiments to study HE. Similar NH_4^+ concentrations were found in animals with acute liver failure (Swain et al. 1992). To compensate for the slightly elevated Cl^--concentration in NH_4^+-ACSF, due to the addition of NH_4Cl, the regular ACSF for these experiments contained a NaCl concentration of 130 mM. To investigate the function of the NKCC1, 100 µM Bumetanide (Biotrend AG, Wangen/Zurich, Switzerland) was added to the respective experimental solutions (Kelly & Rose 2010).

2.3 Cultured tissue slices

For the preparation of organotypic hippocampal slice cultures (OHSC) transgenic mice were used (FVB/T-Tg[GFAPGFP]14Mes/J; obtained from Jackson Laboratory; Harbor, USA), which expressed green fluorescent protein (GFP) under the GFAP promoter.

After explantation, brains were embedded in ice-cold ACSF containing (in mM) 125 NaCl, 2.5 KCl, 2 $CaCl_2$, 1 $MgCl_2$, 1.25 NaH_2PO_4, 26 $NaHCO_3$ and 20 glucose, bubbled with 95% O_2 and 5% CO_2 (Carbogen) and adjusted to pH 7.4. Hemispheres were separated, trimmed and sectioned transversally with 200 µm thickness, including the entorhinal cortex, hippocampus proper and dentate gyrus, by using a vibratome (Microm HM650V, Thermo Fisher Scientific, Walldorf, Germany). OHSCs were produced and cultured as described by Stoppini et al. (1991) using a slightly modified protocol (Schreiner et al 2013). The tissue slices were placed on a Millicell interface culture insert (PICM ORG 50, hydrophilized PTFE, pore size 0.4 µm; Merck

Millipore, Darmstadt, Germany) and incubated with a serum-based, antibiotic-free culture medium in a humidified incubator (5% CO_2, 37°C). The culture medium was made of 40% Hank´s balanced salt solution (HBSS; GIBCO/Life Technologies, Darmstadt, Germany), 30% Dulbecco´s modified eagle medium (DMEM; Gibco/Life Technologies) and 30% sterile-filtered normal horse serum (NHS; Gibco/Life Technologies) supplemented with 38 mM glucose (pH adjusted to 7.3-7.4). Slices were inspected and medium was changed three times a week, the surfaces of the inserts were washed with medium once a week (Schreiner et al 2013). Slices were kept in culture for 12 days (days *in vitro* (DIV) 12) for acclimatization and tissue flattening. After that time, a mechanical lesion was set by using a sterile scalpel blade. This was done by cutting through the *stratum pyramidale* (pyramidal cell layer) in the CA1 region, including the overlying *stratum oriens*, the subjacent *stratum radiatum* and *stratum lacunosum moleculare*. Afterwards, the slices remained in culture for additional 6-7 days (DIV 17-19). Untreated control slices were prepared and cultured simultaneously for a similar time period (Schreiner et al 2013).

A propidium iodide (PI) assay was applied to detect cell death. Therefore slice cultures were incubated, with PI (0.5 µg/ ml) in ACSF on the surface of the inserts, for 3 hours at 37°C and 5% CO_2 and washed with ACSF afterwards. For immunohistochemistry, slice cultures were fixed in 4% paraformaldehyde (PFA) in phosphate-buffered saline (PBS, 0.01 M, pH 7.4) for 30 min at room temperature (RT) and then washed three times with PBS every 30 min.

For documentation, confocal laser scanning microscopes were used (Nikon E600 FN C1; Nikon Instruments, Düsseldorf, Germany and Olympus Fluoview300; Olympus, Hamburg, Germany; Schreiner et al 2013).

2.4 Fixed tissue slices

For the preparation of fixed tissue slices, a transgenic mouse line was used (C57BL/6N background). These mice expressed the human APP751, including the familial Swedish and the Aß dimer mutation (Aß-S8C), under the control of the neuron specific Thy1-promoter (APP751swe-Aß-S8C) and were termed "tgDimer" (Müller-Schiffmann et al. 2014). After dissection of the brain, tissue was kept in 4% PFA at 4°C for 48 hours, then washed three times with PBS every 30 min at RT and stored in PBS at 4°C until slices of 30 µm thickness were made. To achieve that, brains were enclosed with 4% agar to stabilize. Sectioning was done in cooled PBS (0.01 M, pH 7.4, 4°C) and slices were stored in PBS at 4°C until immune-histochemical staining.

2.5 Whole-cell patch-clamp

For the staining of single astrocytes dye was injected by using the whole-cell patch-clamp technique (Stephan et al. 2011). Acute tissue slices were placed in a perfusion-chamber at an upright fixed-stage microscope (Nikon E600 FN C1, 60x water immersion objective, N.A. 1.00; Nikon Instruments). An ECP 800 USB patch-clamp amplifier, remote-controlled by "PatchMaster"-software in combination with an LIH 1600 acquisition interface (HEKA Elektronik; Lambrecht, Germany) was used. Patch pipettes were produced from borosilicate glass capillaries (Hilgenberg; Waldkappel, Germany) by pulling them out to a resistance of 2 to 3 MΩ in a vertical pipette puller (PP-830, Narishige; Japan). Pipettes were filled with a solution containing (in mM) 120 K-$MeSO_3$, 24 KCl, 12 NaCl, 4Mg-ATP, 0.4 Na_3-GTP and 10 HEPES (N-(2-Hydroxyehtyl)piperazine-N´-2ethanesulfonic acid), adjusted to pH 7.30 (Stephan et al. 2011).

For immunohistochemistry 100 µM AlexaFluor594-hydrazide and 5 µl Neurobiotin (20%) was added to the pipette solution, and for time-lapse live-cell imaging experiments 200 µM AlexaFluor488-hydrazine. To stain single astrocytes, cells were clamped to a membrane potential (E_m) of -85 mV. The liquid potential correction was performed, but neither the compensation of the series resistance, nor of the slow capacitance was done due to the insufficient voltage control of mature astrocytes (Zhou et al. 2009, Stephan et al. 2011). Astrocytes were held for at least 20 min attached to the patch pipette in whole-cell mode for filling with dye; then the pipette was withdrawn as cautious as possible under visual control to keep cell soma as intact as possible. Then, the slices either were taken for life-cell imaging experiments, or were immersion-fixed with 4% PFA for 30 min at RT for immunohistochemistry, followed by three washes with PBS every 30 min.

2.6 Immunohistochemistry

For immunohistochemistry different treatments were implemented. Patch-filled, immersion-fixed slices were treated with PBS containing 0.25% triton-X100 (TX) for 90 min at 4°C to permeabilize cell membranes, followed by three washes for 10 min each with PBS at the same temperature. Afterwards, the slices were incubated in 100 µl Avidin Alexa 488 (50 µl/ml) in PBS for 3 h at RT. Subsequently, the slices were again washed in PBS three times for 10 min each, and then stored in PBS at 4°C or processed for documentation by placing them on microscope slides followed by embedding in mowiol/DABCO (Calbiochem, Fluka, distributed by Sigma-Aldrich Chemical, Munich, Germany).

For organotypic slice culture staining, fixed slices were transferred to PBS containing 0.25% TX and 2% normal goat serum (NGS; GIBCO/Life Technologies) for 90 min at 4°C to permeabilize cell membranes and to block unspecific binding sites. The further immunohistochemical processing of slice cultures used for the experiments presented in Schreiner et al. (2013) is described here (2.5 Immunohistochemistry; attachment). For the documentation of GFAP/GFP fluorescence, slices where subjected to DAPI staining (4´,6-diamino-2-phenylindole; 0.5 µM; Invitrogen) for 10 to 15 min, washed three times in PBS at RT, placed on microscope slides, and were embedded in mowiol/DABCO (Calbiochem, Fluka, distributed by Sigma-Aldrich Chemical).

For immunohistochemical staining of fixed tissue slices of “tgDimer”-mice, specimen were transferred to PBS containing 0.25% TX and 2% NGS for 90 min at 4°C. For GFAP/S100ß double staining, slices were incubated in a solution containing both primary antibodies, GFAP-mAb (1:1000, DAKO Cytomation, Glostrup, Denmark) and rabbit-S100ß (1:100, Abcam, United Kingdom) in PBS containing 0.25% TX and 2% NGS over night at 4°C. In the next step, slices were washed fife times in 2% NGS/PBS and then incubated with anti-mouse-AlexaFluor488 and anti-rabbit-AlexaFluor594 (1:100) in blocking solution for 2h at RT. After an additional DAPI staining and a three times wash, slices were placed on microscope slides and embedded in mowiol/DABCO prior to documentation.

To ensure reproducibility, tissue processing and immunohistochemical staining protocols were identical for the respective experiments. Parallel to each staining procedure, negative controls lacking either one or both primary antibodies were performed to proof specific antibody labeling. Unless stated otherwise, all chemicals were purchased from Sigma-Aldrich Chemical (Munich, Germany).

2.7 Image analysis

Confocal microscopy was used to monitor the fluorescent GFP-expressing and immunohistochemically labelled cells stained with SR101 by using the whole-cell patch-clamp technique. For this purpose an upright fixed-stage microscope, based on a Nikon E600 FN (Nikon), combining transmission (differential interference contrast), epifluorescence and confocal laser scanning microscopy, coupled to a D-eclipse C1 scan head (Nikon), was used. The microscope was equipped with an Intensilight fiber lamp (C-HGF1, Nikon Instruments), as well as a helium-neon (543 nm), an argon (488 nm, both Melles Grillot, Bensheim, Germany) and a diode laser (407 nm, Coherent LaserSystems, Göttingen, Germany). Images were taken with either a 10x/0.5 water immersion (Flour), a 20x/0.75 (Plan Apo VC), a 60x/1.00 water immersion (Flour), or a 60x/1.40 oil immersion objective (Plan ApoVC, all from Nikon). EZ-C1 3.91 Software (Nikon) was used for image acquisition.

To improve image quality, an average image calculation operation of 2 was used for life cell imaging, and an average of 4 for the documentation of immunofluorescence. The thickness of z-plane sections was 0.35 µm; the number of optical sections of the acquired stacks varied depending on the experimental conditions. Unless stated otherwise, images of z-stack scans were compressed into maximum intensity projections (MIP), displaying the pixel with the maximal intensity of every image in the respective stack in a single, two-dimensional image.

For the analysis of GFAP fluorescence in immunohistochemically stained specimen of tgDimere-mice, a quantitative approach was applied, in which grey values above background threshold were counted to calculate the percentage of GFAP-positive signals related to GFAP-negative signals below the threshold value. The values for the background threshold were obtained by measuring the gray values of line plots that were placed in an area, where no or just a minor signal of GFAP fluorescence was expected. With respect to the hippocampus formation, this is the case for the *cornu ammonis*, where somata of pyramidal neurons are located, as well as the *dentate gyrus*, the location of the granule cell bodies. The gray values of these “dark areas” were measured, and used as background threshold. In a next step, the gray value of every pixel in an image was calculated, the number of pixels above the threshold value was normalized to the total pixel number and presented as percentage of GFAP-positive pixels per image (internal correspondence with Dr. Karl W. Kafitz).

For the analysis of scratch wound experiments an Olympus BX51WI microscope coupled to a confocal laser scanning system (FV300) and equipped with a multiline argon (488 nm) and a helium-neon laser (543 nm, both Melles Grillot) came into operation. Images were taken with either a 20x/0.5 (UMPlanFl, Olympus), a 40x/0.8 water immersion (LUMPlan, Olympus) or a 60x/1.40 oil immersion objective (Plan ApoVC, Nikon). A Kalman filter 4, i.e. an average image calculation operation of 4, was used. The thickness of z-plane sections was 1 µm, the number of sections varied depending on the preparation. For the calculation of astrocyte soma size, confocally monitored GFP-fluorescence in hippocampi of GFAP/GFP-expressing mice was analyzed in a semi-quantitative approach in that fluorescence-labelled somata of every single cell in each stack were marked by hand and the resulting areas were automatically calculated (Schreiner et al. 2013).

For image processing and analysis, either NIS-Elements (Nikon), or ImageJ software (NIH, Bethesda, USA) was used. Adobe Photoshop CS2 (Adobe Systems GmbH, München, Germany) was applied for further image presentation, data illustrations were done by using Adobe Illustrator CS2.

2.8 Statistics

Unless otherwise specified, data were calculated with Excel and presented as means ± S.E.M.. For statistical analysis one-tailed Student´s *t*-test was used, in which a p value < 0.05 represents statistical significance (* $p < 0.05$, ** $p < 0.01$, *** $p < 0.001$). n displays the number of analyzed cells and N the number of slices.

3 Results

3.1 Astrocyte labeling via whole-cell patch-clamp

The whole-cell patch-clamp technique was used to label astrocytes in the *stratum radiatum* of the CA1 region of acute hippocampal slices for confocal recording of volume regulation processes over time. Additionally, astrocytes can successfully be fixed and processed below for immunohistochemical purposes. Fig. 3.1 A shows astrocytes labelled with the fluorescent dye AlexaFluor594 (AF 594). The upper picture on the left shows an immature astrocyte; clearly visible are the soma and two opposing major, as well as several fine processes. The lower major process contacts a blood-vessel with its end-feet and participates in the formation of the blood-brain barrier (BBB). The lower picture on the left in Fig. 3.1 A shows a mature, star shaped astrocyte of about 35 µm in diameter. Several major processes originate from the cell soma and branch into various finer ones, thus forming the spongiform arrangement typical for a participant of the astrocyte network in the hippocampus.

In addition to the fluorescent dye, the patch pipette contained neurobiotin, which can pass through the gap junctions between the overlapping processes of neighboring astrocytes and in that way tags surrounding astrocytes, which are coupled to the primary labeled cell. After the fixation of the slice, the fluorescent dye AlexaFluor488-conjugated avidin forms a complex with the injected neurobiotin in an immunohistochemical step, making the gap junction coupled astrocyte network detectable for confocal laser scanning microscopy (Fig. 3.1 A, NB-AF488). Furthermore, a strongly ramified blood vessel system becomes visible. The application of DAPI during immunohistochemical processing allows for the visualization of the nuclei of the various cells located in the *stratum radiatum* (Fig. 3.1 A, DAPI). Recognizable are the nuclei of the primary and secondary labeled astrocytes as well as the nuclei of endothelial cells, which form the capillaries of the blood vessel system. Additionally, several nuclei of unlabeled cells can be seen. Merged together, the different labelling techniques give an impression of single astrocytes and of the astrocyte network formed by gap junction coupling, which is embedded in the tissue of the hippocampus formation (Fig. 3.1 A, Merge).

The following experimental step was to label a single astrocyte with AlexaFluor488 by use of the whole-cell patch-clamp technique to stain one single astrocyte entirely and to perform long-term imaging in 10 min intervals in regular ACSF after successful “de-patching” (Fig 3.1 B). While patching cells for immunohistochemistry proved to be a practical method to label astro-

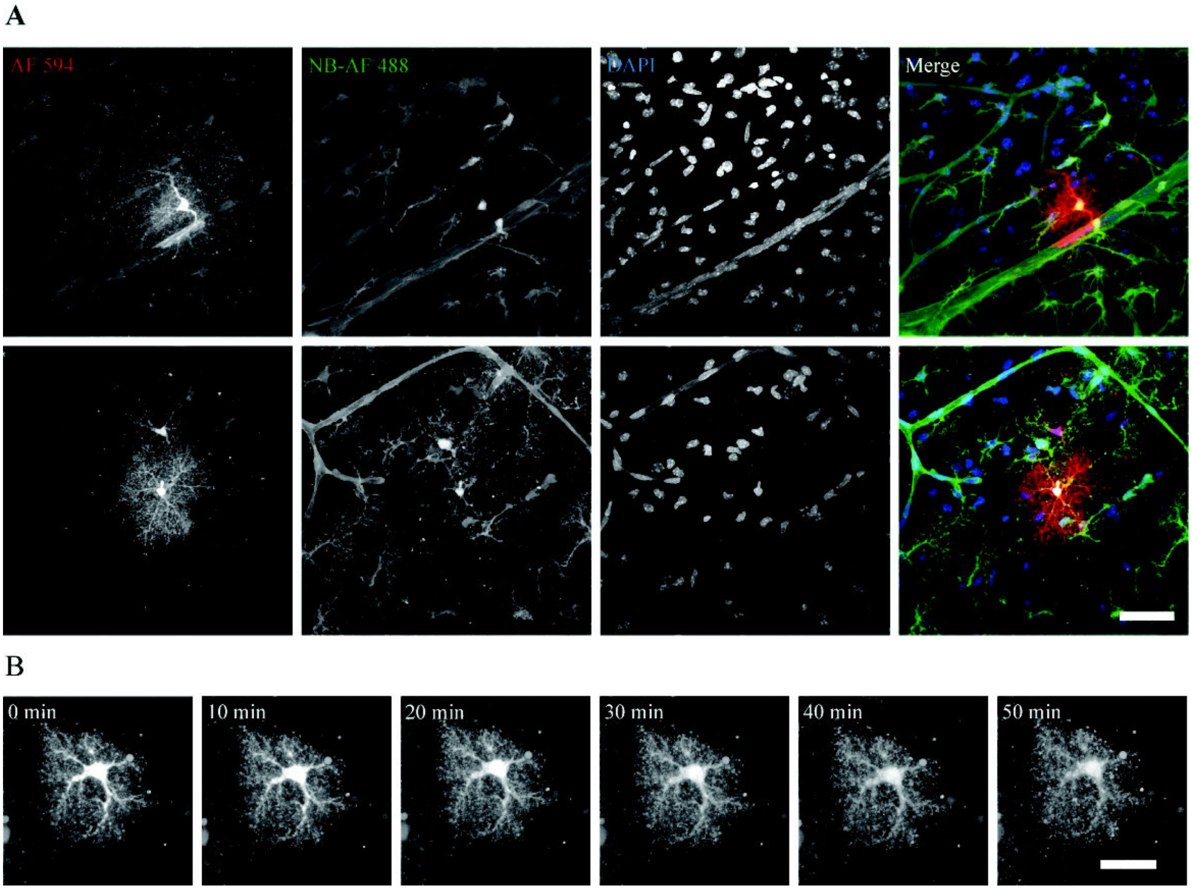

Figure 3.1: **Fluorescent labeling of astrocytes via whole-cell patch-clamp in acute hippocampal sclices** Confocal z-stack maximum intensity projections (MIP) of hippocampal CA1 astrocytes in the *stratum radiatum* of the CA1 region **A**) Single cells, an immature astrocyte in the upper and a mature astrocyte in the row below, where labeled with the fluorescent dye AF594 (AF 594, left), in combination with gap junction-permeable neurobiotin. Complexed with AF488-conjugated avidin (NB-AF488, middle left) and co-stained with DAPI (DAPI, middle right) the merge images (Merge, right) show how single astrocytes form a network and participate in the formation of the blood-brain barrier. **B)** Single astrocyte, labelled with AF488. Images were acquired at 10 min intervals, starting at time point t_0 (0 min), the first scan after 20 min attached to the patch-pipette for fluorescent labelling and subsequent de-patching. Showing a well stained, healthy cell shape in the beginning, the cell disrupts and starts to disintegrate between time point t_4 and t_5 (30 - 40 min); Scale bars: (A) 20 µm, (B) 10 µm. [own image, Institute of Neurobiology, Düsseldorf].

cytes, long-term imaging turned out to be more problematic, because the survival rate of the cells for the next 50 min after removing of the patch pipette was drastically diminished. As shown in figure 3.1 B, astrocytes, after appearing well stained and intact at the beginning of the imaging sequence (0 min to 20 min), tended to disrupt over time, so that the targeted six scans of an labelled and vital astrocyte in this experimental setup could not be accomplished. This problem occurred in approximately all of the 33 experiments carried out and Fig. 3.1 B shows the most successful result for this experimental approach.

3.2 Detection of volume changes in astrocytes

3.2.1 SR101 labeling and image acquisition

The staining of acute hippocampal tissue slices with SR 101 has been proven to be a practicable and reliable tool for the specific labeling of vital astrocytes (Kafitz et al. 2008). Here, it was used for the development of a method for the measurement of volume changes in astrocytes. SR101 can be applied during the preparation process, it provides a bright and stable astrocyte-specific staining pattern and because other cell types remain unstained, the specificity of the staining can easily be verified by observing the slice with transmission and epifluorescence microscopy (Fig. 3.2 A, C). Thus SR101-stained slices were positioned into the perfusion chamber of the upright fixed-stage microscope and continuously perfused with ACSF. To ensure the vitality of the slice, its appearance had to be examined. Therefore, the pyramidal cells in the CA1 region were observed at higher magnification (inset Fig. 3.2 A).

SR101 fluorescence has an excitation maximum at the wavelength of 578 nm and an emission maximum at 594 nm. A confocal setup with a 543 nm He-Ne laser for excitation and a 603 nm emission filter with a bandwidth of 75 nm were used for documentation (Fig. 3.2 B).

In case of successful staining, a clear pattern was observed with astrocytes showing bright fluorescence in all layers of the hippocampus formation, i.e. in the *stratum oriens, radiatum, lacunosum, lacunosum-moleculare* of the hippocampus and in the molecular layer of the dentate gyrus. A lack of stained neurons in the CA regions and in the dentate gyrus connote the specificity of the SR 101 staining.

Then an area within the *stratum radiatum*, deeper than at least one cell layer (~50 µm) below the surface of the slice was chosen, where a sufficient number of bright stained astrocytes with a vital appearance were found (inset Fig. 3.2 C). Prior to the first scan, several adjustments had to be carried out, in order to obtain images suitable for later threshold operations: first, gain and offset parameters of the photomultiplier (PMT) had to be adjusted such that within the centers of astroglial somata a saturated fluorescence signal was measured, without outshining their boundary areas, for the correct determination of the cell shape. Next, the depth of the scan along the z-axis had to be determined, so that the scanned volume contained about two to three cell layers. After these adjustments had been made, z-scans were taken at respective time points throughout an experiment, in which t_0 (0 min) represented the first scan at the beginning of each experiment. Since all experiments at t_0 were carried out in regular ACSF, this initial scan serves

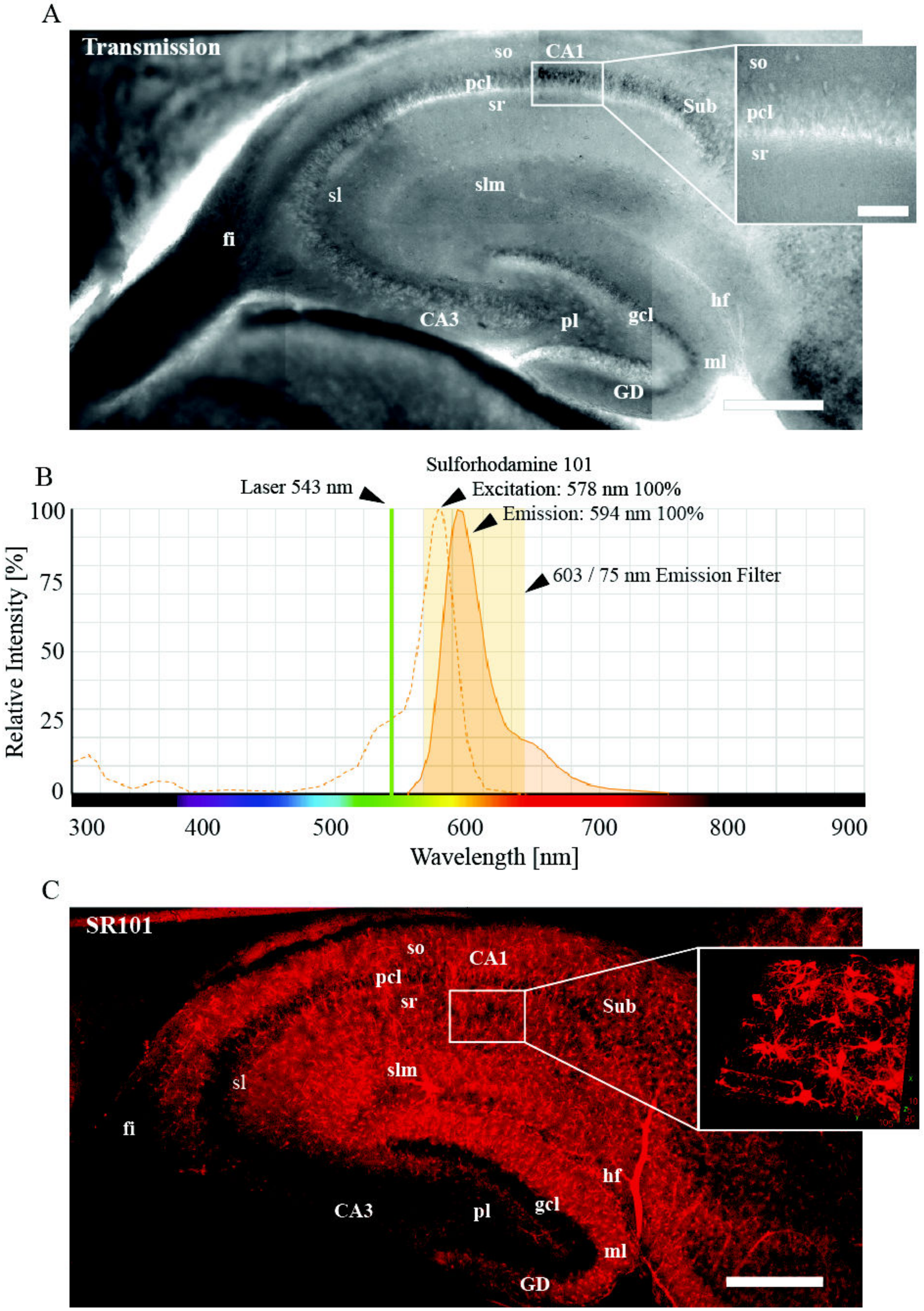

Figure 3.2: for explanation see next page.

Figure 3.2: **SR 101 staining of astrocytes in acute hippocampal slices. A)** Transmitted light image (composition) of an acute hippocampal tissue slice showing the anatomy of the *hippocampus proper*: CA1, 3 (*cornu ammonis*), fi (*fimbria*), gcl (granule cell layer), GD (*gyrus dentatus*), hf (hippocampal fissure), ml (molecular layer), pcl (pyramidal cell layer), pl (plexus), sl (*stratum lacunosum*), slm (*stratum lacunosum-moleculare*), sr (*stratum radiatum*), so (*stratum oriens*), Sub (*subiculum*); the inset shows the somata of pyramidal cells in CA1 in higher magnification. **B)** Spectral properties of SR 101 (excitation/emission maxima ~ 586/605 nm) and used setup devices for documentation (He-Ne Laser, wavelength 543 nm for excitation and 603 nm emission filter, bandwidth 75 nm) **C)** Confocal fluorescence image (composition) of a SR101 stained acute hippocampal slice. Clearly visible are the hippocampal anatomy and the pattern of stained astrocytes within the slice. The inset shows a 3D-like reconstruction of a life cell imaging z-stack, as it was used for the documentation of volume changes. Scale bars: 250 µm (A, C), 30 µm (A inset). A) and C) own images, Institute of Neurobiology, Düsseldorf, B) obtained and modified from http://www.lifetechnologies.com/de/de/home/life-science/cell-analysis/labeling-chemistry/fluorescence-spectraviewer.html.

as a baseline for all executed experimental procedures. The scan intervals varied from 10 to 30 min, according to experimental requirements. Due to the fact that life cell imaging was performed, it was sometimes necessary to adjust the starting position of the scans and to perform corrections of gain and offset, especially if the ACSF osmolarity was changed.

While SR101 staining of astrocytes in acute hippocampal slices of mice represents a well-established technique (Kafitz et al. 2008), the development of a semi-automated method for the measurement of volume changes in astrocytes required the formulation of a protocol for handling parameters and the elaboration of the image-processing and -analysis procedures presented in the following chapters.

3.2.2 Image processing and analysis

The z-stacks, obtained from confocal laser scanning of SR101-labelled astrocytes, were compressed into single, two-dimensional maximum intensity projections (MIP) for further analysis, i.e. the calculation of the soma area (Fig. 3.3 A). This approach assumes that volume changes of astrocyte somata occur uniformly in all directions, based on viewing along the z-axis. So, the measurements of changes in x- and y-dimensions were appropriate for the detection of relative volume changes, but underestimating actual volume alterations with the assumption, that they are nearly isotropic (Risher et al. 2009).

The detection of volume changes requires long term life cell imaging experiments with multiple z-scan procedures over time in intervals of several minutes. So, although SR101 is a very light-stable chromophore, bleaching is inevitable, and a reduction of fluorescence intensity might lead to false measurement results, because cell borders could not be detected properly. To ensure correct results, as far as automation of the threshold operation and area calculation is concerned, the MIPs obtained from z-stack imaging at different time points needed to be transferred into an 8 bit depth gray scale image first in order to process the images with ImageJ. Then, a bleaching

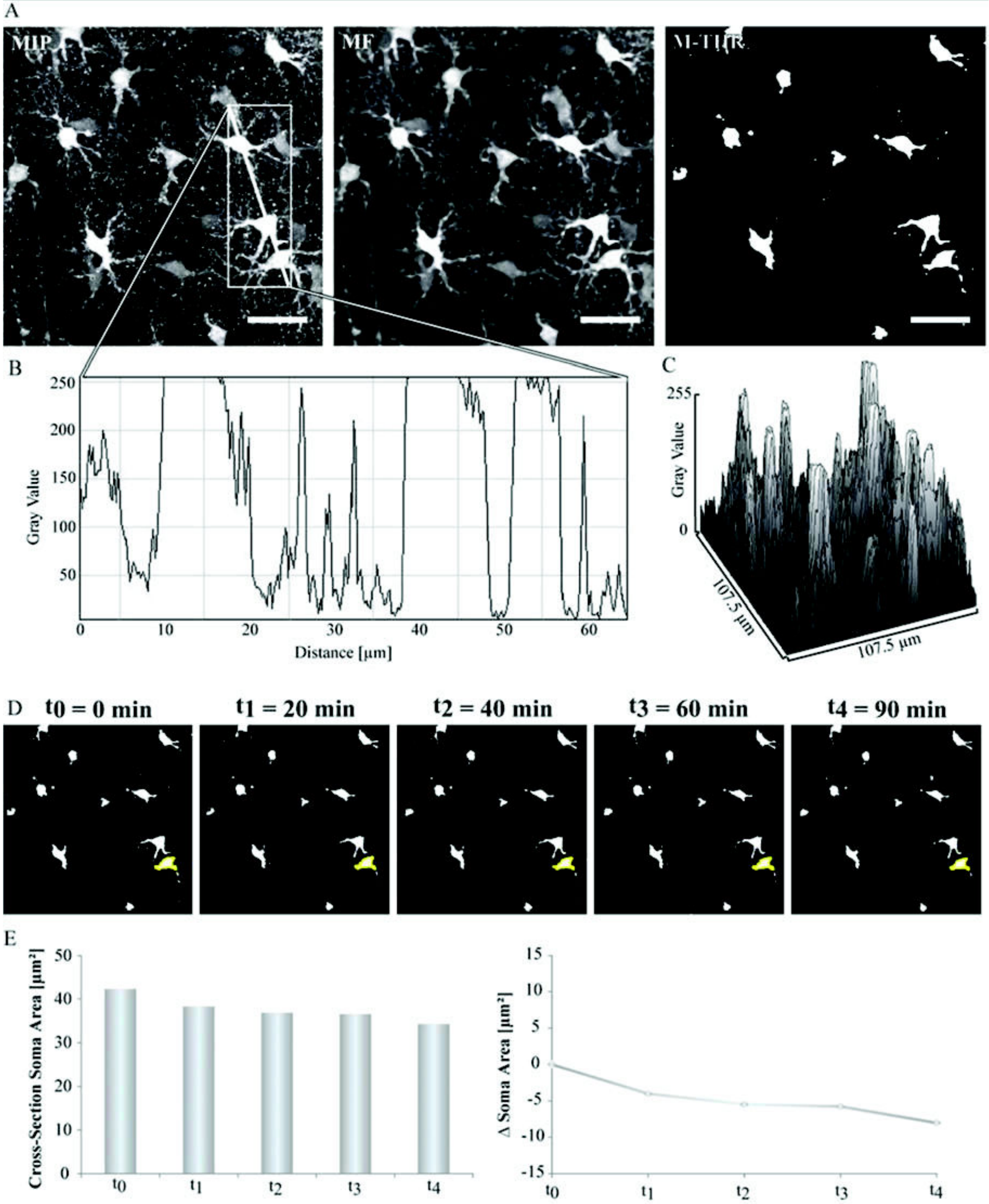

Figure 3.3: **Workflow for image processing and analysis for semi-automated measurements of astroglial soma area. A)** The first step of image processing is the creation of a maximum intensity projection (MIP), an operation that compresses all images of a z-stack into one two-dimensional image (see Material and Methods). Additionally, the pixel/µm ratio has to be set, that defines, how many µm equal one pixel. In a second step, a median filter (MF**)** and background subtraction prepares the image for the MINIMUM-Threshold algorithm, which converts the image into a binary image, showing all pixels below threshold as black and those above threshold as white. If image properties had been adjusted adequately, the auto-threshold operation provides a correct delineation of soma boundaries (M-Thr). **B)** To ensure that bleaching does not distort the results, the gray value intensity along a defined line plot of every image of a time lapse sequence was measured and adapted to the first image of the sequence by performing a color correction. **C)** Surface plots display the gray value distribution over the whole image. **D)** The ImageJ wand tracing tool (yellow) correctly outlines the cell of interest in every image of the time lapse sequence (t_0-t_4). **E)** The obtained data of the cross-section soma area in µm² can be displayed as absolute values or as differences (Δ) to values at t_0. Scale bars in A: 20 µm. [own image, Institute of Neurobiology, Düsseldorf]

correction with respect to the first scan of each experiment was performed by recording a line plot across two to three prominent cells in the t_0 (baseline) image, which provided the necessary information about the distribution of gray values along that particular line (Fig. 3.3 B). These values were compared to the line plot values in the images of the following time points and, if necessary, adjusted to those of t_0 by performing a color correction. Note that the gray values reached the saturation maximum at 255 of the 8 bit gray scale, when crossing the cell somata. The surface plot in Fig. 3.3 C represents an additional tool for the analysis of gray value distribution in the respective image.

For the display of spatial dimensions, it was necessary to define the picture properties. For spatial calibration, the EZ-C1 imaging software provides information about the pixel/µm ratio, which is determined by the objective used and by digital zoom. In case of a 60x objective and a twofold digital magnification the software displays 0.21 µm per pixel. That equals an edge length of 107.5 µm for an image of 512 x 512 pixels, as was used for this study (Fig. 3.3 C). This information enabled the software to calculate the area of the cell somata, as described later.

In order to perform an ImageJ threshold operation within the images, a 2.0 pixel median filter, a nonlinear digital filtering technique to remove noise and to smooth the image and a background subtraction with the "rolling ball" algorithm and a rolling ball radius of 50 pixels were applied (Fig. 3.3 A MF).

These individual operations ensured that the MINIMUM-Threshold algorithm correctly outlined the somata of appropriate astrocytes by converting the image into a binary image (M-THR). The previous adjustments at the steps of image acquisition and processing secured a consistent threshold value within one image sequence and in comparison to all other experiments (data not shown).

The "wand tracing tool" was used to mark the cell boundaries, so that the analyze function was able to calculate the areas of a particular cell within a time lapse image sequence (Fig. 3.3 D t_0-t_4). These values could be displayed as absolute values in µm² of an individual astrocyte over time, or the change (Δ) of soma areas with respect to the area at t_0 (Fig. 3.3 E).The results were occasionally compared to measurements of manually outlined cell somata, what ensured the correct function of measurement procedure (data not shown).

An additional tool to detect changes in the area of a cell soma is to transfer the MIPs of different time points into differing color channels of an RGB-image (red-green-blue), whereby in this study the red channel was always used for the image at t_0 and the green channel for images of later time points (Fig. 3.4 A and B). This results in yellow coloring of colocalized areas. If the observed astrocyte did swell, the additional soma area appeared green and if the astrocyte did shrink, the lost area appeared red (Fig. 3.4 C arrowheads).The here represented successful development of a protocol for the detection of acute volume changes in astrocytes, as it was part of this study, provided the prerequisite for the experiments described in the following.

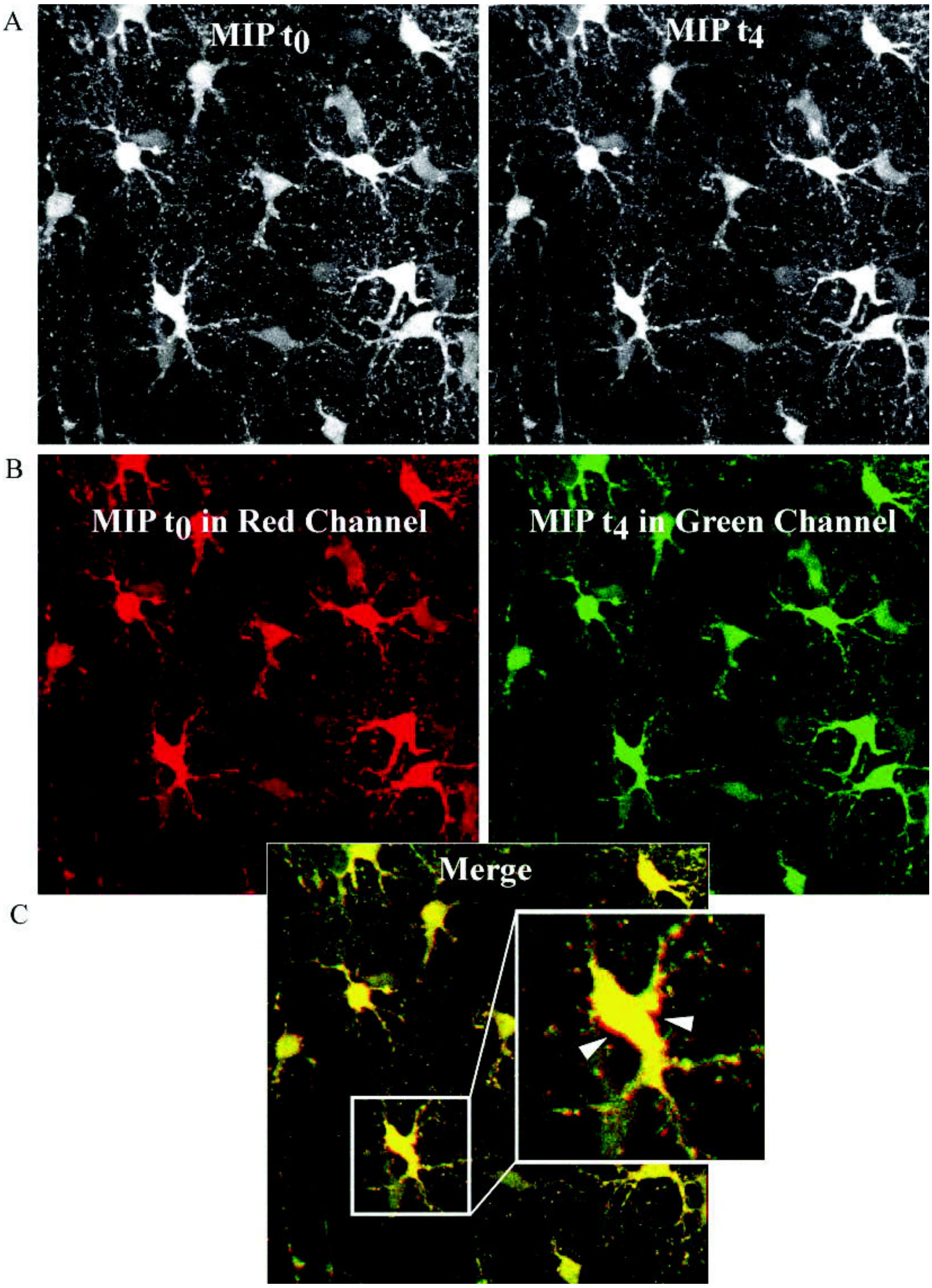

Figure 3.4: **Overlay image - a visual tool for the detection of volume changes.** The direct visual comparison of cells is another tool for the documentation of changes in astrocyte soma size over time. **A)** Confocal stacks taken at different time points were processed into MIPs **B)** MIP taken at t_0 was inserted into the red channel of a RGB-channel image and MIP taken at t_4 into the green channel. **C)** The image showing both color channels at the same time reveals differences in shape and size of the cells. Areas of conformity appear in yellow due to an additive mixture of red and green. In case of cell swelling at t_4 the increased soma parts are recognizable as green areas, in case of cell shrinkage, the reduced soma parts are recognizable as red areas (arrowheads). [own image, Institute of Neurobiology, Düsseldorf].

3.3 Volume changes in astrocytes

3.3.1 Volume changes in short-term control experiments

The documentation of volume regulation of astrocytes under control conditions marks a next step in the development of methods for the detection of changes in cell size. Acute hippocampal SR101-stained slices were imaged for about one hour in intervals of 10 min. Three different experimental procedures were applied: 1) control experiments in isotonic ACSF (Fig. 3.5 A), 2) application of hypoosmolar ACSF to induce cell swelling (Fig. 3.5 B) and 3) application of hyperosmolar ACSF to induce cell shrinkage (Fig. 3.5 C).

Imaging of astrocytes in isotonic ACSF revealed a soma area of 34.4 ± 1.6 µm² at t_0 (n = 50, N = 8; Fig. 3.6 C). Although the soma area values showed minor variations during the following 60 min, no significant alterations in cross-section soma area were measurable. The visual observation by regarding the overlay images ($t_0 + t_1$ to $t_0 + t_6$) confirmed this finding (Fig. 3.5 A).

The application of hypoosmolar ACSF after taking the image t_0 resulted in a significant increase in soma area from 39.1 ± 2.7 µm² at to 46.8 ± 3.2 µm² after 10 min (n = 48, N = 7). This enlargement persisted in the presence of hypoosmolar ACSF, except for a down regulation of the soma size after 20 min to a value not significantly different from the t_0 value. The return to normal osmotic conditions, i.e. isotonic ACSF, resulted in a significant decrease of the soma area down to 35.3 ± 2.4 µm² at t_5, lightly but not significantly smaller than the area at t_0 (Fig. 3.5 B). Again, these findings were confirmed by overlay images (Fig. 3.5 B, Overlay). Swollen areas were clearly visible during osmotic perturbation, but disappeared afterwards.

The application of hyperosmolar ACSF after taking the image t_0 resulted a significant decrease in cross-section soma area from 36.6 ± 2.3 µm² to 27.4 ± 2.2 µm² after 10 min (n = 32, N = 4). The soma size remained significantly lowered, even after the ACSF had been turned back to isotonic osmolarity. No back regulation to baseline area values at t_0 could be observed (t_5: 28.2 ± 1.8 µm², t_6: 27.6 ± 1.9 µm²). Here again, the overlay images could confirm this finding.

The comparative presentation of the data obtained in these experiments showing the changes of soma area in relation to the value at t_0 (Δ) revealed that astrocyte cell volume remained stable over one hour under control conditions. Hypoosmolar ACSF increased the soma area significantly by maximally +25 % and hyperosmolar ACSF decreased the soma area by -25 %. The return of osmolarity to regular conditions at t_5 caused a decrease of max. -9 % in the swelling experiment compared to t_0, whereas cell volume remained significantly decreased in shrinking

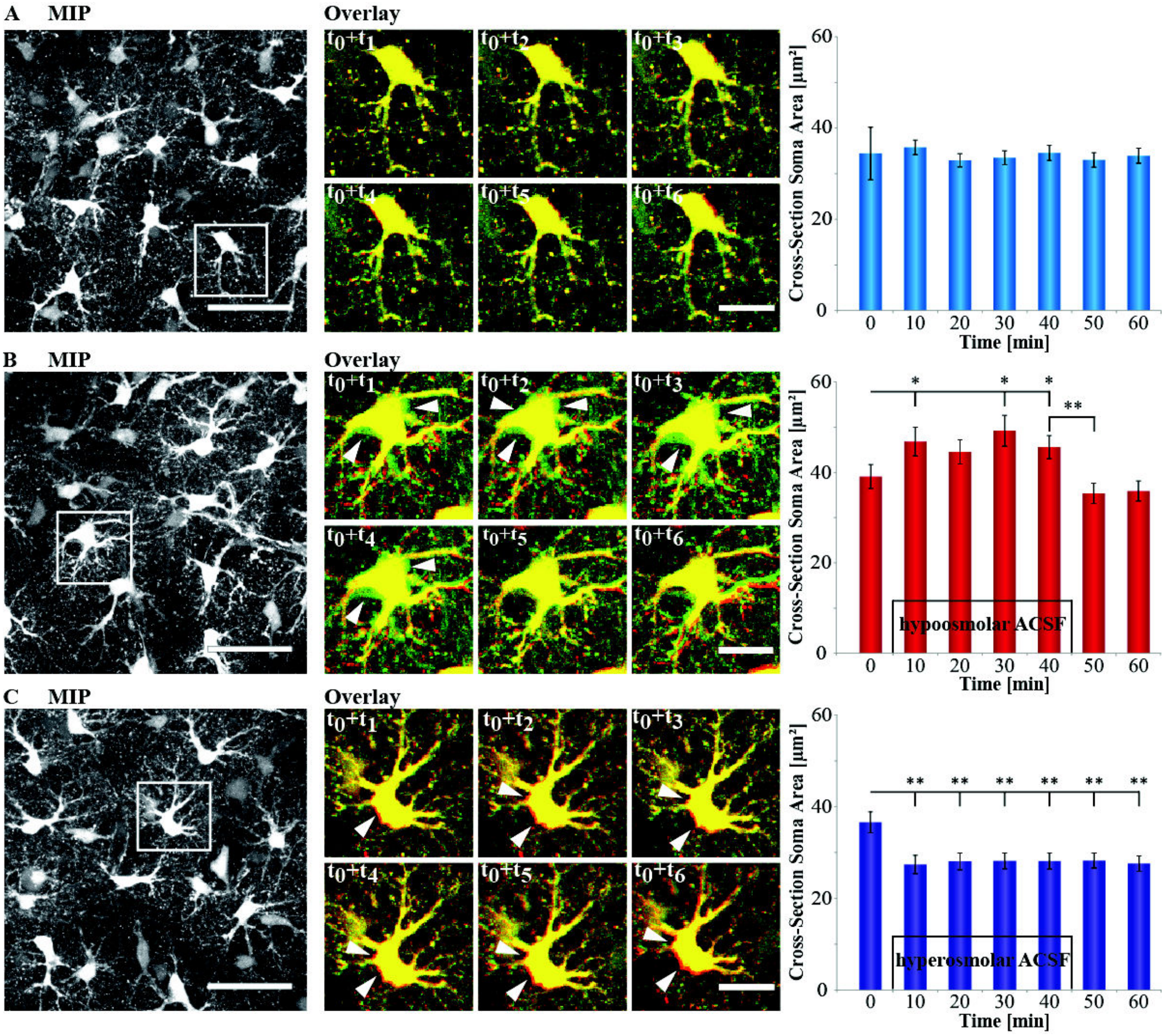

Figure 3.5: **Changes of astrocyte soma size in short-term control experiments.** Cells swell or shrink in response to changes in the osmolarity of the applied ACSFs. Experiments were done over 1h, scans were taken every 10 min. **A)** Soma area in isotonic ACSF (130 mM NaCl, ~316 mOsm); left: MIP image of SR101-stained astrocytes in hippocampal *stratum radiatum*. The marked cell was taken for overlay illustration (middle) of different time points, the red channel shows the astrocyte at t_0, the green channel at t_2-t_6. Yellow indicates an overlay, green areas cell swelling and red areas cell shrinking; right: summary of soma area measurements of 50 cells from 8 slices ± S.E.M. (blue); no significant alterations in soma area where detected under control conditions. **B)** Soma area in hypoosmolar ACSF (~222 mOsm), slices were kept in isotonic ACSF for the first scan at t_0, then perfused with hypoosmolar ACSF after 5 min; left: MIP of SR101- stained astrocytes at t_0; middle: arrowheads point out to swollen areas (green) of the marked astrocyte at respective time points compared to t_0. After t_4= 40 min scan was taken, superfusion was returned to normal ACSF for control volume recovery; right: summary of soma area measurements of 48 cells from 7 slices ± S.E.M. (red); asterisks indicate significant alterations in soma area values compared to t_0 or next time point respectively. **C)** Soma area in hyperosmolar ACSF (~450 mOsm), the experimental setup resembles the experiment in B); left: MIP of SR101-stained astrocytes at t_0; middle: arrowheads point out to shrunken areas in red. After 40 min superfusion was returned to normal ACSF for control volume recovery. Right: Summary of cross-section soma area measurements of 32 cells from 4 slices ± SEM (purple); asterisks indicate significant alterations in soma area values compared to t_0. Cells did not return to control morphology. (**$p < 0.01$, *$p < 0.05$; *t*-Test; Scale bars: MIP: 30 µm, Overlay: 10 µm). [own image, Institute of Neurobiology, Düsseldorf]

experiments (Fig. 3.6 A, C). The comparison of baseline soma areas at t_0 determined in the three different experiments revealed no significant differences. The data for the following time point

t_1-t_5 showed significant difference from the control values, when the osmolar conditions were altered, but not under isotonic conditions (Fig. 3.6 B).

A simple volume calculation, based on the assumption of sphere geometry and a uniform expansion of the somata of the astrocytes in the x-, y- and z-dimension results in $V_0 = 184$ µm³, based on an soma area of 39.1 µm² at t_0 and $V_1 = 241$ µm³ based on $t_1 = 46.8$ µm² at t_2, what equals an increase by factor 1.31 when ASCF is changed from isotonic to hypotonic conditions,

A

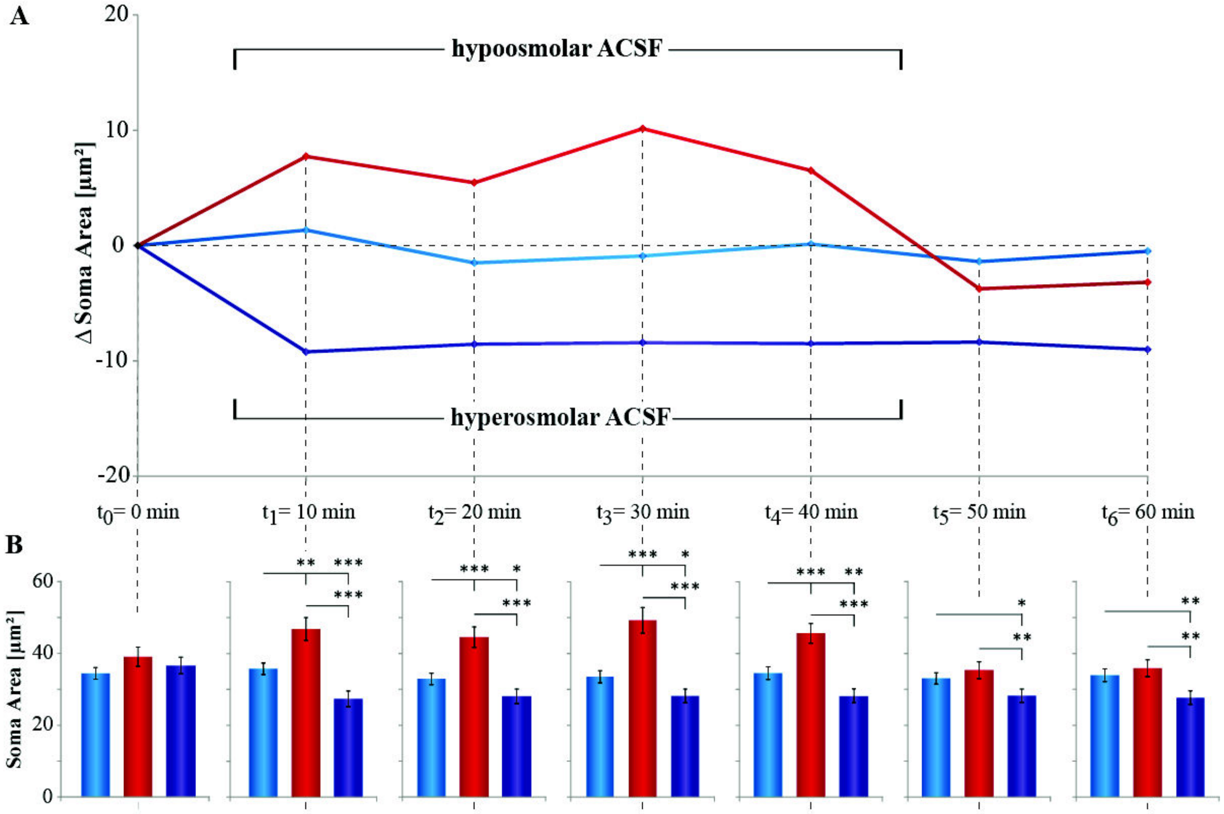

C

isotonic ACSF 🟦 34.4 ± 1.6 µm	35.8 ± 1.6 µm + 3.9 %	32.9 ± 1.6 µm - 4.4 %	35.5 ± 1.7 µm - 2.6 %	34.6 ± 1.8 µm + 0.4 %	33.0 ± 1.6 µm - 4.0 %	33.9 ± 1.8 µm - 1.5 %
hypoosmolar ACSF 🟥 39.1 ± 2.7 µm	46.8 ± 3.2 µm + 19.8 %	44.6 ± 2.9 µm + 13.9 %	49.2 ± 3.6 µm + 25.9 %	45.6 ± 2.7 µm + 16.6 %	35.3 ± 2.4 µm - 9.6 %	35.9 ± 2.4 µm - 8.2 %
hyperosmolar ACSF 🟦 36.6 ± 2.3 µm	27.4 ± 2.2 µm - 25.2 %	28.1 ± 2.0 µm - 23.4 %	28.2 ± 2.0 µm - 23.0 %	28.1 ± 2.0 µm - 23.2 %	28.2 ± 1.8 µm - 22.9 %	27.6 ± 1.9 µm - 24.6 %

Figure 3.6: **Short-term changes in astrocyte soma size in control experiments**. Further evaluation of the data presented in Fig. 3.5 **A)** Alterations in soma area of astrocytes in different ACSFs compared to control values at t_0. Hypo- or hyperosmolar ACSF were applied, as indicated between t_0 and t_1 and replaced with isotonic ACSF after 45 min, between t_4 and t_5. Cells in regular ACSF maintained their soma size as it was expected for control experiments (🟦). The hypoosmolar ACSF caused cell swelling, followed by cell shrinkage below t_0 control values when ACSF has been changed to isotonic again (🟥). Under hyperosmolar conditions cells shrink. After return to the isotonic ACSF, cells were not able to reestablish control values similar to t_0 (🟦). **B)** Comparison of soma areas for each time point. The application of hypo- or hyperosmolar ACSF leads to significant changes in astrocyte soma area. While cells in experiments providing hypoosmolar conditions were able to return to control values, astrocytes under hyperosmolar conditions remained significantly shrunken. **C)** Mean soma area values [µm²] ± S.E.M. for all shown experiments. Percentage changes compared to t_0 control values are shown for each time point (***$p < 0.001$, **$p < 0.01$, *$p < 0.05$, *t*-Test). [own image, Institute of Neurobiology, Düsseldorf]

with a decrement of the osmolarity from ~316 to ~222 mOsm by the factor 1.42. For the experiments in hyperosmolar ASCF the similar calculation reveals V_0 = 167µm³ based on 36.6 µm² at t0 and V1 = 108 µm² based on 27.4 µm² at t1, what equals a decrease by factor 0.65 when ACSF is changed from isotonic to hypertonic conditions, with an increment of the osmolarity by factor 1.42 (1/1.42 = 0.7). So, astrocytes in this experiment behave like an almost ideal osmometer, what is consistent with a statement by Pasantes-Morales (1996): "…the volume of cells exposed to anisosmotic fluids rapidly changes as a consequence of water fluxes tending to equalize the osmotic forces. Brain cells at the beginning behave as a perfect osmometer gaining water in a hyposmotic medium and losing water in a hyperosmotic medium".

3.3.2 Volume changes in long-term control experiments

In order to find out whether astrocytes in acute hippocampal slices can regulate their volume over a longer period of time, the experimental approach described above was modified: 1. the duration of the entire procedure was set to six hours; 14 measurements were done with scan intervals of 20 min in the first hour and 30 min between t_3 = 60 min and the end of the experiment at t_{13} = 360 min. 2. There was no return to regular ACSF after application of hypo- or hyperosmolar ACSFs to test how astrocytes respond to chronic osmotic perturbations.

In contrast to the short-term essay, cells in isotonic ACSF did, although not significantly, alter their volume during the first 40 min (t_0 - t_2) of the control experiment (Fig. 3.7 A). At time point t_3 = 60 min, cell soma area significantly decreased from initial 38.1 ± 1.8 µm² to 34.3 ± 1.4 µm² and it further dropped to 29.0 ± 4.1 µm² at t_5, but then increased again to 31.8 ± 3.3 µm² at t_7 (180 min), which was not significantly different from the value at t_0. Subsequently, the soma area decreased again to 26.1 ± 2.7 µm² at t_{12} = 330 min and then slightly increased to 27.4 ± 3.2 µm² at t_{13} = 360 min, the end of the experiment (n = 92, N = 12 for the first 90 min, n = 18, N = 3 for the following 270 min, ± S.E.M.).

The application of hypoosmolar ACSF induced a significant increase in soma area from 51.5 ± 1.5 µm² at t_0 to 62.2 ± 2.8 µm² at t_1, followed by a decrease at t_3 (60 min) to 55.5 ± 2.6 µm², which was not significantly different from the value at t_0. During the next 60 min cell somata swelled to a maximum of 67.3 ± 5.8 µm² at t_5 = 120 min, and then shrunk again to 60.8 ± 5.4 µm² at t_7 = 180 min. Until the end of the experiment, the soma area stayed elevated, but not significantly, compared to values measured at t_0 (Fig. 3.7 B). The overlay images also revealed obvious enlargements of the regarded cell for all time points relative to t_0 (n = 76, N = 10, ± S.E.M.; Fig. 3.7 B, overlay, arrowheads). Hyperosmolar ACSF caused a rapid and significant decrease in soma area from initial 45.6 ± 6.6 µm² to 26.9 ± 5.2 µm² at t_2 = 40 min. Soma area was further reduced to 17.1 ± 2.6 µm² after 180 min and fell, after a slight increase at t_9 (240 min), to an absolute minimum of 14.1 ± 2.2 µm² after 330 min (n = 8, N = 1, ± S.E.M. Fig. 3.7 C). The red areas (arrowheads) in the overlay images confirm this data.

The changes in soma area with respect to the initial soma area at t_0 under isotonic, hypotonic, and hypertonic conditions are shown in Fig. 3.8. Under isotonic conditions astrocytes shrunk by -31 % at the most during 360 min. Cell did not shrink continuously but rather showed an alternating de- and increase of soma area (Fig. 3.8 A and C). This phenomenon becomes more obvious when cells in hypoosmolar ACSF are regarded. After swelling significantly by +20 % as a first reaction, cells showed a RVD down to +7 % after 60 min, not significantly different from the value at t_0. Then, soma area values significantly rose again to +30 % at t_5 = 120 min. Afterwards, cell volume tended to slowly decrease again, but stayed enlarged with respect to t_0 (Fig. 3.8 A and C).

Hyperosmolar ACSF caused a massive shrinkage of about -40 % at t_1 = 20 min. Cell volume remained significantly decreased and became even smaller, down to a minimum of -69 % at t_{11} = 300 min. Here, the cells also showed an alternating de- and increase of soma area, as in the other experimental procedures (Fig. 3.8 A and C).

Regarding the soma areas in the three experimental setups (Fig. 3.8 B) it was conspicuous that the soma areas at t_0 differed remarkably from each other, although the slices were kept in almost the same isotonic ACSF. Thus, astrocytes later exposed to hypoosmolar ACSF had a significantly greater soma area then astrocytes kept in regular ACSF throughout the experiment. The soma area of astrocyte later exposed to hypoosmolar ACSF was also larger, but this was not significant. Hyperosmolar conditions caused a significant decrease in cell volume, but when between t_0 the data obtained under isotonic and hyperosmolar conditions were compared, a significant difference could be found not until t_7 = 180 min. This might be due to high standard deviations because of low quantities of analyzed cells in hyperosmolar experiments.

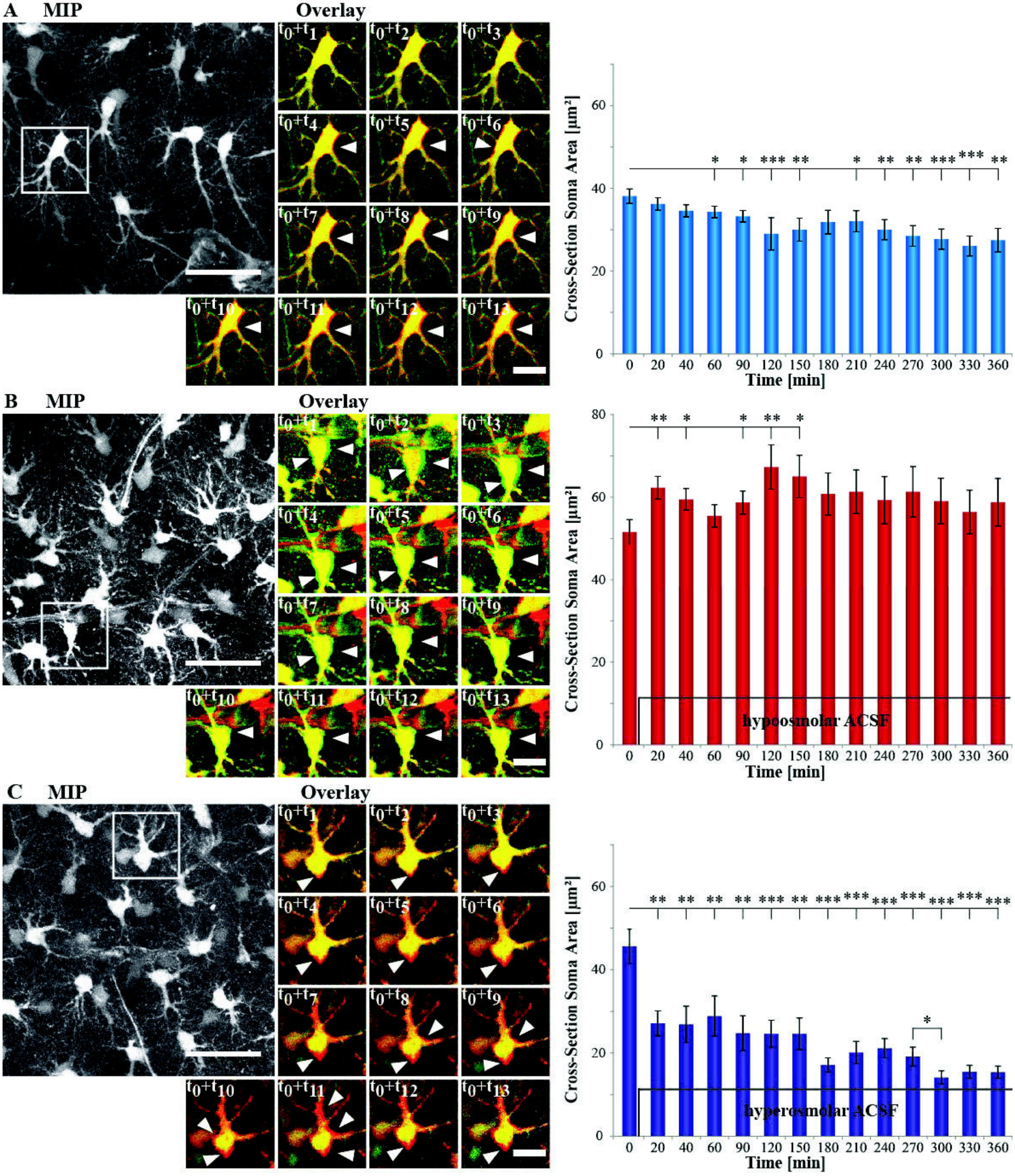

Figure 3.7: **Changes of astrocyte soma area in long-term experiments.** Experiments lasted for 6 h, scans were taken every 20 min over the initial 60 min and every 30 min until the end of the experiment. **A)** Soma area in isotonic ACSF (130 mM NaCl, ~316 mOsm); left: MIP image of SR101-stained astrocytes in *stratum radiatum*. The marked cell was taken for overlay illustration (middle) of different time points, the red channel shows the astrocyte at t_0, the green channel at t_2-t_6. Yellow indicates an overlay, green areas cell swelling and red areas cell shrinking; right: summary of soma area measurements (n = 92, N = 12 for the first 90 min, n = 18, N = 3 for the following 270 min ± S.E.M., blue). **B)** Soma area in hypoosmolar ACSF (~220 mOsm), slices were kept in isotonic ACSF for the first scan at t_0, then perfused with hypoosmolar ACSF after 5 min; left: MIP of SR101-stained astrocytes at t_0; middle: arrowheads point out to swollen areas (green) at respective time points compared to t_0; right: summary of soma area measurements (n = 7, N = 10, ± S.E.M., red); asterisks indicate significant changes in measured soma area compared to t_0 or next time point. **C)** Soma area in hyperosmolar ACSF (~450 mOsm), the experimental setup resembles the experiment in B); left: MIP of SR101 stained astrocytes at t_0; middle: arrowheads point out to shrunken areas in red; right: Summary of soma area measurements (n = 8, N = 1, ± S.E.M., purple); asterisks indicate significant changes in soma area compared to t_0. (***$p < 0.001$, **$p < 0.01$, *$p < 0.05$, *t*-Test; scale bars: MIP: 30 µm, Overlay: 10 µm). [own image, Institute of Neurobiology, Düsseldorf]

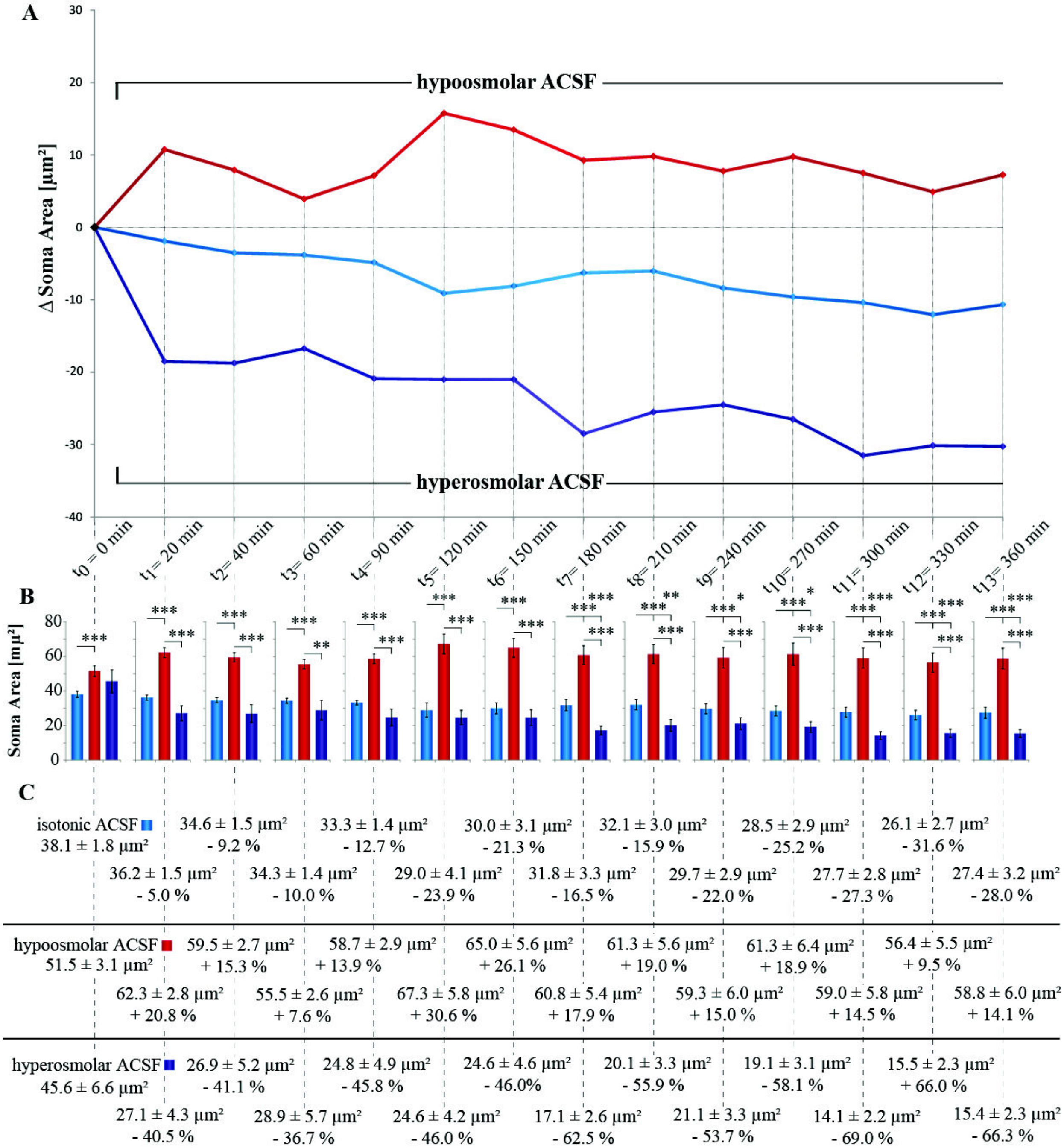

isotonic ACSF ▪ 38.1 ± 1.8 µm²
34.6 ± 1.5 µm² - 9.2 % | 33.3 ± 1.4 µm² - 12.7 % | 30.0 ± 3.1 µm² - 21.3 % | 32.1 ± 3.0 µm² - 15.9 % | 28.5 ± 2.9 µm² - 25.2 % | 26.1 ± 2.7 µm² - 31.6 %
36.2 ± 1.5 µm² - 5.0 % | 34.3 ± 1.4 µm² - 10.0 % | 29.0 ± 4.1 µm² - 23.9 % | 31.8 ± 3.3 µm² - 16.5 % | 29.7 ± 2.9 µm² - 22.0 % | 27.7 ± 2.8 µm² - 27.3 % | 27.4 ± 3.2 µm² - 28.0 %

hypoosmolar ACSF ▪ 51.5 ± 3.1 µm²
59.5 ± 2.7 µm² + 15.3 % | 58.7 ± 2.9 µm² + 13.9 % | 65.0 ± 5.6 µm² + 26.1 % | 61.3 ± 5.6 µm² + 19.0 % | 61.3 ± 6.4 µm² + 18.9 % | 56.4 ± 5.5 µm² + 9.5 %
62.3 ± 2.8 µm² + 20.8 % | 55.5 ± 2.6 µm² + 7.6 % | 67.3 ± 5.8 µm² + 30.6 % | 60.8 ± 5.4 µm² + 17.9 % | 59.3 ± 6.0 µm² + 15.0 % | 59.0 ± 5.8 µm² + 14.5 % | 58.8 ± 6.0 µm² + 14.1 %

hyperosmolar ACSF ▪ 45.6 ± 6.6 µm²
26.9 ± 5.2 µm² - 41.1 % | 24.8 ± 4.9 µm² - 45.8 % | 24.6 ± 4.6 µm² - 46.0% | 20.1 ± 3.3 µm² - 55.9 % | 19.1 ± 3.1 µm² - 58.1 % | 15.5 ± 2.3 µm² + 66.0 %
27.1 ± 4.3 µm² - 40.5 % | 28.9 ± 5.7 µm² - 36.7 % | 24.6 ± 4.2 µm² - 46.0 % | 17.1 ± 2.6 µm² - 62.5 % | 21.1 ± 3.3 µm² - 53.7 % | 14.1 ± 2.2 µm² - 69.0 % | 15.4 ± 2.3 µm² - 66.3 %

Figure 3.8: **Long-term changes in astrocyte soma size in control experiments.** Further evaluation of the data presented in Fig. 3.7. **A**) Alterations in soma area of astrocytes in different ACSFs compared to control values at t_0. **B**) Comparison of soma area values of the experiments for each time point. The application of hypo- and hyperosmolar ACSF leads to significant changes in astrocyte soma area. **C)** Mean soma area values [µm²] ± S.E.M. for all shown experiments. Percentage changes compared to t_0 control values are shown for each time point (***$p < 0.001$, **$p < 0.01$, *$p < 0.05$, *t*-Test). [own image, Institute of Neurobiology, Düsseldorf]

3.3.3 The role of NKCC1 in volume changes

After having successfully tested how astrocytes in acute hippocampal slices react to alterations in extracellular osmolarity, and having shown that even relatively small changes in soma area could be detected, the next step was to examine the behavior of the cells, when a major component of the cellular volume regulation mechanism was pharmacologically inhibited. Therefore, the loop diuretic bumetanide, which blocks the Na^+-K^+-Cl^--cotransporter 1 (NKCC1), was added to the ACSF and the soma area was measured over 90 min, with scan intervals of 20 min during the first 60 min and a final 30 min interval. Two experimental approaches were carried out: 1) the measurement of astrocyte soma area with inhibition of the NKCC1 with bumetanide while osmotic conditions remain unaltered, 2) the measurement of astrocyte soma area with inhibition of the NKCC1 with bumetanide when extracellular osmolarity was changed.

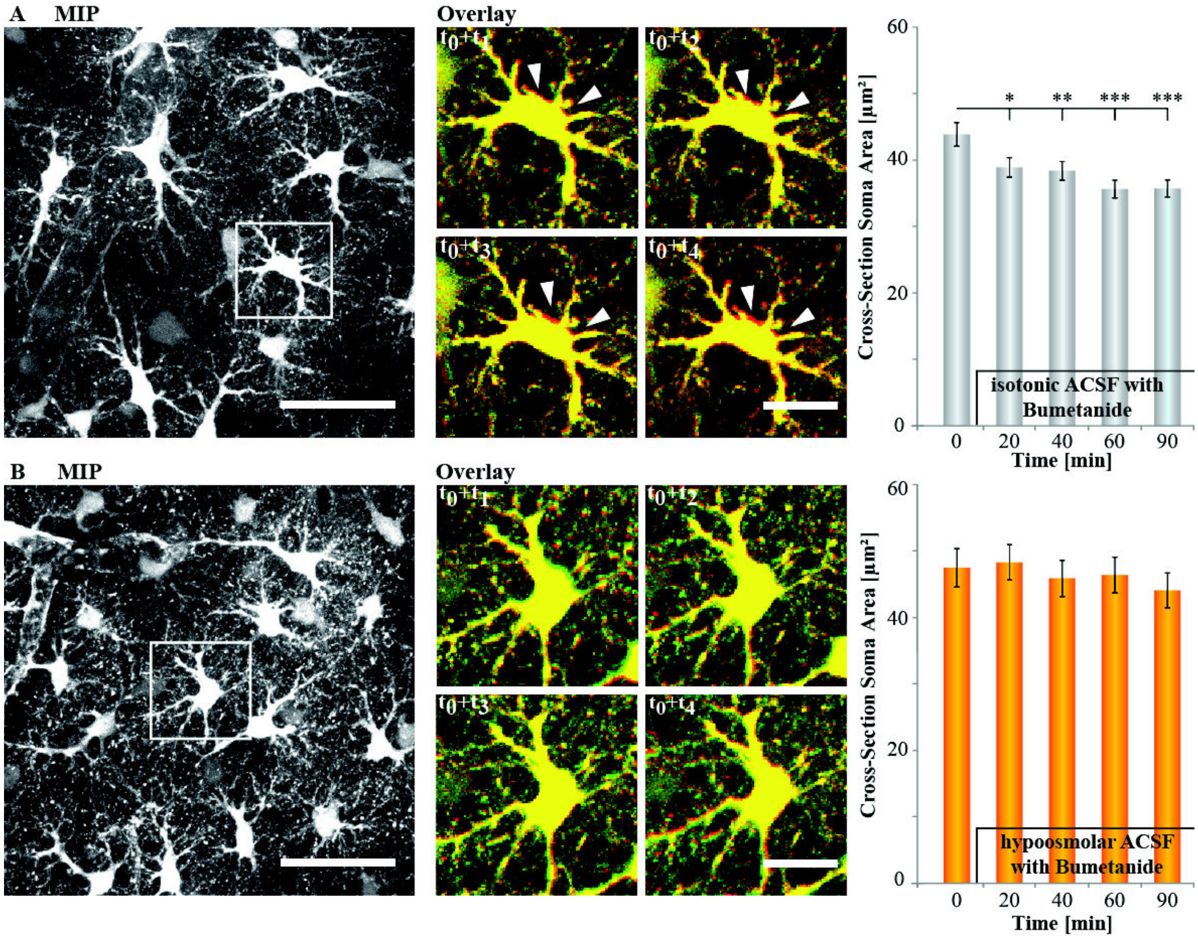

Figure 3.9: **Influence of bumetanide on the volume of astrocytes.** The function of NKCC1 was blocked by addition of 100 µM bumetanide to the applied ACSFs. Cells were observed for 90 min with scan intervals of 20 min over the first 60 min (t_1 – t_3) and 30 min until 90 min (t_3 – t_4). **A)** MIP, overlay images and soma area values of astrocytes in isotonic ACSF with bumetanide. Cells shrink significantly within 90 min, compared to t_0. **B)** As A), but in hypoosmolar ACSF with bumetanide. Cell swelling, under hypotone conditions (see Fig. 3.7 B), was completely abolished. (***$p < 0.001$, **$p < 0.01$, *$p < 0.05$, *t*-test; scale bars: MIP: 30 µm, Overlay: 10 µm). [own image, Institute of Neurobiology, Düsseldorf]

The first experiment was carried out by adding 100 µM bumetanide to the isotonic ACSF, in the second experiment, 100 µM bumetanide was added to hypoosmolar ACSF. The results show that the inhibition of NKCC1 led to significant decrease in astrocyte soma area, from 43.8 ± 1.8 µm² at t_0 to 38.9 ± 1.5 µm² at t_1 = 20 min (Fig. 3.9 A). This reduction continued in the following: 38.4 ± 1.4 µm² at t_2 = 40 min, 35.6 ± 1.4 µm² at t_3 = 60 min, and 35.7 ± 1.3 µm² at t_4 = 90 min (Fig. 3.9 A). The overlay images for the different time points confirmed this reduction in soma area. In hypoosmolar ACSF bumetanide completely prevented astrocytes from swelling, as observed without pharmacological NKCC1 inhibition (Fig. 3.9 B). After a small soma increase from 47.5

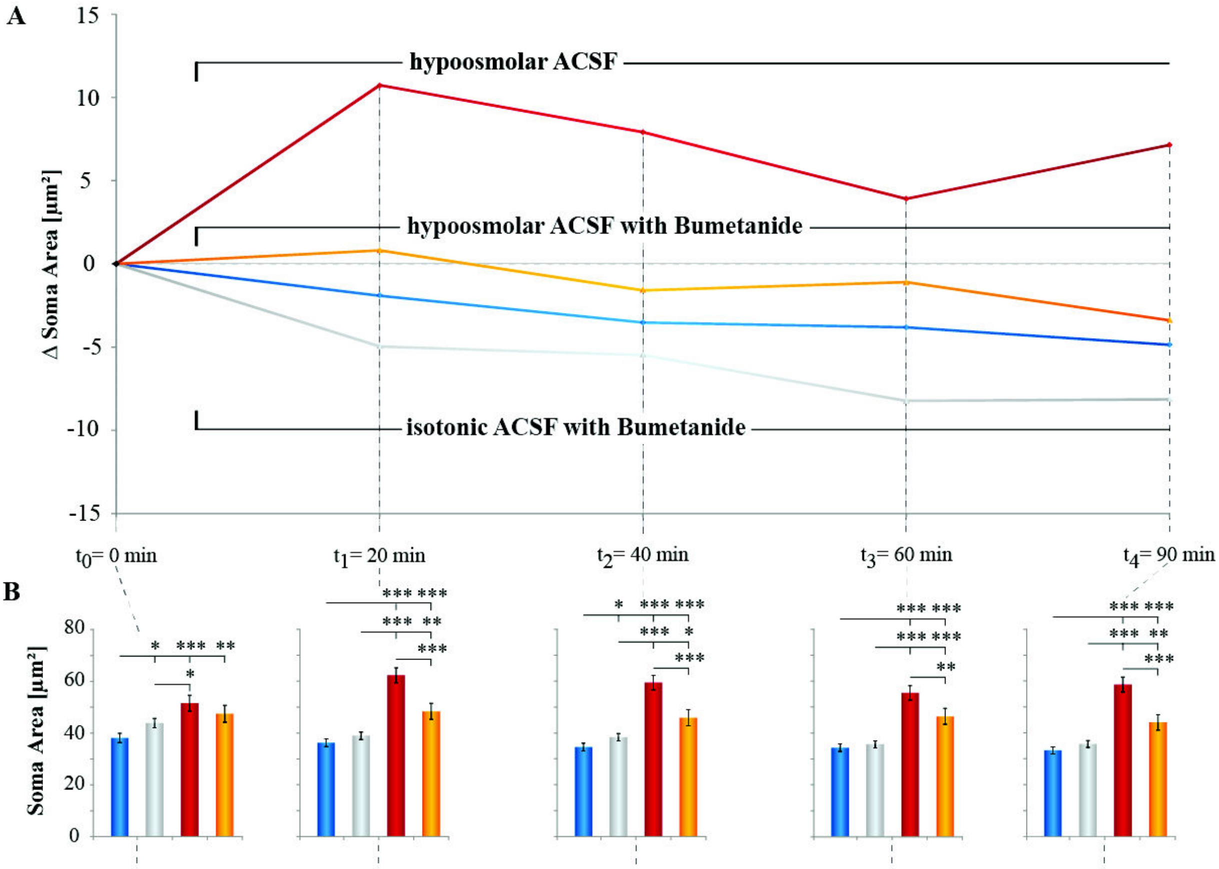

C

isotonic ACSF 🟦 38.1 ± 1.8 µm²	36.2 ± 1.5 µm² - 5.0 %	34.6 ± 1.5 µm² - 9.2 %	34.3 ± 1.4 µm² - 10.0 %	33.3 ± 1.4 µm² - 12.7 %
isotonic ACSF ⬜ with Bumetanide 43.8 ± 1.8 µm²	38.9 ± 1.5 µm² - 11.3 %	38.4 ± 1.4 µm² - 12.5 %	35.6 ± 1.4 µm² - 18.8 %	35.7 ± 1.3 µm² - 18.6 %
hypoosmolar ACSF 🟥 51.5 ± 3.1 µm²	62.3 ± 2.8 µm² + 20.8 %	59.5 ± 2.7 µm² + 15.3 %	55.5 ± 2.6 µm² + 7.6 %	58.7 ± 2.9 µm² + 13.9 %
hypoosmolar ACSF 🟧 with Bumetanide 47.5 ± 3.3 µm²	48.3 ± 3.1 µm² + 1.7 %	45.9 ± 3.1 µm² - 3.4 %	46.4 ± 3.1 µm² - 2.3 %	44.1 ± 3.0 µm² - 7.2 %

Figure 3.10: **Bumetanide treatment influences the volume of astrocytes.** Additional evaluation of the data presented in Fig. 3.9 **A)** Alterations in soma area of astrocytes in different ACSFs compared to control values at t_0. **B)** Comparison of soma area values of the experiments for each time point. **C)** Mean soma area values [µm²] ± S.E.M. for all shown experiments. Percentage changes compared to t_0 control values are shown for each time point (***$p < 0.001$, **$p < 0.01$, *$p < 0.05$, *t*-Test). [own image, Institute of Neurobiology, Düsseldorf]

± 3.3 µm² at t_0 to 48.3 ± 3.1 µm² at t_1 = 20 min, the soma area decreased to 45.9± 3.1 µm² at t_2, 46.4 ± 3.1 µm² at t_3 and to 44.1 ± 3.0 µm² at t_4 = 90 min. The overlay images confirmed these results (Fig. 3.9 B). Regarding the differences in soma area the effect of bumetanide becomes more obvious (Fig. 3.10 A). Compared to t_0, the soma area in isotonic ACSF decreased by -5 %, -9 %, -10 % and -12 % during the 90 min of the experiment. In the presence of bumetanide the soma area decreased by -11 %, -12 %, -18 % and -18 %. The hypoosmolar ACSF caused an increase in soma area by +20 %, +15 %, +7 % and +13 % (Fig. 3.10 C), in the presence of bumetanide the soma area changed by +1 %, -3 %, -2 % and -7 % (Fig. 3.10 C). Comparison of the soma areas at the beginning of the experiments shows a significant difference between isotonic ACSF experiments and the other approaches, although the conditions were similar. Isotonic ACSF soma area (blue) significantly deviates from soma areas, measured in other experiments, which makes a direct comparison of the results difficult. The obtained results varied between 38.1 ± 1.8 µm² (blue), 43.8 ± 1.8 µm² (gray), 47.5 ± 3.3 µm² (red) and 51.5 ± 3.1 µm² (orange) at t_0 (Fig. 3.10 C). There was no significant difference between the soma areas in bumetanide experiments at t_0 (gray, orange), but between those measured in isotonic ACSF with bumetanide (gray) and hypoosmolar ACSF (orange, Fig. 3.10 B). As a consequence, soma areas measured in isotonic ACSF and isotonic ACSF plus bumetanide cannot be directly compared, but relative changes and differences from the initial value can be used. In contrast, the direct comparison of soma areas measured in hypoosmolar ACSF and in hypoosmolar ACSF plus bumetanide demonstrates the difference in volume regulation behavior, in that bumetanide significantly prevented cell swelling as a reaction to hypoosmolarity.

3.3.4 The effect of NH_4^+ on volume changes

Since NH_4^+ leads to the swelling of astrocytes and hence brain edema, the time course of this process is of great interest in order to understand it´s pathophysiology.

To investigate how astrocytes react to pathologic amounts of NH_4^+, as they can be found in the brain of rats with induced ALF (Swain et al. 1992)., three approaches were used: 1. application of 5 mM NH_4^+ in ACSF in short term experiments, 2. application of 5 mM NH_4^+ in ACSF in long term experiments and 3. and application of 5 mM NH_4^+ plus bumetanide in ACSF over 90 min.

The application of 5 mM NH_4^+ (~312 mOsm) had no effect on the soma area of astrocytes during the first 40 min. Starting with 40.7 ± 6.9 µm², cell swelled minimally after transition to NH_4^+-

ACSF to 41.3 ± 6.5 µm² at t_1 and 41.4 ± 6.6 µm² at t_2, followed by a slight decrease to 38.3 ± 6.0 µm² at t_3 and 38.3 ± 5.9 µm² at t_4. The return to isotonic ACSF resulted in 37.3 ± 5.3 µm² soma area at t_5 and 37.2 ± 4.8 µm² at t_6 at the end of the experiment. These values were not significantly different from each other (n= 36, N= 5, Fig. 3.11 A).

In long-term experiments with NH_4^+-ACSF alternating de- and increases of soma area were observed, as seen before in long-term experiments (Fig. 3.7 B). Starting with 37.6 ± 1.4 µm² at t_0, after transition to NH_4^+-ACSF the soma area decreased to 35.5 ± 1.1 µm² at t_1; this reduction continued and became significant at t_2 with 34.4 ± 1.1 µm² and t_3 with 32.9 ± 1.1 µm² soma area. Then soma area started to re-increase at t_4 = 90 min to 34.3 ± 1.1 µm². This increase became maximal at t_5 with 36.6 ± 2.8 µm² and t_6 with 36.4 ± 2.9 µm². These values were not statistically different from that at t_0. During the next 120 min soma area decreased again to 33.0 ± 2.6 µm² at t_8, followed by another increase to 34.7 ± 2.8 µm² at t_{10}. Until t_{13} at the end of the experiment, the soma area decreased to 33.7 ± 2.8 µm². Although clearly visible red areas in overlay images indicate cell shrinkage, soma areas between t_5 and t_{13} were not statistically different from that at t_0 (Fig. 3.11 B). In this case, n = 107 cells and N = 13 slices for the first 90 min, n= 45 cells and N = 7 slices for the remaining 270 min of the experiment were evaluated. In the presence of 100 µM bumetanide plus 5 mM NH_4^+ in ACSF (~314 mOsm) the soma area continuously decreased over 90 min. At the beginning of the experiment, soma area was 35.9 ± 1.5 µm², which dropped to 34.5 ± 1.4 µm² at t_1 and then further to 32.1 ± 1.4 µm at t_2, 30.9 ± 1.3 µm² at t_3 and 31.0 ± 1.4 µm² at the end of the experiment (Fig. 3.11 C, n = 110, N = 16). The overlay images verify these results, in that they show clearly visible red areas.

In long term experiments, the changes in soma areas in isotonic ACSF, NH_4^+-ACSF, and NH_4^+-ACSF plus bumetanide showed an alternating de- and increase of cell volume (Fig. 3.12 A). During the first 40 min of the experiment the soma area decreased by -9 %, -8 % and -10 %. At t_3 = 60 min, the area values started to diverge, showing a reduction of -14 % in NH_4^+-ACSF plus bumetanide but of only -10 % in isotonic ACSF, which was significantly smaller.

Treatment with NH_4^+ alone caused a soma area reduction of -12 %, which was not significantly different from the other two values. Significant differences between NH_4^+-ACSF (-9 %) and NH_4^+-ACSF plus bumetanide (-13 %) occurred at t_4 = 90 min, whereas soma areas in isotonic ACSF (-12 %) turned out to be not significantly different from the other two soma areas (Fig. 3.12 B). Divergence between control and NH_4^+ experiments reaches a maximum at t_5 = 120 min, where control values decreased to -23 % and NH_4^+-treatment caused an re-increase in soma area to -2 %. This alternating de- and increase of cell volume continued and soma area converged and approximated maximal at t_8 (- 15 % in regular ACSF and -12 % in NH_4^+-ACSF).

Then again, soma area values departed and became significantly different at time points t_{11} and t_{12}, where cells in isotonic ACSF shrunk to -27 % and -31 %, whereas astrocytes in NH_4^+-ACSF showed soma values of -8 % and -10 % (Fig. 3.12 A, B, C).

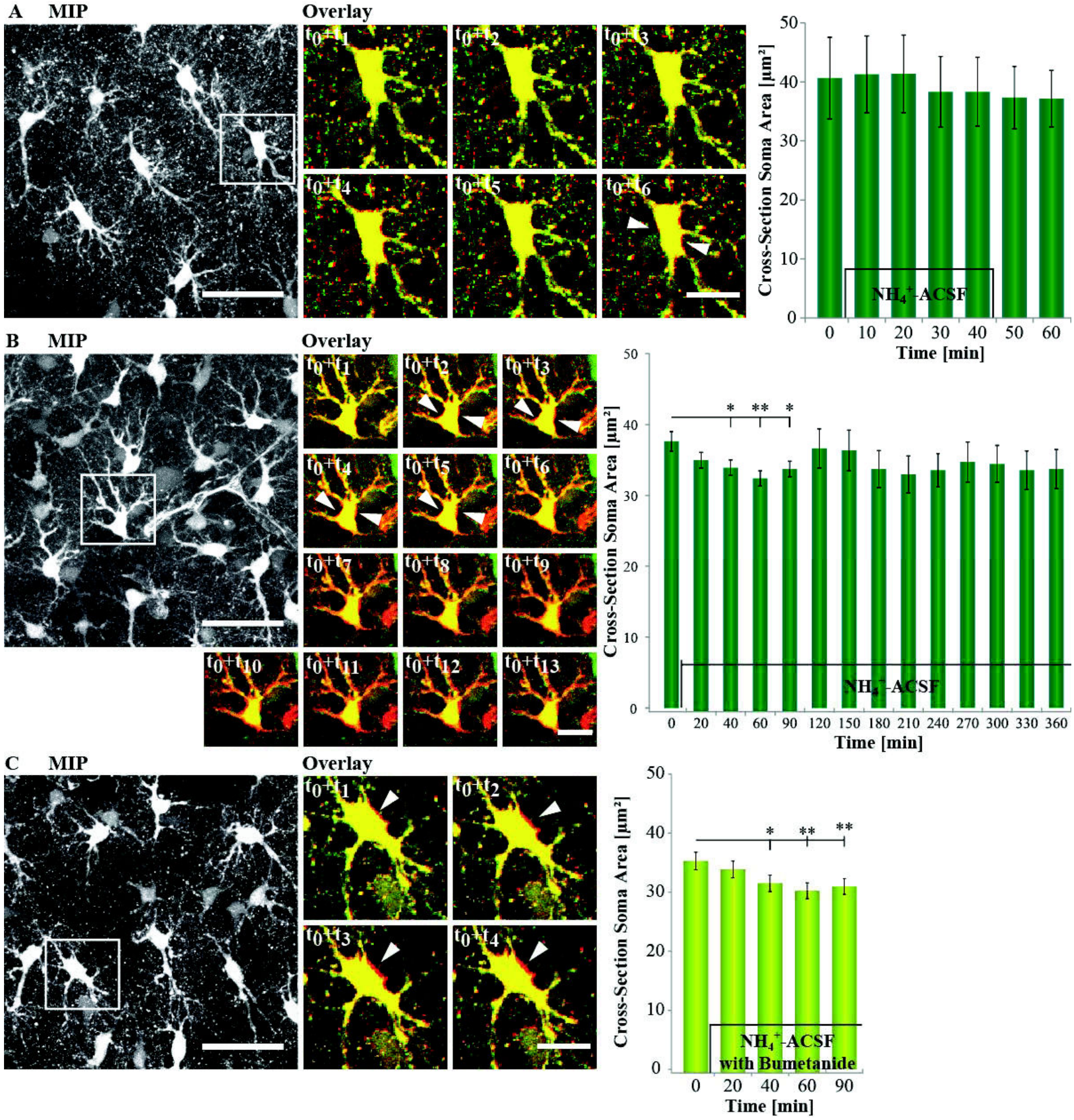

Figure 3.11**: Volume of astrocytes in the presence of NH_4^+ and bumetanide.** Cells were exposed to 5 mM NH_4^+ added to the applied ACSF. Short time experiments (1h, scan interval 10 min), long time experiments (6h, scan intervals 20 min to 30 min, as described above) and pharmacological inhibition experiments with 100 µm bumetanide (90 min, scan intervals 20 min to 30 min) were carried out. **A)** MIP, overlay images and soma areas of astrocytes in short term experiments. NH_4^+-ACSF was applied between t_1 and t_4. Cell volume remained constant over 60 min. **B)** as A), but in long term experiments. Transition to NH_4^+-ACSF was executed between t_0 and t_1. Soma area decreased significantly during the first 90 min, then it increased, and exhibited an alternating de- and increase of soma area, but remained insignificantly different from starting value at t_0. **C)** As A), but cells were treated with 100 µM bumetanide added to the 5 mM NH_4^+-ACSF that has been applied between t_0 and t_1 until the end of the experiment. Cells showed a continuous and significant decrease in soma area during 90 min experiments. (**$p < 0.01$, *$p < 0.05$, *t*-Test; Scale bars: MIP: 30 µm, Overlay: 10 µm). [own image, Institute of Neurobiology, Düsseldorf]

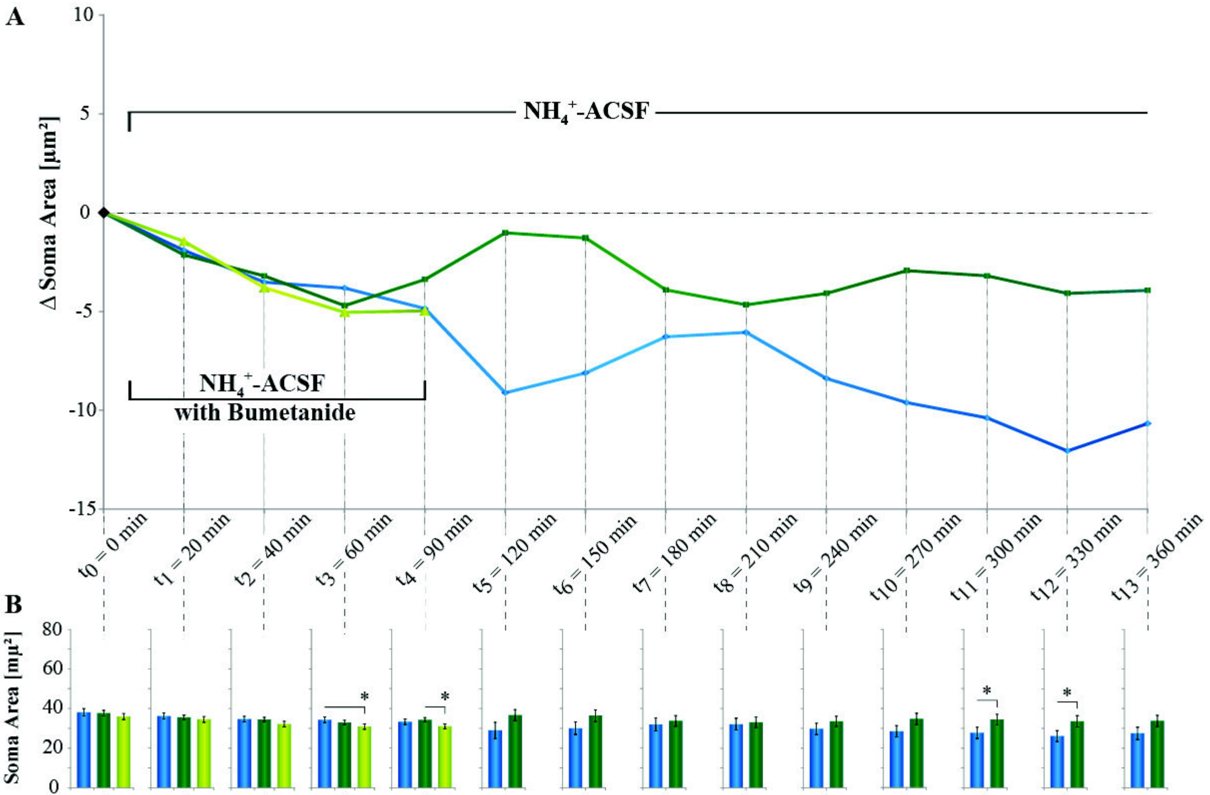

C

isotonic ACSF 🟦	38.1 ± 1.8 µm²	36.2 ± 1.5 µm² - 5.0 %	34.6 ± 1.5 µm² - 9.2 %	34.3 ± 1.4 µm² - 10.0 %	33.3 ± 1.4 µm² - 12.7 %	29.0 ± 4.1 µm² - 23.9 %	30.0 ± 3.1 µm² - 21.3 %	31.8 ± 3.3 µm² - 16.5 %	32.1 ± 3.0 µm² - 15.9 %	29.7 ± 2.9 µm² - 22.0 %	28.5 ± 2.9 µm² - 25.2 %	27.7 ± 2.8 µm² - 27.3 %	26.1 ± 2.7 µm² - 31.6 %	27.4 ± 3.2 µm² - 28.0 %
NH$_4^+$-ACSF 🟩	37.6 ± 1.4 µm²	35.5 ± 1.1 µm² - 5.7 %	34.4 ± 1.1 µm² - 8.5 %	32.9 ± 1.1 µm² - 12.5 %	34.3 ± 1.1 µm² - 9.0 %	36.6 ± 2.8 µm² - 2.7 %	36.4 ± 2.9 µm² - 3.4 %	33.7 ± 2.6 µm² - 10.4 %	33.0 ± 2.6 µm² -12.4 %	33.6 ± 2.4 µm² - 10.9 %	34.7 ± 2.8 µm² - 7.8 %	34.4 ± 2.6 µm² - 8.5 %	33.6 ± 2.7 µm² - 10.9 %	33.7 ± 2.8 µm² - 10.4 %
NH$_4^+$-ACSF 🟩 with Bumetanide	35.9 ± 1.5 µm²	34.5 ± 1.4 µm² - 4.0 %	32.1 ± 1.4 µm² - 10.6 %	30.9 ± 1.3 µm² - 14.0 %	31.0 ± 1.4 µm² - 13.8 %									

Figure 3.12: **Volume of astrocytes in the presence of 5 mM NH$_4^+$ and bumetanide.** Results of experiments carried out in isotonic ACSF, NH$_4^+$-ACSF and NH$_4^+$-ACSF plus bumetanide were presented as Δ soma area, compared between the different time points and as mean soma area in [µm²], as well as relative changes for each time point. **A)** Δ soma areas show a more or less uniform decrease in all experimental approaches for the first 90 min. then soma areas showed an alternating de- and increase of the soma area, whereas cells in isotonic and NH$_4^+$-ACSF had an antithetic behavior. In contrast to astrocytes in control experiments, which continuously decreased in soma area, NH$_4^+$-treated cells remained, although slightly decreased not significantly smaller than in the beginning of the experiment. **B)** Comparison of soma area values of the experiments for each time point. **C)** Mean soma area values [µm²] ± S.E.M. for all shown experiments. Percentage changes compared to t_0 control values are shown for each time point (**p* < 0.05, *t*-Test). [own image, Institute of Neurobiology, Düsseldorf]

3.4 Lesion-induced changes in astrocyte morphology

3.4.1 Organotypic hippocampal slice cultures of GFP/GFAP-expressing mice

For the examination of chronic volume changes, slice cultures turned out to be an appropriate model system. The use of cultured mouse hippocampal tissue slices (organotypic hippocampal slice cultures, OHSC) provides the typical layering and basic cellular organization that can be found in this brain region and retains these properties over a certain period of time (Stoppini et al. 1991).

During the first 19 to 25 days *in vitro* (DIV), slice tissue underwent a reduction of thickness from 200 µm to ~ 50 µm, containing three or four cell layers. Propidium iodide assay were taken to proof the viability of cells and the stability of the culture system (data not shown). They confirmed that the slice cultures were vital, providing minimal cell death within the regions of interest. The usage of transgenic mice expressing green fluorescent protein (GFP) under the control of the glial fibrillary acidic protein (GFAP) promoter (FVB/N-Tg[GFAP/GFP]) served as potent tool for the visualization of astrocyte specific morphology (Schreiner et al. 2013; Fig. 3.12 A).

The GFP fluorescence pattern of tissue cultures prepared from this GFP/GFAP mice confirmed that the typical arrangement of astrocytes in the CA1 *strata pyramidale* and *radiatum* was preserved in this culture system (Benediktsson et al. 2005, Lushnikova et al. 2009; Fig. 3.13 B). Examination of slice cultures at higher magnification showed that the morphology of single GFP-

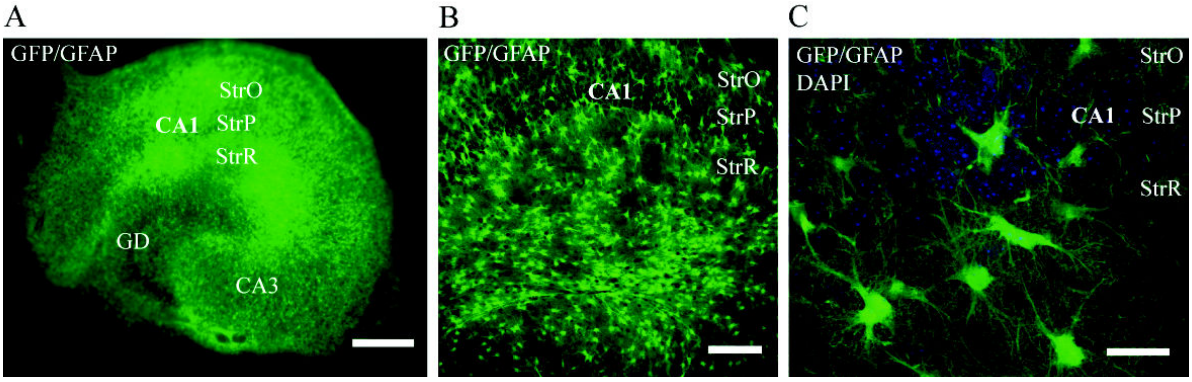

Figure 3.13: **Organotypic hippocampal slice culture. A)** Overview of an OHSC of GFP/GFAP expressing mice. Layering and cellular organization of the hippocampal formation are visible. **B)** Overview of the CA1 region of an OHSC. Note the typical distribution of fluorescent astrocytes in the *strata oriens* (StrO) and *radiatum* (StrR) and the free spaces in *stratum pyramidale* (StrP), due to somata of pyramidal neurons. **C)** Higher magnification of the CA1 region. The morphology of fluorescent astrocytes in the StrR (green) and DAPI-stained nuclei of pyramidal neurons in the StrP (blue) are visible. Scale bars: (A) 300 µm, (B) 100 µm, (C) 20 µm. [own image, Institute of Neurobiology, Düsseldorf]

expressing astrocytes was clearly visible and suited for the examination of changes in shape and volume of these cells (Fig. 3.13 C).

3.4.2 Astrocyte morphology following mechanical lesion

Reactivity of astrocytes and the development of astrogliosis, as they were to investigate in these experiments, was induced by setting a mechanical lesion. A sterile scalpel blade was used to cut through the *strata oriens*, *pyramidale* and *radiatum* at the CA1 region of cultured hippocampal slices under semisterile conditions (Fig. 3.14 A, B, C). Afterwards, the slices were returned into culture and cell morphology was observed six to seven days later.

For the characterization of reactive gliosis induced by the lesion, soma areas of fluorescent astrocytes in control and lesioned slices from GFP/GFAP-expressing mice were analyzed. Slice cultures were imaged with confocal microscopy and spatial resolution was calculated by adjusting the pixel/µm ratio. Somata were manually encircled and the resulting area was calculated. Results were discriminated between soma area of cells next to the lesion site (scar),

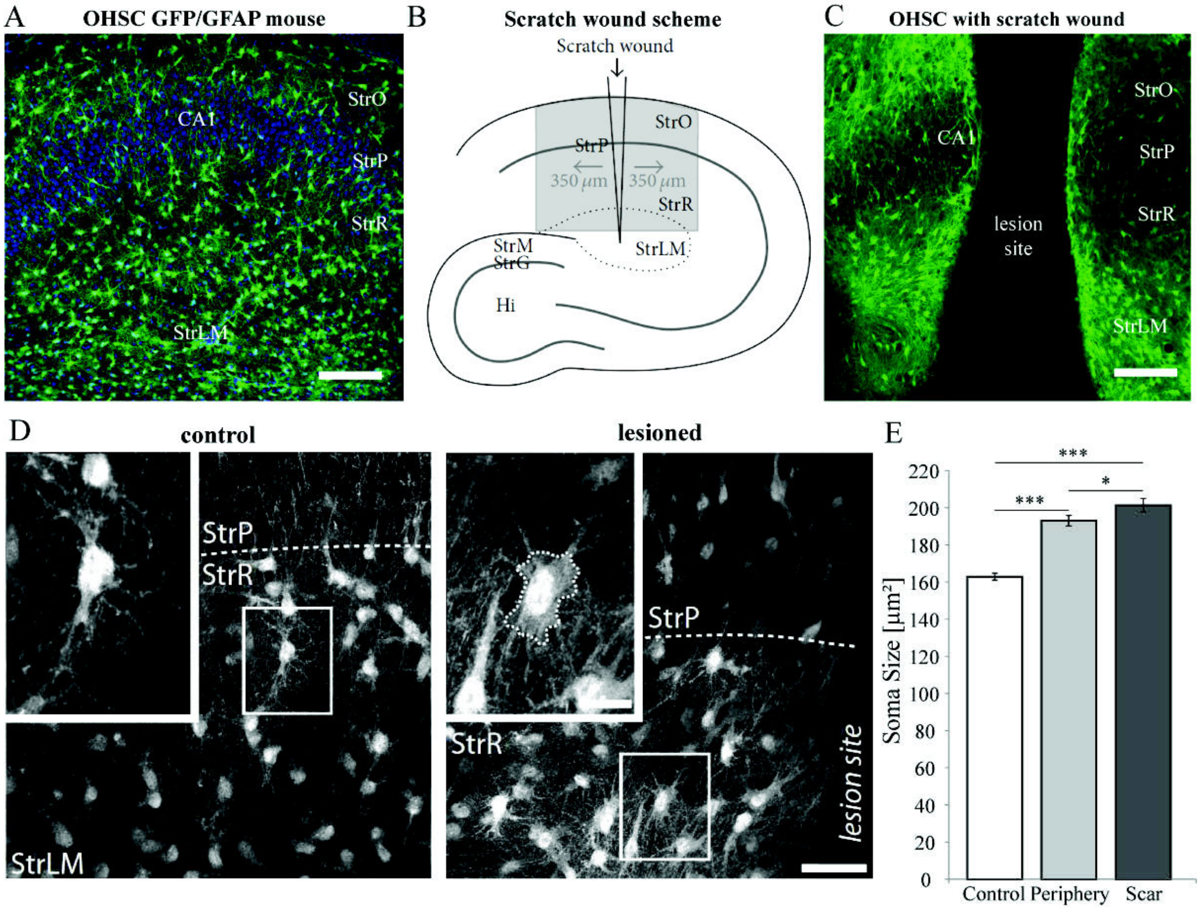

Figure 3.14: for explanation see next page.

Figure 3.14**: Scratch wound model for the induction of astrogliosis in organotypic slice cultures of GFP/GPAP-expressing mice. A)** Confocal image of an unlesioned organotypic hippocampal slice culture (OHSC) of a GFP/GFAP expressing mouse. Distinct layering and clear astrocyte and neuronal organization pattern is visible. (own image, Institute of Neurobiology, Düsseldorf) **B)** Schematic illustration of the performed scratch wound within the hippocampus formation and the region of interest for the measurement of soma areas in direct proximity as well as in the periphery of the lesion site (from Schreiner et al. 2014). **C)** Confocal image of a lesioned OHSC. The lesion site is clearly visible as a prominent gap within the culture tissue. The layering and cellular organization is still recognizable, as well as the glial scar, indicated by a strong GFP fluorescence (courtesy of Alexandra Schreiner). **D)** Confocal images of GFP fluorescence in cultured slices obtained from GFP/GFAP transgenic animals under control conditions (*left*) and subjected to a lesion (*right*). Cells surrounded by boxes are shown in the insets at higher magnification, and the dashed lines around the soma indicate the areas which served to determine their size. **E)** Quantification of soma area based on GFAP/GFP fluorescence in control and lesioned slices. The soma size increased both in astrocytes in the scar region (“scar”) and in astrocytes in the periphery of the lesion (“periphery”, D) and E) from Schreiner et al. 2014). StrP, *stratum pyramidale*; StrR, *stratum radiatum*; StrLM, *stratum lacunosum moleculare*. (***$p < 0.001$, *$p < 0.05$, scale bars: (A), (C): 100 µm, (D): 40 µm and 10 µm (inset)).

cells in the periphery, in distances of 100 to 350 µm to the scratch wound (periphery) and soma areas of astrocytes in unlesioned slices (control).

Astrocytes in direct proximity to the lesion site showed an increase in soma area of 24 % and astrocytes in the periphery of the scratch an increase of 18 %, compared to astrocytes in control slices (control: 163 ± 2 µm^2; n = 945, lesion periphery: 193 ± 3 µm^2, n = 496; scar tissue: 201 ± 4 µm^2, n = 439; N = 7, control; N = 9 lesioned slices; Fig. 3.14 D, E).

This chronic increase in soma size represents, besides an increase in GFAP and S100ß expression (Schreiner et al. 2013), a defined characteristic of reactive gliosis after mechanical lesion. The results confirm that the mechanical lesion model in organotypic hippocampal slice cultures of GFP/GFAP expressing mice is a practical tool for the examination of the development of a glial scar accompanied by a strong activation of astrocytes and appearance of astrogliosis (Schreiner et al. 2013).

3.5 Staining pattern of GFAP and S100ß in Aß-S8C dimer expressing mice

In order to investigate whether the overexpression of Aß-S8C dimer, which plays a key role in the pathology of Alzheimer’s disease, causes an activation of astrocytes and hence might be responsible for the development of astrogliosis in the hippocampus formation of aged mice, hippocampi of transgenic animals where examined. These mice (C57BL/6N background) express the human APP751, including the familial Swedish and the Aß dimer mutation (Aß-S8C), under the control of the neuron-specific Thy1-promoter and were called “tgDimer”.

PFA-fixed slices of 15 to 16 months old mice were used and immunohistochemical double staining against astrocyte-specific GFAP and S100ß was carried out, as well as staining with DAPI. GFAP immunoreactivity was quantified by measuring the distribution of gray values per

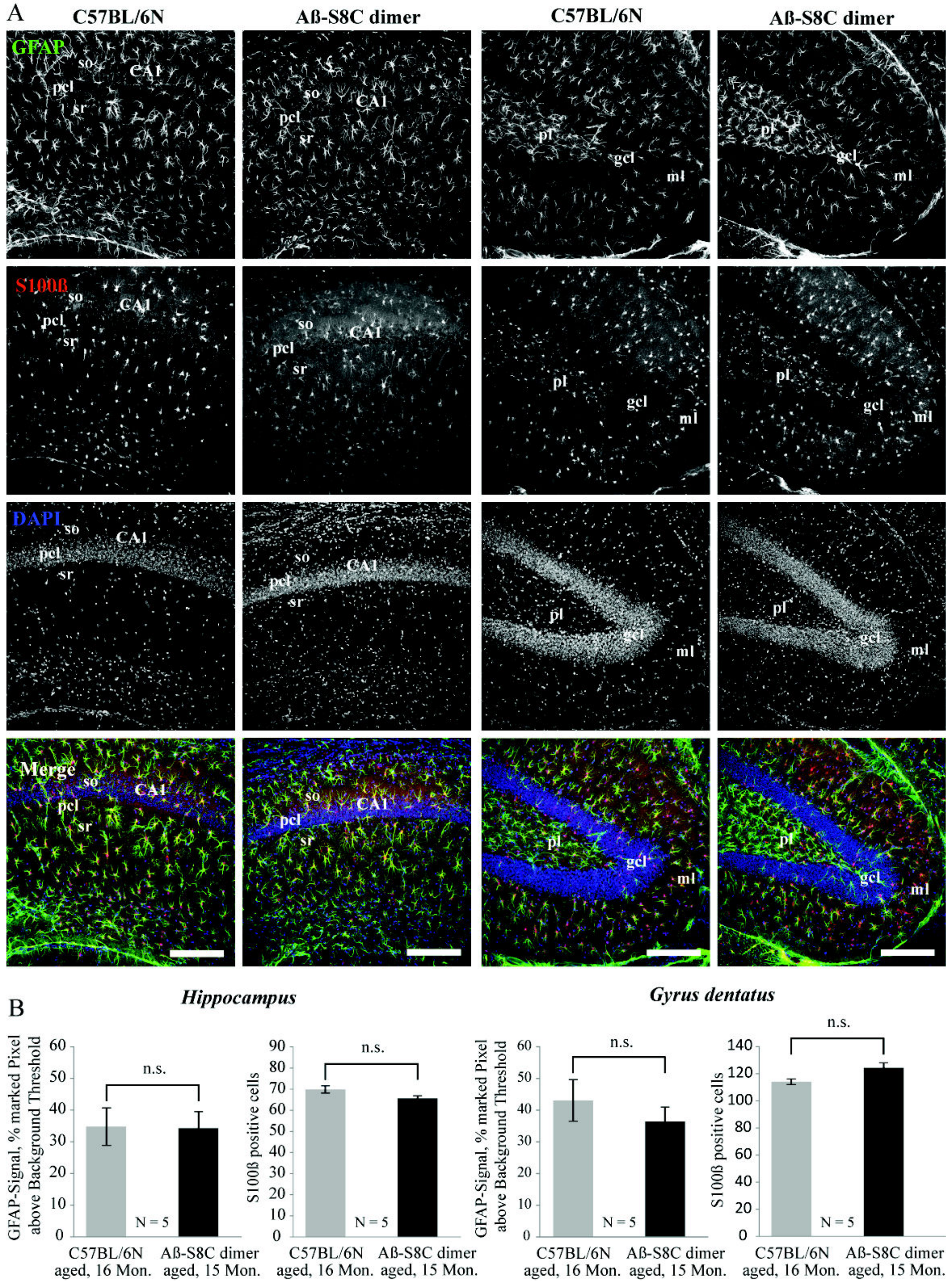

Figure 3.15: **GFAP and S100ß immunoreactivity pattern in the hippocampus formation of aged Aß-S8C dimer expressing mice compared to control animals. A)** GFAP and S100ß immunofluorescence and DAPI staining pattern in the hippocampus and the dentate gyrus of fixed tissue slices of Aß-S8C dimer expressing mice (aged, 15 months) compared to C57BL/6N control animals (aged, 16 months). Visual examination reveals no difference between transgenic and control animals. **B)** Measurement of the percentage of pixel above threshold and S100ß-positive cells in hippocampus and dentate gyrus of tgDimer and C57BL/6N control mice. Scale bars: 150 µm, N = 5 for tgDimer and C57BL/6N control mice; ± STD. [own image, Institute of Neurobiology, Düsseldorf]

pixel within the images and subtraction of pixels, whose gray values were below a defined threshold value. The threshold was determined by a line plot, positioned within the "dark" areas of every respective image made up by the GFAP negative somata of the pyramidal neurons in the *stratum pyramidale* of the CA1 region. The fraction of the pixels with a GFAP signal above threshold in the confocal images of the hippocampus and the dentate gyrus was used to evaluate the degree of GFAP expression in tissue slices of tgDimer- mice compared to C57BL/6N control animals. Furthermore, the number of S100ß-positive cells within the CA1 region and the dentate gyrus of the hippocampus formation was counted.

There was no significant difference in the percentage of pixels above threshold in confocal images of tgDimer mice compared to control animals. tgDimer mice exhibited 34.2 ± 5.3 % of pixel above threshold in the hippocampus and 36.4 ± 4.5 % in the dentate gyrus, compared to 34.8 ± 5.9 % positive signal in the hippocampus and 43.0 ± 6.6 % in the dentate gyrus of control animals. tgDimer mice had an average of 65.6 ± 1.2 S100ß-positive cells in the hippocampus and 124.4 ± 3.7 S100ß-positive cells in the dentate gyrus. Control mice exhibited an average of 69.8 ± 1.7 S100ß-positive cells in the hippocampus and 114.1 ± 2.1 in the dentate gyrus (N = 5 slices each; ± STD, Fig. 3.15 A, B). Taken together, these data show that Aß-S8C toxicity does not promote the activation of astrocytes and the development of astrogliosis in this transgenetic mouse model for the investigation of Alzheimer´s disease.

4 Discussion

This study intended to answer the question, how to investigate acute and chronic changes in astrocyte cell volume and morphology in vital and fixed tissue, and how astrocytes react to different pathological stimuli. A method that is based on the specific staining of the cells with SR101 for the investigation of volume changes of astrocytes in acute slices over minutes and hours has been developed. Anisotonic extracellular solutions were applied. The inhibition of NKCC1, describing the role of this cotransporter in volume regulation under anisotonic conditions and in the presence of NH_4^+, which is responsible for the development of brain edema following ALF, CLF and FHF were examined with this model system. Slice cultures of transgenic mice expressing GFAP-coupled GFP were used for the investigation of traumatic brain injury-induced astrogliosis, simulated through a scratch wound lesion as an example for chronic volume changes during days or weeks. The effect of a neuronal overexpression of a putative neurotoxic Aß-dimer on astrocytes in the hippocampus of aged transgenic mice was immunohistochemically examined for a possible role of this Aß-dimer in the chronic development of astrogliosis, which would be indicated by increased GFAP and S100ß expression patterns.

4.1 Staining procedures for astrocytes in acute hippocampal slices

For the understanding of how astrocytes are integrated into the cytoarchitecture of the hippocampal neuropil, it became necessary to label not only parts of their cytoskeleton as is can be done by using classical immunohistochemically antibody-labelling against GFAP, for example, but rather to find methods for the visualization of entire astrocytes and their complex spongiform morphology. Bushong et al. (2002) described a technique for the intracellular filling of astrocytes in fixed tissue with fluorescent dye by using sharp electrodes, and thereby was able to describe spatial relationships between these cells. For the study of morphological changes of astrocytes in acute hippocampal slices as a reaction to osmotic challenges or pharmacological stimulation, it was necessary to modify this experimental approach. The whole-cell patch–clamp technique was used here for the intracellular labeling of astrocytes in acute hippocampal slices. It has been shown, that astrocytes can successfully be patched, labeled and also visualized in their entirety, before and after the fixation of the tissue (Fig. 3.1 A,B) what allows for experimental approaches of cells in living tissue, as well as immunohistochemical studies afterwards. The use of gap junction-permeable labeling reagents, such as for the described avidin-neurobiotin method here, revealed the functional syncytium formed by the astrocytes and also showed the perivascular endfeet ensheathing capillaries. Additional immunohistochemical staining methods have also been applied to the slices (Fig. 3.1 A). Taken together, this method allows for the identification of cells after electrophysiological characterization, for example and the visualization of gap junction coupled cells (Stephan 2011). The combination of this technique with further immunohistochemical staining methods provides additional possibilities. As well, the combination of this labelling technique with confocal scanning microscopy allows for the visualization of high resolution images and 3D reconstruction, as described by Bushong et al. (2002). The detection of volume changes over a certain period of time demands, that astrocytes were kept alive before, during and after having underwent the staining procedure. However, the modification of the method for the recording of acute volume changes of astrocytes turned out to be very difficult, in that the loss off cells upon de-patching and the disruption of cells over time lead to the miscarriage of many experiments. For the detection of volume changes, it is necessary do withdraw the patch-pipette, because measurements of volume changes would be falsified by the supply of ions from the solution in the patch-pipette. During this withdrawal most of the cell-somata were lost. When the de-patching process was successful, a disruption off the cell lead, as described (Fig. 3.1 B), to a failure of the experiment, what lead to the decision that this technique should not be pursued further.

In contrast, the labeling of astrocytes with SR101 turned out to be an unproblematic staining method, which could easily be applied for monitoring volume changes of astrocytes in acute hippocampal slices. Confocal laser scanning microscopy was used for the real-time imaging of SR101-stained astrocytes in the *stratum radiatum* of the CA1 region in acute hippocampal slices. The very light-stable chromophore allows for the scanning of a cubic volume in the slice tissue up to thirteen times (Fig. 3.7). The SR101 staining marks all astrocytes so that multiple cells can be measured, but it is not possible to visualize one single cell entirely, as is shown by Bushong et al. (2002) for the intracellular dye filling, or by using whole-cell patch-clamp, as shown here. The obtained picture stacks were transferred to maximum intensity projection images, what compresses the image information of the scanned volume into a two-dimensional image. This approach circumvents extensive 3D-reconstruction and volume calculation and allows for the fast and uncomplicated measurement of multiple cells by using a threshold algorithm for the calculation of cross section soma area. In combination with an overlay method for visual verification, as well as occasional validation via manual encirclement it is secured, that the semi-automated measurements are correct. After having determined the appropriate parameters, this method approved useful for the analysis of astrocyte volume in the intact tissue. Several other studies over the past few years used similar techniques: Hirrlinger et al. (2008) used transgenic mice, whose astrocytes were labelled by expressing enhanced GFP (EGFP) under the GFAP promoter control together with a two-photon laser scanning microscope. The z-stacks obtained by this method were also transferred into MIPs and soma area was measured by counting the number of pixel above a distinct threshold.

Florence et al. (2013) used SR101 labelled, acute hippocampal slices of rats for volume measurement. Like Hirrlinger et al. (2008), they used two-photon microscopy and they also transferred obtained stacks into MIPs, which were thresholded, obtained areas calculated and presented as percent changes.

The study of Risher et al. (2009) then served as basis for the development of the measurement method presented here. They used two-photon laser scanning microscopy for image acquisition and also used transgenic mice with EGFP-GFP expressing astrocytes. Soma areas were measured by employing three different techniques: somata were traced by hand, MIP images were pseudocolored in green and red and then overlaid, and “control profiles were traced and filled to create a mask, which revealed peripheral areas of swelling when overlaid upon experimental images.” (Risher et al. 2009).

The method presented here is a symbiosis of these approaches, which uses confocal laser scanning microscopy instead of two-photon laser scanning microscopy to avoid its poor axial resolution (~ 2µm, Florencet al. 2013). SR101 labelling for staining of astrocytes was chosen, because of its reliability and uncomplicated handling (Kafitz et al. 2008), besides its economic efficiency, compared to the usage of transgenic animals. Although the analysis of MIPs for the measurement of relative volume changes underestimate actual volume changes, this approach is considered to adequate therefore (Hirrlinger et al. 2008, Risher et al. 2009, Florence et al. 2012), because it allows the direct measurement, instead of indirect methods. Examples therefore are the measurement of increases in extracellular resistance (Traynelis & Dingledine 1989), field potential amplitude (Rosen & Andrew 1990) and tissue light transmittance (Andrew & MacVicar 1994), which were also mentioned by Risher et al. (2009).

The combination of a semi-automated, threshold algorithm based image analysis method, together with visual comparison of overlay images and occasional validation via manual encirclement was chosen to secure correct measurements.

However, due to the fact that SR101 labels all astrocytes within the tissue slice, measurements of changes of cross section soma area in this study refer to the cell body and major processes that can be allocated to one accurately defined cell. Nonetheless, developing and using this technique, high resolution images of astrocytes and reliable measurements of respective cross section soma areas were obtained. Experimental protocols were developed for short-time experiments over an hour, to monitor volume under control conditions and upon application of hypo- or hyperosmolar extracellular solutions. These procedures where adopted to long-time experiments with a duration of six hours. Pharmacological experiments allowed the examination of molecular components that are putatively involved in the control of the volume of astrocytes in acute hippocampal slices.

4.2 Volume regulation in short time experiments

The cross-sectional soma area of astrocyte did not change significantly over 60 min under control conditions in regular ACSF, although alternating de- and increases in between +3.9% and -4.0% as referred to the soma area at the beginning of the experiment were detected, what leads to the assumption, that a constant cell volume under isotonic conditions is a result of cell swelling tendencies and cell shrinking tendencies, indicating a dynamic volume regulation around the volume set point (Russel 2000).

There are several other recent studies, in which similar experimental techniques were used to determine astrocyte volume changes (Hirrlinger et al. 2008, Risher et al. 2009, Florence et al. 2012), but only Hirrlinger et al. (2008) and Florence et al. (2012) studied real time volume regulation under control conditions. Hirrlinger et al. (2008) reported a decrease of soma area of about 6% over 32 min and Florence et al. (2012) a decrease by ~1% over 40 min: both groups did not detect alternating de- and increases of the soma area. Such a dynamic volume regulation could be the result of the regulation of changes in $[K^+]_o$ due to neuronal activity, where astocytes are thought to play a key role in via K^+ spatial buffering (Kofuji & Newman 2009, Florence et al. 2012).

Reduction of extracellular osmolarity by -90 mOsm resulted in significant increase in soma area followed by a decrease after 20 min, indicating the activation of a RVD mechanism, and a significant increase afterwards (Fig. 3.5 B, Fig. 3.6). This is in contrast to results obtained by Risher et al. (2009), who also found a volume increase after reducing the extracellular osmolarity by –40 mOsm, but did not observe RVD, probably due to the much shorter observation time (one scan after 15 min exposure). An increase in cell volume after application of hypoosmolare ACSF with an osmolarity of ~206 mOsm was also reported by Hirrlinger et al. (2008), which turned to a slight, but insignificant decrease after 40 min.

In contrast, cells in our study swelled again at later time points what might indicate, that the presented hypoosmotic challenge might have been too massive for the volume regulatory capacity of astrocytes to counteract over longer periods of time.

Return to normosmotic condition resulted in a slight undershoot that might be due to a volume-regulatory loss of osmolytes (Strange 1992). Increasing the extracellular osmolarity by +140 mOsm resulted in an expected decrease in the soma area of the astrocytes. This decrease remained irreversible, even after return to normosmotic conditions, indicating a damaging of the cells.

In summary, the results suggest that the SR101-stained acute hippocampal slice model system is appropriate for the monitoring of volume changes in astrocytes, because cells in isotonic ASCF maintained a constant cell volume over 60 min, and we were able to measure volume changes due to changes of the extracellular osmolarity, together with a return to base line values after transition to isotonic conditions, at least when hypoosmolar ACSF was applied before.

4.3 Volume regulation in long term experiments

This work is, to our knowledge, the first to investigate volume regulation of astrocytes in hippocampal slices over an extended time range. Other studies on volume regulation of astrocytes extended over periods of maximally 60 min (Hirrlinger et al. 2008, Risher et al. 2009, Florence et al. 2012).

Here, we examined a range of 360 min. With an experimental duration of more than six hours, this procedure approximated the maximum extent of time for the use of acute hippocampal slices. It could have been shown that the tissue injury by the vibratome leads to changes in cellular metabolism and receptor activation, as well as in the expression and location of astrocyte specific proteins, amongst others (Takano et al. 2014), so that acute slices cannot be kept viable for more than several hours.

Being almost similar to the results obtained in short term experiments, which gave first hints for volume regulation of astrocytes, measurements over a prolonged time period revealed that the soma area decreases over time (Fig. 3.7 B, Fig. 3.8). This decrease was overlaid by a de- and increase of soma area with periods up to 120 min, which implies that cell volume is regulated dynamically, in that alternate volume increase and decrease mechanisms occur (Russel 2000) that might be according to activity-based changes in ion concentration and osmolarity (Kofuji & Newman 2009, Florence et al. 2012). The fact that cell volume in general decreases over time might be explained by the fact that the experiments were carried out *ex vivo*. It is noted that water and ion homeostasis in the CNS are tightly controlled via the glymphatic system, "a paravascular fluid exchange pathway that enables brain interstitial and cerebrospinal fluid turnover and is facilitated by glial cells" (Thrane et al. 2014) which consists of four separated fluid compartments: the intracellular fluid (ICF); the interstitial fluid (ISF); the cerebrospinal fluid (CSF); and vascular compartments. This system regulates the exchange of cerebrospinal (CSF) and interstitial fluids (ISF), and also influences intracellular fluid homeostasis (Thrane et al. 2014) and the drainage of excess water via the vascular compartment. Regarding the experimental conditions, two components of this "brain-wide paravasculare pathway for cerebrospinal and interstitial fluid exchange", namely the paravascular CSF-ISF exchange, were missing (Thrane et al. 2014, Hirrlinger et al. 2008), a fact that might explain the observed impairment of astrocyte volume maintenance.

Hirrlinger et al. (2008) also reported a significant reduction in astrocyte soma area under control conditions, which was ascribed to photobleaching of EGFP after 32 min. Photobleaching of SR101 might be an explanation for the volume decrease observed here, however to a minor degree, since an adequate bleaching correction procedure has successfully been performed.

Acute hippocampal slices are suitable to examine morphology and physiology over a certain period of time, it is undeniable that the vitality of the cells decline the longer the time *ex vivo* becomes. Ion composition and energy supply, mediated by superfusion with ACSF can only simulate several important necessities essential for a proper physiological functioning. The isotonic ACSF used here had an osmolarity of ~316 mOsm. Hirrlinger et al. (2008) used an ACSF with an osmolarity of ~322 mOsm and reported a decrease in soma area of about 6% during 32 min. Risher et al. (2009) worked with an ACSF of 291-293 mOsm, did not perform time lapse imaging, but measured soma area once under control conditions, once after having decreased and increased the extracellular osmolarity and again under control conditions. Florence et al. (2012) used an ACSF with 295-300 mOsm for experiments with acute brain slices of Sprague Dawley rats, instead of mice, which were used by Hirrlinger et al. (2008), Risher et al. (2009) and in the present study. Florence et al. (2012) measured a soma area decrease of ~ 1% over 40 min. So, Hirrlinger et al. (2008), Risher et al. (2009) and Florence et al. (2012) inspected volume regulation for a shorter time range, compared to the present study.

ACSF recipes try to approach physiological conditions. These conditions, to be more precise ion homeostasis and water balance between intra- and extracellular space need to be strictly regulated, differences in the osmolarity of the applied isotonic ACSF, although appearing quite small, may lead to the described cell shrinkage as far as volume regulation over longer periods of time is concerned.

Other factors, for example hormonal regulation by vasopressin (AVP), atriopeptin (ANP), angiotensinogen (AGT) and angiotensin (Ang) II, also important for water and ion homeostasis in astrocytes, are missing(Simard & Nedergaard 2004). The lack of such centrally released factors that are supposed to regulate cell volume "possibly via intrinsic osmoregulation of glial cells" (Simard & Nedergaard 2004) might impair the ability of astrocytes to maintain a constant cell volume over time in acute slices.

The unphysiological room temperature at which the experiments were done may contribute to the observed decrease in cell volume. This could be explained by the fact that cation-chloride-cotransporters (CCCs) exhibit a temperature dependence (Hartmann & Nothwang, 2011) and it has been shown that the transport activity of NKCC1 is increased at 37°C compared to RT (Hannemann & Flatman 2011). Also, it has been shown here, that the inhibition of NKCC1 by bumetanide administration resulted in a significant reduction of the soma area under isotonic conditions (Fig. 3.9 A). So a decreased NKCC1 transport activity at RT might also contribute to the impaired volume maintenance of astrocytes in acute slices. The experiments carried out by Risher et al. (2009) took place at 32-34°C. Furthermore, Chvátal et al. (2007) reported that a reduction in extracellular osmolarity of -100 mOsm at room temperature resulted only in a small RVD. Hirrlinger et al. (2008) also reported a decrease of soma area under isotonic conditions after 32 min at RT. Although they assume, that this decrease is due to photobleaching, they argue that volume regulation processes like RVD might be temperature-dependent, since RVD was found in cell cultures at 37°C, and that experiments carried out at RT might not provide optimal conditions for a proper function of these regulation processes. However, elevating the temperature to 37°C would result in a massive decrease in the vitality of the slices and cells, thus drastically reducing the experimental time and making six hours experiments with acute hippocampal slices impossible. This problem could possibly be avoided by performing such experiments with hippocampal slice cultures at 37°.

It was postulated that cells under hypotonic extracellular conditions react with an anisotonic volume change that is a rapid water flow into the cell (Strange 1992). In contrast to previous studies in cortical slices (Andrew & MacVicar 1994, Andrew et al. 1997, 2007) a reduction of soma area, i.e. an RVD, was detected here, however not before ~50-60 min after exposition to hypoosmolar ACSF. Risher et al. (2009) measured soma area during 15-20 min of osmotic challenge with no sign of RVD. The subsequent rise in soma area indicates, that the cells were not able to maintain the RVD, suggesting that the osmotic challenge was too massive to withstand for a prolonged time period. After reaching the peak of volume increase after 120 min (Fig. 3.7 B, Fig. 3.8), soma area stayed elevated. That this elevation was not significant with respect to the baseline value might reflect the volume decline over time observed under control conditions.

The exposure to hyperosmolar ACSF resulted in the expected volume decrease, with only a slight tendency for a postulated RVI (Strange 1992). The finding that cell volume stayed significantly decreased in short-term and in long-term experiments indicates that astrocytes cannot compensate a drop in extracellular osmolarity by 30% or more. The lack of the many other factors responsible for volume regulation in the intact brain might contribute for this inability.

4.4 Bumetanide inhibits anisotonic volume decrease

Ion and water transport in the brain need to be tightly regulated, due to the placement of this part of the CNS within an osseous skull (Passantes-Morales 1996). The cellular mechanisms underlying the sensing of cell volume and the activation of its regulation in the brain are not yet fully understood. The activity of ion transporters and ion channels serves not only for the homeostasis of inorganic solutes but also for the maintenance of the cell volume and is upregulated within seconds upon osmotic perturbations that trigger sensors of the volume set point. (McManus et al. 1995, Kahle et al. 2009). The significant decrease in soma area in isotonic ACSF upon bumetanide administration indicates a participation of NKCC1 in the volume regulation in astrocytes under isotonic conditions, and not only in RVI. NKCC1 is found in various types of tissue, especially in epithelial cells, where it is involved in ion homeostasis. In the CNS NKCC1 is expressed in neurons and glial cells, where it is assumed to be involved in volume regulation and ion homeostasis. Thus NKCC1 has been shown to contribute to several pathogenic states, for example ischemic damage of neurons and development of brain edema caused by astrocyte swelling and glutamate release (Chen & Sun 2005).

The complete inhibition of osmotically induced volume changes by bumetanide leads to the conclusion that in contrast to previous assumptions by Risher et al. (2009), cell swelling is not a passive, but rather an active process, in which bumetanide-sensitive cotransport through the NKCC1 plays a crucial role. This contradicts the model that water is in thermodynamic equilibrium across the plasma membrane under and freely permeable through the cell membrane when a transmembrane osmotic gradient causes a passive water flux. According to this view, astrocytes should not be able to resist an osmotic challenge, as they are, when NKCC1 is inhibited. It is also assumed that animal cells are not able to counterbalance transmembrane osmotic gradients by correspondingly generating hydrostatic pressure (McManus 1995, Kahle et al. 2009) and therefore change their volume. Regarding epithelial barriers, it is known that cells are able to avert the passage of certain molecules like water, protons and ammonia across their membranes (Zeidel 1996) and that the transport of such molecules through this membranes might not be a passive, but rather an active and regulated process.

In the case of water and NH_4^+, it has been shown that membranes with high amounts of fully saturated hydrocarbon chains like sphingomyelin and certain amounts of cholesterol sulfate show a reduced permeability for these substances (Zeidel 1996). H_2O and NH_4^+ are important molecules, as far as astrocyte duties regarding homeostasis are concerned. According to the results obtained here, volume regulation in the brain is a tightly regulated process, in which NKCC1 contributes permanently to the maintenance of cell volume, not only under isotonic conditions but also upon osmotic perturbations by upregulation of its activity. Thus NKCC1 inhibition resulted in a significant volume decrease under control conditions, as well as in a lack of cell swelling under hypotonic conditions. This fits in with several corollaries, which Russel (2000) postulates, when talking about the role of NKCC in the homeostatic cell volume regulation: "…3) Inhibition of the NKCC fluxes under normally isosmotic conditions would lead to cell shrinkage (assuming normal cell volume is the dynamic result of cell shrinkage tendencies and cell swelling tendencies) 4) Stimulation of NKCC fluxes ought to cause cell swelling. 5) Cell swelling might be expected to reduce NKCC fluxes…" (Russel 2000). Here, Inhibition of NKCC1 results in a decrease in cell volume under isotonic conditions, but it is not clear, if hypotonicity induced cell swelling is caused by stimulation of NKCC fluxes or vice versa. And finally our results show, that reduction of NKCC fluxes (inhibited by bumetanide) prevent hypotonicity induced cell swelling.

Andrew et al. (2007) proposes that pyramidal neurons are "osmoresistant", i.e. they maintain their volume upon osmotic challenge in order to sustain their electrophysiological stability. Astrocytes are able to alter their volume in reaction to osmotic challenge, because of the expression of water-permeable aquaporins (Nielsen et al. 1997, Amiry-Moghaddam & Ottersen

2003, Risher et al. 2009). But when NKCC1 is inhibited, astrocytes also seem to be "water-tight", because hypotonic conditions then do not lead to cell swelling. Volume changes thus seem to be activated by some sort of osmosensor, comparing the osmolarity of extracellular and intracellular compartments, triggering the activation of NKCC1 and somehow propagating water influx, gated via aquaporins for example.

4.5 Ammonium hampers volume decrease in acute slices

NH_4^+ has been shown to induce the swelling of astrocytes, thus leading to severe brain edema, the most prominent complication in the late phase of HE caused by ALF (Norenberg 1987, Traber et al. 1987, Swain et al. 1991). Several studies showed that high NH_4^+ levels lead to this pathological increase in cell volume *in vivo* and *in vitro* (Ganz et al. 1989, Takahashi et al. 1991, Blei et al. 1994, Norenberg et al. 2009). Jayakumar et al. (2008) showed that cultured astrocytes react upon NH_4^+ treatment with an activation of NKCC1 and subsequent cell swelling, which could be reduced significantly by bumetanide. That study also found an increase in total NKCC1 protein expression as well as an enhanced oxidation and nitration of NKCC1, and that the treatment with antioxidants and cyclohexamide (CHX) significantly decreased the NH_4^+-induced NKCC1 activity (Jayakumar et al. 2008). Since oxidative and/or nitrosative stress activates the transcription factor NF-κB, Jayakumar and Norenberg (2010) showed an increased NF-κB activation (nuclear translocation) upon NH_4^+ treatment, which could be prevented by treatment with antioxidants and NOS inhibitors as well as by direct inhibitors of NF-κB or specific siRNA, and these treatments also reduced NKCC1 activation and astrocyte swelling caused by NH_4^+ (Sinke et al. 2008, Jayakumar & Norenberg 2010). Furthermore, Jayakumar et al. (2006) described an NH_4^+-induced activation of MAPK and CaMKII in astrocytes, and inhibition of these kinases has been shown to decrease NH_4^+-induced NKCC1 phosphorylation and subsequent cell swelling (Jayakumar et al. 2006). Since MAPKs and hence NF-κB may be activated by oxidative and/or nitrosative stress, it could be possible that NH_4^+ causes an increase in NKCC1 activity and expression (Jayakumar et al. 2006, Sinke et al. 2008, Jayakumar & Norenberg 2010). It has also been shown that cultured astrocytes treated with NH_4^+ exhibit an elevation in bumetanide-sensitive NKCC1 activity after 18 to 24 hours of exposure and an elevated, but not significant, increase in NKCC1 activity between one and six hours. In addition, exposure of astrocyte cultures to NH_4^+ resulted in an increase in cell volume (Jayakumar et al. 2008).

Kelly et al. (2009) then showed that 5 mM NH_4^+ caused significant changes in pH_i and $[Na^+]_i$ during up to 50 min of treatment in 20-34 DIV cultured astrocytes. NH_4^+ caused an acidification of about 0.2 pH units and an elevation of $[Na^+]_i$ of about 20 mM from an initial steady-state of 19 mM up to 40 mM. Other studies suggested that the acidification is partly caused by NKCC1-mediated NH_4^+ inward transport (Nagaraja & Brookes 1998, Titz et al. 2006) and the steady-state $[Na^+]_i$ is also maintained via NKCC1 activity (Rose & Ransom 1996a, Su et al. 2002b). Kelly et al. (2009) showed that the changes in pH_i and $[Na^+]_i$ could be inhibited by bumetanide. These findings were confirmed by Kelly & Rose (2010) for hippocampal slices, where NH_4^+ also resulted in a significant acidification of 0.18 pH units and a $[Na^+]_i$ increase of about 27 mM after ~30 min. Both pH and $[Na^+]_i$ returned to baseline after NH_4^+ removal. As in culture, bumetanide completely inhibited increases in steady-state $[Na^+]_i$ and almost halves the amplitude of the NH_4^+-induced acidification (Kelly & Rose 2010).

Here it is shown that treatment of acute hippocampal slices with 5 mM NH_4Cl resulted in a measurable increase in cell volume. After 300 to 330 min this increase became significant, which indicates that NH_4^+ disturbs volume regulation with a time course that may reflect the development of HE brain edema in an early state. The NH_4^+-induced swelling of the astrocytes was significantly reduced by bumetanide after 90 min.

4.6 Induction of reactive gliosis in hippocampal slice cultures

The organotypic hippocampal slice culture has proven to be a reliable model system for the examination of the function of neurons and glial cells in matters of cellular and tissue specific characteristics, of developmental processes within neuronal networks (Stoppini et al. 1991, Gähwiler et al. 1997, Förster et al. 2006) and of the effect of excitotoxicity (Kunkler 1997, Holopainen 2005). Providing all advantages of cell cultures, like easy handling and the control of experimental conditions, organotypic cultures preserve the natural cytoarchitecture of the tissue. In particular, it has been shown that astrocyte morphology and synaptical arrangements are preserved in organotypic slice cultures (Benediktsson et al. 2005, Haber 2006, Nishida 2007, Lushnikova 2009).

When using animals that expressed fluorescent markers, like GFAP/GFP in this case, organotypic cultures enable the documentation of astroglial morphology without any staining procedures. It was found that SR101 staining almost entirely matches with the GFP expression pattern (Schreiner et al. 2013), confirming that SR101 vital staining is a reliable tool for the identification of astrocytes both in acute and cultured tissue slices (Nimmerjahn et al. 2004, Kafitz et al. 2008) as well as *in vivo* (Nimmerjahn & Helmchen 2012). Another interesting finding was that astrocytes in organotypic tissue culture exhibit an up to four times enlarged soma area, compared to soma areas measured in acute tissue slices (Fig. 3.8 C, Fig. 3.14 E). An explanation for this enlargement might be the flattening of the culture (Schreiner et al. 2013), which leads to a less dense tissue structure in contrast to the more compact cytoarchitecture that can be found in freshly isolated acute slices.

Lesioning the CA1 hippocampal region in organotypic slices nonetheless leads to the development of a glial scar in proximity to the scratch wound, as indicated by the elevated content of GFAP and S100ß and the presence of hypertrophic astrocyte somata. More distant (100-350 µm) to the lesion site, the degree of astrocytic reactivity decreased continuously to moderate or mild, with minor swelling of cell somata and GFAP expression. In addition the ability of astrocytes for the uptake of SR101 was significantly reduced in closer proximity to the glial scar, developed after traumatic brain injury (TBI). Taken together, the findings that features of reactive gliosis as found following injuries of brain tissue (Pekny & Nilsson 2005, Sofroniew 2009, Buffo et al. 2010) can be reproduced in organotypic cultures, and that the degree of astrocytes activation is defined by their distance the severity of the injury (Ridet et al. 1997, Pekny & Nilsson 2005).

4.7 Aß-S8C dimer expression does not alter GFAP staining pattern

Amyloid-ß (Aß) peptide plaques present a hallmark in the pathology of Alzheimer´s disease (AD). Being generated by ß- and γ-secretase proteolysis, the presence of Aß has been associated with neurotoxicity, causing synaptic degradation and the loss of dendritic spines leading to morphological abnormalities in the early phase of AD (Haass & Selkoe 1993, 2007, Takami, et al. 2009, Müller-Schiffmann et al. 2011). Recently a mouse model, named tgDimer, expressing high amounts of soluble Aß-Dimers, has been generated (Müller-Schiffmann et al. 2014). It is known that extracellular deposits of Aß proteins initiate reactive astrocytosis in *vitro* (DeWitt et al. 1998), and these activated astrocytes were identified in participating in neuro-inflammatory processes (Heneka et al. 2010). The question arose if astrocytes in the hippocampal formation of aged mice over-expressing Aß-S8C dimers exhibit cellular hypertrophy, recognizable by increased expression of GFAP and S100ß, which, as discussed in the previous chapter, present hallmarks of astrogliosis (Beach et al. 1988, Griffin et al. 1989, Nagele et al. 2004, Kashon et al 2004, Verkhratsky et al. 2010).

In this study, neither evidence for an upregulation of GFAP content or an increase in the number of S100ß-stained astrocytes, nor any changes of astroglial morphology or signs of hypertrophy have been detected. These results are in line with the findings that overexpression of the Aß dimer does not lead to neuroinflammation in the hippocampus (Müller-Schiffmann et al. 2014).

Taken together these results show that the method established here generally is suitable for the determination of acute, as well as chronic cellular volume changes in brain slices of murine brains. Furthermore these results indicate that the transporter NKCC1 is significantly involved in acute volume changes in astrocytes. For further experimental approaches for the examination of the role of NKCC1 in volume regulation, as well as the influence of NH_4^+ on volume regulation in astrocytes and the early phase of an NH_4^+-induced cell swelling, it can be taken into consideration to use OHSCs, obtained from GFAP/GFP expressing mice, or in combination with SR101-staining. So, the time frame, where experiments with acute brain slices reach their limits could be supplemented and continued, from several ours up to days or weeks to complete the observation period and to elucidate further knowledge about the cellular mechanisms involved here.

The immunohistochemical staining method used here for the examination of Aß-S8C induced astroglial hypertrophy does not directly show chronic volume changes. Nonetheless it provides a reliable tool to study the hallmarks of astrogliosis and the use of this classical technique should always be taken into consideration.

A References

Abbruscato TJ, Lopez SP, Roder K, Paulson JR (2004): Regulation of blood-brain barrier Na,K,2Cl-cotransporter through phosphorylation during in vitro stroke conditions and nicotine exposure. J Pharmacol Exp Ther 310:459-68.

Abramov AY, Canevari L, Duchen MR (2003): Changes in intracellular calcium and glutathione in astrocytes as the primary mechanism of amyloid neurotoxicity. J Neurosci 23:5088-95.

Abramov AY, Canevari L, Duchen MR (2004): Beta-amyloid peptides induce mitochondrial dysfunction and oxidative stress in astrocytes and death of neurons through activation of NADPH oxidase. J Neurosci 24:565-75.

Akimova OA, Grygorczyk A, Bundey RA, Bourcier N, Gekle M, Insel PA, Orlov SN (2006): Transient activation and delayed inhibition of Na^+-K^+-Cl^- cotransport in ATP-treated C11-MDCK cells involve distinct P2Y receptor subtypes and signaling mechanisms. J Biol Chem 281:31317-25.

Alger BE, Nicoll RA (1983): Ammonia does not selectively block IPSPs in rat hippocampal pyramidal cells. J Neurophysiol 49:1381-91.

Allert N, Köller H, Siebler M (1998): Ammonia-induced depolarization of cultured rat cortical astrocytes. Brain Res 782:261-70.

Alvarez-Leefmans FJ, Herrera-Pérez JJ, Márquez MS, Blanco VM (2006): Simultaneous measurement of water volume and pH in single cells using BCECF and fluorescence imaging microscopy. Biophys J 90:608-18.

Alzheimer A (1910): Beiträge zur Kenntnis der pathologischen Neurogliaund ihrer Beziehungen zu den Abbauvorgängen im Nervengewebe. In: Nissl F, Alzheimer A, eds. Histologische und histopathologische Arbeiten über die Grosshirnrinde mit besonderer Berücksichtigung der pathologischen Anatomie der Geisteskrankheiten Jena. Verlag von Gustav Fischer, p401–562.

Andersen P, Bliss TV, Skrede KK (1971): Lamellar organization of hippocampal pathways, Exp Brain Res 13:222-38.

Andersen GØ, Skomedal T, Enger M, Fidjeland A, Brattelid T, Levy FO, Osnes JB (2006): Alpha1-AR-mediated activation of NKCC in rat cardiomyocytes involves ERK-dependent phosphorylation of the cotransporter. Am J Physiol Heart Circ Physiol 286:H1354-60.

Andrew RD, Lobinowich ME, Osehobo EP (1997): Evidence against volume regulation by cortical brain cells during acute osmotic stress. Exp Neurol 143:300-12.

Andrew RD, Labron MW, Boehnke SE, Carnduff L, Kirov SA. (2007): Physiological evidence that pyramidal neurons lack functional water channels. Cereb Cortex 17:787-802.

Andrew RD, MacVicar BA (1994): Imaging cell volume changes and neuronal excitation in the hippocampal slice. Neuroscience 62:371-83.

Aamaral DG (1993): Emerging principles of intrinsic hippocampal organization. Curr Opin Neurobiol 3:225-9.

Amaral DG, Witter MP (1989): The three-dimensional organization of the hippocampal formation: a review of anatomical data. Neurosciences 31:571-91.

Amiry-Moghaddam M, Ottersen OP (2003): The molecular basis of water transport in the brain. Nat Rev Neurosci 4:991-1001.

Amiry-Moghaddam M, Otsuka T, Hurn PD, Traystman RJ, Haug FM, Froehner SC, Adams ME, Neely JD, Agre P, Ottersen OP, Bhardwaj A (2003): An alpha-syntrophin-dependent pool of AQP4 in astroglial end-feet confers bidirectional water flow between blood and brain. Proc Natl Acad Sci USA 100:2106-11.

Apelt J, Ach K, Schliebs R (2003): Aging-related down-regulation of neprilysin, a putative beta-amyloid-degrading enzyme, in transgenic Tg2576 Alzheimer-like mouse brain is accompanied by an astroglial upregulation in the vicinity of beta-amyloid plaques. Neurosci Lett 339:183-6.

Bak LK, Schousboe A, Waagepetersen HS (2006): The glutamate/GABA-glutamine cycle: aspects of transport, neurotransmitter homeostasis and ammonia transfer. J Neurochem. 98:641-53.

Beach TG, McGeer EG (1988): Lamina-specific arrangement of astrocytic gliosis and senile plaques in Alzheimer's disease visual cortex. Brain Res. 463:357-61.

Bear MF (1996): A synaptic basis for memory storage in the cerebral cortex. Proc Natl Acad Sci USA 93:13453-9.

Bekar LK, He W, Nedergaard M (2008): Locus coeruleus alpha-adrenergic-mediated activation of cortical astrocytes in vivo. Cereb Cortex 18:2789-95.

Ben-Ari Y, Gaiarsa JL, Tyzio R, Khazipov R (2007): GABA: a pioneer transmitter that excites immature neurons and generates primitive oscillations. Physiol Rev 87:1215-84. Review.

Benediktsson A M, Schachtele SJ, Green SH, Dailey ME (2005): Ballistic labeling and dynamic imaging of astrocytes in organotypic hippocampal slice cultures. J Neurosci, Methods, 141:41–53.

Benjamin AM, Okamoto K, Quastel JH (1978): Effects of ammonium ions on spontaneous action potentials and on contents of sodium, potassium, ammonium and chloride ions in brain in vitro. J Neurochem 30:131-43.

Bergeron MJ, Gagnon E, Wallendorff B, Lapointe JY, Isenring P (2003): Ammonium transport and pH regulation by K(+)-Cl(-) cotransporters. Am J Physiol Renal Physiol 285:68-78.

Blei AT, Olafsson S, Therrien G, Butterworth RF (1994): Ammonia-induced brain edema and intracranial hypertension in rats after portacaval anastomosis. Hepatology 19:1437-44.

Brambilla R, Bracchi-Ricard V, Hu WH, Frydel B, Bramwell A, Karmally S, Green EJ, Bethea JR (2005): Inhibition of astroglial nuclear factor kappaB reduces inflammation and improves functional recovery after spinal cord injury. J Exp Med. 202:145-56.

Brookes N (1992): Intracellular pH as a regulatory signal in astrocyte metabolism. Glia 21:64-73.

Buffo A, Rolando C, Ceruti S (2010): Astrocytes in the damaged brain: molecular and cellular insights into their reactive response and healing potential. Biochem Pharmacol 79:77-89.

Bushong EA, Martone ME, Jones YZ, Ellisman MH (2002): Protoplasmic astrocytes in CA1 stratum radiatum occupy separate anatomical domains. J Neurosci 22:183-92.

Bushong EA, Martone ME, Ellisman MH (2004): Maturation of astrocyte morphology and the establishment of astrocyte domains during postnatal hippocampal development. Int J Dev Neurosci 22:73-86.

Chen H, Sun D (2005): The role of Na-K-Cl co-transporter in cerebral ischemia. Neurol Res. 27:280-6. Review

Chen Y, Vartiainen NE, Ying W, Chan PH, Koistinaho J, Swanson RA (2001): Astrocytes protect neurons from nitric oxide toxicity by a glutathione-dependent mechanism. J Neurochem 77:1601-10.

Christopherson KS, Ullian EM, Stokes CC, Mullowney CE, Hell JW, Agah A, Lawler J, Mosher DF, Bornstein P, Barres BA (2005): Thrombospondins are astrocyte-secreted proteins that promote CNS synaptogenesis. Cell 120:421-33.

Chvátal A, Andrová M, Kirchhoff (2007): Three-dimensional confocal morphometry-A new approach for studying dynamic changes in cell morphology in brain slices. J Anat 210:671-683.

Clemmesen JO, Larsen FS, Kondrup J, Hansen BA, Ott P (1999): Cerebral herniation in patients with acute liver failure is correlated with arterial ammonia concentration. Hepatology 29:648-53.

Cooper AJ, McDonald JM, Gelbard AS, Gledhill RF, Duffy TE (1979): The metabolic fate of 13N-labeled ammonia in rat brain. J Biol Chem 254:4982-92.

Correa-Cerro LS, Mandell JW (2007): Molecular mechanisms of astrogliosis: new approaches with mouse genetics. J Neuropathol Exp Neurol 66:169-76.

Deitmer JW, Rose CR (1996): pH regulation and proton signalling by glial cells. Prog Neurobiol 48:73-103.

Deitmer JW, Rose CR (2010): Ion changes and signalling in perisynaptic glia. Brain Res Rev 63:113-29.

Diecke FP, Wen Q, Iserovich P, Li J, Kuang K, Fischbarg J (2005): Regulation of Na-K-2Cl cotransport in cultured bovine corneal endothelial cells. Exp Eye Res 80:777-85.

Dierkes PW, Wüsten HJ, Klees G, Müller A, Hochstrate P (2006): Ionic mechanism of ouabain-induced swelling of leech Retzius neurons. Pflugers Arch 452:25-35.

Dietzel I, Heinemann U, Hofmeier G, Lux HD (1980): Transient changes in the size of the extracellular space in the sensorimotor cortex of cats in relation to stimulus-induced changes in potassium concentration. Exp Brain Res 40:432-9.

Dietzel I, Heinemann U, Lux HD (1989): Relations between slow extracellular potential changes, glial potassium buffering, and electrolyte and cellular volume changes during neuronal hyperactivity in cat brain. Glia 2:25-44.

Di Ciano-Oliveira C, Sirokmány G, Szászi K, Arthur WT, Masszi A, Peterson M, Rotstein OD, Kapus A (2003): Hyperosmotic stress activates Rho: differential involvement in Rho kinase-dependent MLC phosphorylation and NKCC activation. Am J Physiol Cell Physiol 285:555-66.

Di Giorgio FP, Carrasco MA, Siao MC, Maniatis T, Eggan K (2007): Non-cell autonomous effect of glia on motor neurons in an embryonic stem cell-based ALS model. Nat Neurosci 10:608-14.

Eddleston M, Mucke L (1993): Molecular profile of reactive astrocytes--implications for their role in neurologic disease. Neuroscience 54:15-36. Review.

Felipo V, Butterworth RF (2002): Neurobiology of ammonia. Prog Neurobiol 67:259-79. Review.

Flatman PW (2008): Cotransporters, WNKs and hypertension: an update. Curr Opin Nephrol Hypertens 17:186-92. Review.

Florence CM, Baillie LD, Mulligan SJ (2012): Dynamic volume changes in astrocytes are an intrinsic phenomenon mediated by bicarbonate ion flux. PLoS One 7:e51124.

Förster E, Zhao S, Frotscher M (2006): Lamminating the hippocampus. Nat Rev Neurosci 7:259-267.

Gagnon KB, England R, Delpire E (2006): Characterization of SPAK and OSR1, regulatory kinases of the Na-K-2Cl cotransporter. Mol Cell Biol 26:689-98.

Gagnon KB, England R, Delpire E (2006): Volume sensitivity of cation-Cl^- cotransporters is modulated by the interaction of two kinases: Ste20-related proline-alanine-rich kinase and WNK4. Am J Physiol Cell Physiol. Jan: 290:C134-42.

Ganz R, Swain M, Traber P, DalCanto M, Butterworth RF, Blei AT (1989): Ammonia-induced swelling of rat cerebral cortical slices: implications for the pathogenesis of brain edema in acute hepatic failure. Metab Brain Dis 4:213-23.

Gähwiler BH, Capogna M, Debanne D, McKinney RA, Thompson SM (1997): Organotypic slice cultures: a technique has come of age. Trends Neurosci 20:471-477.

Giménez I, Forbush B (2003): Short-term stimulation of the renal Na-K-Cl cotransporter (NKCC2) by vasopressin involves phosphorylation and membrane translocation of the protein. J Biol Chem 278:26946-51.

Goh JJ, Manahan-Vaughan D (2013): Spatial object recognition enables endogenous LTD that curtails LTP in the mouse hippocampus. Cereb Cortex 23:1118-25.

Griffin WS, Stanley LC, Ling C, et al. (1989): Brain interleukin 1 and S-100 immunoreactivity are elevated in Down syndrome and Alzheimer disease. Proc Natl Acad Sci USA 86:7611–7615.

Gris P, Tighe A, Levin D, Sharma R, Brown A (2007): Transcriptional regulation of scar gene expression in primary astrocytes. Glia 55:1145-55.

Guénette SY (2003): Astrocytes: a cellular player in Abeta clearance and degradation. Trends Mol Med 9:279-80

Haas M, Forbush B 3rd (2000): The Na-K-Cl cotransporter of secretory epithelia. Annu Rev Physiol 62:515-34. Review.

Haass C, Selkoe DJ (1993): Cellular processing of beta-amyloid precursor protein and the genesis of amyloid beta-peptide. Cell 75:1039-42. Review.

Haass C, Selkoe DJ (2007): Soluble protein oligomers in neurodegeneration: lessons from the Alzheimer's amyloid beta-peptide. Nat Rev Mol Cell Biol 8:101-12.

Haber M, Zhou L, Murai KK (2006): Cooperative astrocyte and dendritic spine dynamics al hippocampal excitatory synapses. J Neuroscie 26:8881-8891.

Halassa MM, Fellin T, Haydon PG (2007): The tripartite synapse: roles for gliotransmission in health and disease. Trends in Mol Med 13:54-63.

Hannemann A, Flatman PW (2011): Phosphorylation and transport in the Na-K-2Cl cotransporters, NKCC1 and NKCC2A, compared in HEK-293 cells. PLoS One. 6:e17992.

Hartmann AM, Nothwang HG (2011): Opposite temperature effect on transport activity of KCC2/KCC4 and N(K)CCs in HEK-293 cells. BMC Res Notes 4:526.

Herrmann JE, Imura T, Song B, Qi J, Ao Y, Nguyen TK, Korsak RA, Takeda K, Akira S, Sofroniew MV (2008): STAT3 is a critical regulator of astrogliosis and scar formation after spinal cord injury. J Neurosci. 28:7231-43.

Heneka MT, Rodríguez JJ, Verkhratsky A (2010): Neuroglia in neurodegeneration. Brain Res Rev 63:189-211.

Hille B (1973): Potassium channels in myelinated nerve. Selective permeability to small cations. J Gen Physiol 61:669-86.

Hirrlinger PG, Wurm A, Hirrlinger J, Bringmann A, Reichenbach A (2008): Osmotic swelling characteristics of glial cells in the murine hippocampus, cerebellum, and retina *in situ*. Jof Neurochem 105:1405-1417.

Hoffmann EK, Lambert IH, Pedersen SF (2009): Physiology of cell volume regulation in vertebrates. Physiol. Rev 89:193-277.

Holopainen IE (2005): Organotypic hippocampal slice cultures: a model system to study basic cellular and molecular mechanisms of neuronal cell death, neuroprotection, and synaptic plasticity. Neurochem Research 30:26-43.

Holm LM, Jahn TP, Møller AL, Schjoerring JK, Ferri D, Klaerke DA, Zeuthen T (2005): NH3 and NH4+ permeability in aquaporin-expressing Xenopus oocytes. Pflugers Arch 450:415-28.

Huang CH, Ye M (2010): The Rh protein family: gene evolution, membrane biology, and disease association. Cell Mol Life Sci 67:1203-18.

Hsu JY, Bourguignon LY, Adams CM, Peyrollier K, Zhang H, Fandel T, Cun CL, Werb Z, Noble-Haeusslein LJ (2008): Matrix metalloproteinase-9 facilitates glial scar formation in the injured spinal cord. J Neurosci 28:13467-77.

Iliff JJ, Wang M, Liao Y, Plogg BA, Peng W, Gundersen GA, Benveniste H, Vates GE, Deane R, Goldman SA, Nagelhus EA, Nedergaard M (2012): A paravascular pathway facilitates CSF flow through the brain parenchyma and the clearance of interstitial solutes, including amyloid β. Sci Transl Med 4:147ra111.

Jayakumar AR, Rao KV, Murthy ChR, Norenberg MD (2006): Glutamine in the mechanism of ammonia-induced astrocyte swelling. Neurochem Int 48:623-628.

Jayakumar AR, Liu M, Moriyama M, Ramakrishnan R, Forbush B, 3rd, Reddy PV, Norenberg MD (2008): Na-K-Cl Cotransporter-1 in the mechanism of ammonia-induced astrocyte swelling. J Biol Chem 283:33874-33882.

Jayakumar AR, Norenberg MD (2010): The Na-K-Cl Co-transporter in astrocyte swelling. Metab Brain Dis 25:31-38.

John GR1, Lee SC, Brosnan CF (2003): Cytokines: powerful regulators of glial cell activation. Neuroscientist 9:10-22.

Kafitz KW, Meier SD, Stephan J, Rose CR (2008): Developmental profile and properties of sulforhodamine 101 – labelled glial cells in acute brain slices of rat hippocampus. J Neurosci Methods 169:84-92.

Kahle KT, Simard JM, Staley KJ, Nahed BV, Jones PS, Sun D (2009): Molecular mechanisms of ischemic cerebral edema: role of electroneutral ion transport. Physiology 24:257-265.

Kandel ER (1991): Nerve Cell and behavior. In: Principles of neural science (Kandel ER, Schwartz JH, Jessel TM, eds) pp 18-32. New York: Elsevier Science Publishing.

Kashon ML, Ross GW, O'Callaghan JP, et al. (2004): Associations of cortical astrogliosis with cognitive performance and dementia status. J Alzheimers Dis 6:595– 604.

Kawano H, Kimura-Kuroda J, Komuta Y, Yoshioka N, Li HP, Kawamura K, Li Y, Raisman G. (2012): Role of the lesion scar in the response to damage and repair of the central nervous system. Cell Tissue Res 349:169-80.

Kelly T, Kafitz KW, Roderigo C, Rose CR (2009): Ammonium-evoked alterations in intracellular sodium and pH reduce glial glutamate transport activity. Glia 57: 921-934.

Kelly T, Rose CR (2010): Ammonium influx pathways into astrocytes and neurons of hippocampal slices. J. Neurochem. 115:1123-1136.

Kimelberg, HK (2010): Functions of mature mammalian astrocytes: a current view. Neuroscientist 16:79-106. Review.

Klein JD, Perry PB, O'Neill WC (1993): Regulation by cell volume of Na(+)-K(+)-2Cl-cotransport in vascular endothelial cells: role of protein phosphorylation. J Membr Biol 132:243-52.

Koehler RC, Roman RJ, Harder DR (2009): Astrocytes and the regulation of cerebral blood flow. Trends Neurosci 32:160-9.

Kofuji P, Newman E, 2009 Regulation of potassium by glial cells in the central nervous system. Springer, New York: 151-175.

Kosenko E, Kaminsky YG, Felipo V, Miñana MD, Grisolía S (1993): Chronic hyperammonemia prevents changes in brain energy and ammonia metabolites induced by acute ammonium intoxication. Biochim Biophys Acta 1180:321-6.

Kuchibhotla KV, Lattarulo CR, Hyman BT, Bacskai BJ (2009): Synchronous hyperactivity and intercellular calcium waves in astrocytes in Alzheimer mice. Science 323:1211-5.

Kurihara K, Moore-Hoon ML, Saitoh M, Turner RJ (1999): Characterization of a phosphorylation event resulting in upregulation of the salivary Na(+)-K(+)-2Cl(-) cotransporter. Am J Physiol 277:C1184-93.

Kunkler PE, Kraig RP (1997): Reactive astrocytosis from excitotoxic injury in hippocampal organ culture parallels that seen in vivo. J Cereb Blood Flow and Metabol, 17:26–43.

Latorre R, Miller C (1983): Conduction and selectivity in potassium channels. J Membr Biol. 71:11-30.

Lavenex P, Lavenex PB, Amaral DG (2007): Spatial relational learning persists following neonatal hippocampal lesions in macaque monkeys. Nat Neurosci 10:234-9.

Lavoie J, Giguère JF, Layrargues GP, Butterworth RF (1987): Amino acid changes in autopsied brain tissue from cirrhotic patients with hepatic encephalopathy. J Neurochem 49:692-7.

Lledo PM, Alonso M, Grubb MS (2006): Adult neurogenesis and functional plasticity in neuronal circuits. Nat Rev Neurosci 7:179-93. Review.

Lushnikova I, Skibo G., Muller D, Nikonenko (2009): Synaptic potentiation induces increased glial coverage of excitatory synapses in CA1 hippocampus. Hippocampus 19:753-762.

Lytle C, Forbush B 3rd (1992): The Na-K-Cl cotransport protein of shark rectal gland. II. Regulation by direct phosphorylation. J Biol Chem 267:25438-43.

Manley GT, Fujimura M, Ma T, Noshita N, Filiz F, Bollen AW, Chan P, Verkman AS (2000): Aquaporin-4 deletion in mice reduces brain edema after acute water intoxication and ischemic stroke. Nat Med 6:159–163.

Martin SJ, Grimwood PD, Morris RG (2000): Synaptic plasticity and memory: an evaluation of the hypothesis. Annu Rev Neurosci 23:649-711.

Maragakis NJ, Rothstein JD (2006): Mechanisms of Disease: astrocytes in neurodegenerative disease. Nat Clin Pract Neurol 2:679-89. Review.

McManus ML, Churchwell KB, Strange K (1995): Regulation of Cell Volume in Health and Disease. N Engl J Med 333:1260-6.

Meda L, Baron P, Scarlato G (2001): Glial activation in Alzheimer's disease: the role of Abeta and its associated proteins. Neurobiol Aging 22:885-93. Review.

Meier SD, Kovalchuk Y, Rose CR (2006): Properties of the new fluorescent Na+ indicator CoroNa Green: Comparison with SBFI and confocal Na+ Imaging. J Neurosci Methods 155: 251-259.

Middeldorp J1, Hol EM (2011): GFAP in health and disease. Prog Neurobiol 93:421-43.

Moriguchi T, Urushiyama S, Hisamoto N, Iemura S, Uchida S, Natsume T, Matsumoto K, Shibuya H (2005): WNK1 regulates phosphorylation of cation-chloride-coupled cotransporters via the STE20-related kinases, SPAK and OSR1. J Biol Chem. Dec 280:42685-93.

Murthy CR, Rama Rao KV, Bai G, Norenberg MD (2001): Ammonia-induced production of free radicals in primary cultures of rat astrocytes. J Neurosci Res 66:282-8.

Müller-Schiffmann A, Herring A, Abdel-Hafiz L, SChäble S, Wedel D, van Stegen B, Horn AHC, Sticht H, Gottmann K, de Souza Silva MA, Keyvani K, Korth K (2014): Abeta dimers are sufficient to cause cognitive impairments in the absence of plaques. Poster Trieste PRION2014

Müller-Schiffmann A, Andreyeva A, Horn AH, Gottmann K, Korth C, Sticht H (2011): Molecular engineering of a secreted, highly homogeneous, and neurotoxic aβ dimer. ACS Chem Neurosci 2:242-8.

Mrak RE, Griffin WS (2005): Glia and their cytokines in progression of neurodegeneration. Neurobiol Aging 26:349-54. Review.

Nagaraja TN, Brookes N (1998): Intracellular acidification induced by passive and active transport of ammonium ions in astrocytes. Am J Physiol 274:C883-891.

Nagele RG, D'Andrea MR, Lee H, Venkataraman V, Wang HY (2003): Astrocytes accumulate A beta 42 and give rise to astrocytic amyloid plaques in Alzheimer disease brains. Brain Res. 971:197-209.

Nagele RG, DÁndrea MR, Lee H, Venkataraman V, Imaki H, Wang KC, Wegiel J (2004): Contribution of glial cells to the development of amyloid plaques in Alzheimer´s disease. Neurobiol Aging 25:663-674.

Nagelhus EA, Horio Y, Inanobe A, Fujita A, Haug FM, Nielsen S, Kurachi Y, Ottersen OP (1999): Immunogold evidence suggests that coupling of K+ siphoning and water transport in rat retinal Müller cells is mediated by a coenrichment of Kir4.1 and AQP4 in specific membrane domains. Glia 26:47-54.

Nagelhus EA, Ottersen OP (2013): Physiological roles of aquaporin-4 in brain. Physiol Rev 93:1543-62. Review.

Neary JT, Kang Y, Willoughby KA, Ellis EF (2003): Activation of extracellular signal-regulated kinase by stretch-induced injury in astrocytes involves extracellular ATP and P2 purinergic receptors. J Neurosci 23:2348-56.

Neves G, Cooke SF, Bliss TV (2008): Synaptic plasticity, memory and the hippocampus: a neural network approach to causality. Nat Rev Neurosci 9:65-75.

Nielsen S, Nagelhus EA, Amiry-Moghaddam M, Bourque C, Agre P, Ottersen OP (1997): Specialized membrane domains for water transport in glial cells: high-resolution immunogold cytochemistry of aquaporin-4 in rat brain. J Neurosci 17:171-80.

Nicoll JA, Weller RO (2003): A new role for astrocytes: beta-amyloid homeostasis and degradation. Trends Mol Med 9:281-2.

Nimmerjahn A, Helmchen F (2012): In vivo labeling of cortical astrocytes with sulforhodamine 101 (SR101). Cold Spring Harb Protoc. 1:326-34.

Nimmerjahn A, Kirchhoff F, Kerr JN, Helmchen F (2004): Sulforhodamine 101 as a specific marker of astroglia in the neocortex in vivo. Nat Methods 1:31-37.

Nishida H, Okabe S (2007): Direct astrocytic contacts regulate local maturation of dendritic spines. J Neurosci 27:331–340.

Norenberg MD, Jajakumar AR, Rama Rao KV, Panickar KS (2007): New concepts in the mechanism of ammonia induces astrocyte swelling. Metab Brain Dis 22:219-234.

Norenberg MD, Rama Rao KV, Jayakumar AR (2009): Signaling factors in the mechanism of ammonia neurotoxicity. Metab Brain Dis 24:103-17.

Oddo S, Caccamo A, Shepherd JD, Murphy MP, Golde TE, Kayed R, Metherate R, Mattson MP, Akbari Y, LaFerla FM (2003): Triple-transgenic model of Alzheimer's disease with plaques and tangles: intracellular Abeta and synaptic dysfunction. Neuron 39:409-21.

O'Donnell ME, Lam TI, Tran LQ, Foroutan S, Anderson SE (2006): Estradiol reduces activity of the blood-brain barrier Na-K-Cl cotransporter and decreases edema formation in permanent middle cerebral artery occlusion. J Cereb Blood Flow Metab 26:1234-49.

Olabarria M, Noristani HN, Verkhratsky A, Rodríguez JJ (2010): Concomitant astroglial atrophy and astrogliosis in a triple transgenic animal model of Alzheimer's disease. Glia 58:831-8.

Ott P, Larsen FS (2004): Blood-brain barrier permeability to ammonia in liver failure: a critical reappraisal. Neurochem Int 44:185-98. Review.

Pasantes-Morales H (1996): Volume regulation in brain cells: cellular and molecular mechanisms. Metab Brain Dis 11:187-204. Review

Pasantes-Morales H, Cardin V, Tuz K (2000): Signaling events during swelling and regulatory volume decrease. Neurochem Res 25:1301-14. Review.

Pasantes-Morales H, Franco R, Ochoa L, Ordaz B (2002): Osmosensitive release of neurotransmitter amino acids: relevance and mechanisms. Neurochem Res 27:59-65. Review.

Payne JA, Forbush B 3rd (1995): Molecular characterization of the epithelial Na-K-Cl cotransporter isoforms. Curr Opin Cell Biol 7:493-503. Review.

Pekny M, Nilsson M (2005): Astrocyte activation and reactive gliosis. Glia 50:427-434

Pellerin L, Magistretti PJ (2003): Food for thought: challenging the dogmas. J Cereb Blood Flow Metab 23:1282-6.

Pellerin L, Bouzier-Sore AK, Aubert A, Serres S, Merle M, Costalat R, Magistretti PJ (2007): Activity-dependent regulation of energy metabolism by astrocytes: an update. Glia 55:1251-62. Review.

Perea G, Navarrete M, Araque A (2009): Tripartite synapses: astrocytes process and control synaptic information. Trends in Neurosci 32:421-31.

Pewitt EB, Hegde RS, Haas M, Palfrey HC (1990): The regulation of Na/K/2Cl cotransport and bumetanide binding in avian erythrocytes by protein phosphorylation and dephosphorylation. Effects of kinase inhibitors and okadaic acid. J Biol Chem 265:20747-56.

Piechotta K1, Garbarini N, England R, Delpire E (2003): Characterization of the interaction of the stress kinase SPAK with the Na+-K+-2Cl- cotransporter in the nervous system: evidence for a scaffolding role of the kinase. J Biol Chem 278:52848-56.

Price DL, Ludwig JW, Mi H, Schwarz TL, Ellisman MH (2002): Distribution of rSlo Ca2+-activated K+ channels in rat astrocyte perivascular endfeet. Brain Res 956:183-93.

Rama Rao KV, Jayakumar AR, Norenberg DM (2003): Ammonia neurotoxicity: role of the mitochondrial permeability transition. Metab Brain Dis 18:113-27. Review.

Rama Rao KV, Norenberg MD (2014): Glutamine in the pathogenesis of hepatic encephalopathy: the trojan horse hypothesis revisited. Neurochem Res 39:593-8. Review.

Raponi E, Agenes F, Delphin C et al. (2007): S100ß expression defines a state in which GFAP-expressing cells lose their neural stem cell potential and aquire a more mature developmental stage. Glia 55:165-177.

Ratnakumari L, Qureshi IA, Butterworth RF (1994): Regional amino acid neurotransmitter changes in brains of spf/Y mice with congenital ornithine transcarbamylase deficiency. Metab Brain Dis 9:43-51.

Reinehr R, Görg B, Becker S, Qvartskhava N, Bidmon HJ, Selbach O, Haas HL, Schliess F, Häussinger D (2007): Hypoosmotic swelling and ammonia increase oxidative stress by NADPH oxidase in cultured astrocytes and vital brain slices. Glia 55:758-71.

Retamal MA, Froger N, Palacios-Prado N, Ezan P, Sáez PJ, Sáez JC, Giaume C (2007): Cx43 hemichannels and gap junction channels in astrocytes are regulated oppositely by proinflammatory cytokines released from activated microglia. J Neurosci 27:13781-92.

Ridet J L, Malhotra S K, Privat A., Gage FH (1997): Reactive astrocytes: cellular and molecular cues to biological function. Trends Neurosci 20:570-7.

Risher WC, Andrew RD, Kirov SA (2009): Real-time passive volume responses of astrocytes to acute osmotic and ischemic stress in cortical slices and *in vivo* revealed by two-photon microscopy. Glia 57:207-221.

Rodríguez JJ1, Olabarria M, Chvatal A, Verkhratsky A (2009): Astroglia in dementia and Alzheimer's disease. Cell Death Differ 16:378-85.

Rose CR, Ransom BR (1996): Intracellular sodium homeostasis in rat hippocampal astrocytes. J Physiol 491, 2:291-305.

Rose CR, Ransom BR, Waxman SG (1998): Effects of glucose deprivation, chemical hypoxia, and simulated ischemia on Na+ homeostasis in rat spinal cord astrocytes. J Neurosci 18:3554-3562.

Rose CR (1997): Intracellular Na+ regulation in neurons and glia: Functional implications. The Neuroscientist 3:85-88.

Rosen AS, Andrew RD (1990): Osmotic effects upon excitability in rat neocortical slices. Neuroscience. 38:579-90.

Rossner S, Lange-Dohna C, Zeitschel U, Perez-Polo JR (2005): Alzheimer's disease beta-secretase BACE1 is not a neuron-specific enzyme. J Neurochem 92:226-34.

Rothstein JD, Dykes-Hoberg M, Pardo CA, Bristol LA, Jin L, Kuncl RW, Kanai Y, Hediger MA, Wang Y, Schielke JP, Welty DF (1996): Knockout of glutamate transporters reveals a major role for astroglial transport in excitotoxicity and clearance of glutamate. Neuron 16:675-86.

Roy ML, Saal D, Perney T, Sontheimer H, Waxman SG, Kaczmarek LK (1996): Manipulation of the delayed rectifier Kv1.5 potassium channel in glial cells by antisense oligodeoxynucleotides. Glia 18:177-84.

Russell JM (2000): Sodium-potassium-chloride cotransport. Physiol Rev 80:211-76. Review.

Selvaraj NG, Omi E, Gibori G, Rao MC (2000): Janus kinase 2 (JAK2) regulates prolactin-mediated chloride transport in mouse mammary epithelial cells through tyrosine phosphorylation of Na+-K+-2Cl- cotransporter. Mol Endocrinol. 2000 Dec: 14:2054-65.

Schiodt FV, Atillasoy E, Shakil AO, Schiff ER, Caldwell C, Kowdley KV, Stribling R, Crippin JS, Flamm S, Somberg KA, Rosen H, McCashland TM, Hay JE, Lee WM (1999): Etiology and outcome for 295 patients with acute liver failure in the United States. Liver Transpl Surg. 5:29-34

Schreiner EA, Berlinger E, Langer J, Kafitz KW, Rose CR (2013): Lesion-induced alterations in astrocyte glutamate transporter expression and function in the hippocampus. ISRN Neurol 3:893605.

Sheng JG, Mrak RE, Rovnaghi CR, Kozlowska E, Van Eldik LJ, Griffin WS (1996): Human brain S100 beta and S100 beta mRNA expression increases with age: pathogenic implications for Alzheimer's disease. Neurobiol Aging 17:359-63.

Silver J, Miller JH (2004): Regeneration beyond the glial scar. Nat Rev Neurosci 5:146-56. Review.

Simard M, Nedergaard M (2004): The neurobiology of glia in the context of water and ion homeostasis. Neurosci 129: 877-896.

Simpson JE, Ince PG, Lace G, Forster G, Shaw PJ, Matthews F, Savva G, Brayne C, Wharton SB (2010): Astrocyte phenotype in relation to Alzheimer-type pathology in the ageing brain. Neurobiol Aging 31:578-90.

Sinke AP, Jayakumar AR, Panickar KS, Moriyama M, Reddy PV, Norenberg MD (2008): NFkappaB in the mechanism of ammonia-induced astrocyte swelling in culture. J Neurochem. 106:2302-11.

Sofroniew MV (2005): Reactive astrocytes in neural repair and protection. Neuroscientist 11:400-7. Review.

Sofroniew MV (2009): Molecular dissection of reactive astrogliosis and glial scar. NIH-PA 32:638-647.

Sontheimer H (1992): Astrocytes, as well as neurons, express a diversity of ion channels. Can J Physiol Pharmacol. 70:223-38.

Stephan J (2011): Dissertation: Mechanisms of ammonium-induced depolarization of astrocytes *in situ*.

Stephan J, Haack N, Kafitz KW, Durry S, Koch D, Hochstrate P, Seifert G, Steinhäuser C, Rose CR (2012): Kir4.1 channels mediate a depolarization of hippocampal astrocytes under hyperammonemic conditions in situ. Glia 60:965-78.

Stevens B, Allen NJ, Vazquez LE, Howell GR, Christopherson KS, Nouri N, Micheva KD, Mehalow AK, Huberman AD, Stafford B, Sher A, Litke AM, Lambris JD, Smith SJ, John SW, Barres BA (2007): The classical complement cascade mediates CNS synapse elimination. Cell 131:1164-78.

Stoppini L, Buchs P-A, Muller D (1991): A simple method for organotypic cultures of nervous tissue. J Neurosci Methods 37:173-182.

Strange K (1992): Regulation of solute and water balance and cell volume in the central nervous system. J. Am. Soc. Nephrol 3:12-27.

Su G, Kintner DB, Sun D (2002b): Contribution of Na^+-K^+-Cl^- cotransporter to high-$[K^+]_o$-induced swelling and EAA release in astrocytes. Am J Physiol Cell Physiol 282:C1136-46.

Swain M, Butterworth RF, Blei AT (1992): Ammonia and related amino acids in the pathogenesis of brain edema in acute ischemic liver failure in rats. Hepatology 15:449-53.

Swain MS, Bergeron M, Audet R, Blei AT, Butterworth RF (1992): Monitoring of neurotransmitter amino acids by means of an indwelling cisterna magna catheter: a comparison of two rodent models of fulminant liver failure. Hepatology 16:1028-35.

Takahashi H, Koehler RC, Brusilow SW, Traystman RJ (1991): Inhibition of brain glutamine accumulation prevents cerebral edema in hyperammonemic rats. Am J Physiol 261:H825-9.

Takami M, Nagashima Y, Sano Y, Ishihara S, Morishima-Kawashima M, Funamoto S, Ihara Y (2009): gamma-Secretase: successive tripeptide and tetrapeptide release from the transmembrane domain of beta-carboxyl terminal fragment. J Neurosci 29:13042-52.

Takano T, He W, Han X, Wang F, Xu Q, Wang X, Oberheim Bush NA, Cruz N, Dienel GA, Nedergaard M (2014): Rapid manifestation of reactive astrogliosis in acute hippocampal brain slices. Glia 62:78-95.

Thrane AS, Rangroo Thrane V, Nedergaard M (2014): Drowning stars: reassessing the role of astrocytes in brain edema. Trends Neurosci 37:620-8.

Titz S, Hormuzdi S, Lewen A, Monyer H, Misgeld U (2006): Intracellular acidification in neurons induced by ammonium depends on KCC2 function. Eur J Neurosci 23:454-64.

Traber PG, Dal Canto M, Ganger DR, Blei AT (1987): Electron microscopic evaluation of brain edema in rabbits with galactosamine-induced fulminant hepatic failure: ultrastructure and integrity of the blood-brain barrier. Hepatology 7:1272-7.

Traynelis SF, Dingledine R (1998): Role of extracellular space in hyperosmotic suppression of potassium-induced electrographic seizures. J Neurophysiol. 61:927-38.

Verkhratsky A, Olabarria, Noristani HN, Chia-Yu Yeh, JJ Rodriguez (2010): Astrocytes in Alzheimer´s Disease. Neurotherapeuthics 7:399-412.

Verkhratsky A, Nedergaard M, Hertz L (2014): Why are astrocytes important? Neurochem Res 40:389-401.

Vitari AC, Deak M, Morrice NA, Alessi DR (2005): The WNK1 and WNK4 protein kinases that are mutated in Gordon's hypertension syndrome phosphorylate and activate SPAK and OSR1 protein kinases. Biochem J 391:17-24.

Wanner IB, Deik A, Torres M, Rosendahl A, Neary JT, Lemmon VP, Bixby JL (2008): A new in vitro model of the glial scar inhibits axon growth. Glia 56:1691-709.

Whitlock JR, Heynen AJ, Shuler MG, Bear MF (2006): Learning induces long-term potentiation in the hippocampus. Science 313:1093-7.

Wong JA1, Gosmanov AR, Schneider EG, Thomason DB (2001): Insulin-independent, MAPK-dependent stimulation of NKCC activity in skeletal muscle. Am J Physiol Regul Integr Comp Physiol 281:R561-71.

Wyss-Coray T, Loike JD, Brionne TC, Lu E, Anankov R, Yan F, Silverstein SC, Husemann J (2003): Adult mouse astrocytes degrade amyloid-beta in vitro and in situ. Nat Med 9:453-7.

Yan Y, Dempsey RJ, Sun D (2001): Expression of Na(+)-K(+)-Cl(-) cotransporter in rat brain during development and its localization in mature astrocytes. Brain Res 911:43-55.

Zador Z, Stiver S, Wang V, Manley GT (2009): Role of aquaporin-4 in cerebral edema and stroke. Handb Exp Pharmacol 190:159-70. Review.

Zeidel ML (1996): Low permeabilities of apical membranes of barrier epithelia: what makes watertight membranes watertight? Am J Physiol 271:F243-5.

Zhou M, Xu G, Xie M, Zhang X, Schools GP, Ma L, Kimelberg HK, Chen H (2009): TWIK-1 and TREK-1 are potassium channels contributing significantly to astrocyte passive conductance in rat hippocampal slices. J Neurosci 29:8551-64.

B Publications

Alexandra E. Schreiner, Eric Berlinger, Julia Langer, Karl W. Kafitz, and Christine R. Rose, "Lesion-Induced Alterations in Astrocyte Glutamate Transporter Expression and Function in the Hippocampus," ISRN Neurology, vol. 2013, Article ID 893605, 16 pages, 2013. doi:10.1155/2013/8936

My contributions:

- Image processing.
- Manual encirclement of astrocyte somata in confocal images of hippocampal slice cultures of GFP-GFAP expressing mice.
- Calculation of the soma area values.
- Statistical examination of the obtained results.
- Data presentation.

Hindawi Publishing Corporation
ISRN Neurology
Volume 2013, Article ID 893605, 16 pages
http://dx.doi.org/10.1155/2013/893605

Research Article

Lesion-Induced Alterations in Astrocyte Glutamate Transporter Expression and Function in the Hippocampus

Alexandra E. Schreiner, Eric Berlinger, Julia Langer, Karl W. Kafitz, and Christine R. Rose

Institute of Neurobiology, Heinrich Heine University Duesseldorf, Universitaetsstraße 1, Building 26.02.00, 40225 Duesseldorf, Germany

Correspondence should be addressed to Christine R. Rose; rose@hhu.de

Received 3 July 2013; Accepted 27 July 2013

Academic Editors: S. C. Barnett and J.-I. Satoh

Astrocytes express the sodium-dependent glutamate transporters GLAST and GLT-1, which are critical to maintain low extracellular glutamate concentrations. Here, we analyzed changes in their expression and function following a mechanical lesion in the CA1 area of organotypic hippocampal slices. 6-7 days after lesion, a glial scar had formed along the injury site, containing strongly activated astrocytes with increased GFAP and S100β immunoreactivity, enlarged somata, and reduced capability for uptake of SR101. Astrocytes in the scar's periphery were swollen as well, but showed only moderate upregulation of GFAP and S100β and efficiently took up SR101. In the scar, clusters of GLT-1 and GLAST immunoreactivity colocalized with GFAP-positive fibers. Apart from these, GLT-1 immunoreactivity declined with increasing distance from the scar, whereas GLAST expression appeared largely uniform. Sodium imaging in reactive astrocytes indicated that glutamate uptake was strongly reduced in the scar but maintained in the periphery. Our results thus show that moderately reactive astrocytes in the lesion periphery maintain overall glutamate transporter expression and function. Strongly reactive astrocytes in the scar, however, display clusters of GLAST and GLT-1 immunoreactivity together with reduced glutamate transport activity. This reduction might contribute to increased extracellular glutamate concentrations and promote excitotoxic cell damage at the lesion site.

1. Introduction

Glutamate reuptake represents the principal mechanism for inactivation of synaptically released glutamate [1, 2]. In the rodent hippocampus, it is mainly accomplished by astrocytic glutamate transporters (EAATs: excitatory amino acid transporters), namely, GLAST (glutamate/aspartate transporter) and GLT-1 (glutamate-transporter-1; rodent analogues of EAAT1 and EAAT2, resp.; [3–7]). Glutamate uptake is energized by the concomitant inward transport of three sodium ions and a proton, while one potassium ion is transported outward. Consequently, its activation is accompanied by an increase in the intracellular sodium concentration of astrocytes [8, 9].

Under pathological conditions, astrocytes undergo a complex reaction referred to as reactive astrogliosis, which is seen in diverse preparations and conditions ranging from primary cell culture to the intact brain [10, 11]. The hallmarks of reactive gliosis are a massive upregulation of the expression of the intermediate filament *Glial Fibrillary Acidic Protein* (GFAP) and a cellular hypertrophy [12, 13]. Reactive astrocytes display several features of immature astrocytes (e.g., [14, 15]) and can partially reenter the cell cycle [16, 17]. The degree of astrogliosis can vary depending on the specific insult. Following traumatic brain injury, a dense glial scar forms at the lesion site due to strong astrocytic reorganization and proliferation [10, 11, 18]. At some distance to the lesion and scar, astrocytes usually do not divide, and their morphological reorganization and hypertrophy is less severe. The establishment of a glial scar around injured tissue is regarded as hindrance for the growth and regeneration of axons [19, 20]. Notwithstanding, reactive astrocytes might also exert a protective role and support regeneration [11, 13, 21].

There is evidence that reactive gliosis is also accompanied by an alteration in the expression level of glial glutamate transporters [6]. Most studies performed in the rodent and human brain reported an overall downregulation of protein levels of both GLAST and GLT-1 and/or a reduction in functional glutamate uptake in response to brain injury and astrogliosis, respectively (e.g., [22–27]). The reduction in the expression of glial glutamate transporters has been suggested to contribute to the elevation of extracellular glutamate concentrations and to glutamate-mediated excitotoxicity which is observed under many pathological conditions.

Injury-induced changes in the expression of the glutamate transporter subtypes might, however, also depend on the degree of astrogliosis. This might be especially relevant and visible upon a mechanical lesion, where reactivity of astrocytes, as judged for example based on their GFAP expression and morphology, ranges from severe astrogliosis in the scar region to only moderate-mild astrogliosis distant from the lesion [10, 11]. To study this question, we analyzed expression of GLAST and GLT-1 following a mechanical lesion in organotypic tissue slice cultures of the mouse hippocampus. Furthermore, we employed ratiometric sodium imaging as functional assay for glutamate uptake in astrocytes. Our results show that mechanical tissue injury generates subsets of reactive astrocytes depending on the distance from the lesion site, which differ in both morphological features and their ability to take up SR101. Furthermore, these subsets show discrete changes in glutamate transporter expression and glutamate uptake capacity, indicating that glutamate clearance might be largely functional in the periphery of the lesion, but strongly hampered in the scar region.

2. Materials and Methods

2.1. Ethics Statement. This study was carried out in strict accordance with the institutional guidelines of the Heinrich Heine University Duesseldorf, Germany, as well as the European Community Council Directive (86/609/EEC). All experiments were communicated to and approved by the Animal Welfare Office at the Animal Care and Use Facility of the Heinrich Heine University Duesseldorf, Germany (institutional act number: O52/05). In accordance with the German Animal Welfare Act (Tierschutzgesetz, Articles 4 and 7), no formal additional approval for the postmortem removal of brain tissue was necessary. For generation of acute slices, mice were quickly decapitated (following the recommendation of the European Commission published in: Euthanasia of experimental animals, Luxembourg: Office for Official Publications of the European Communities, 1997; ISBN 92-827-9694-9).

2.2. Preparation of Tissue Slice Cultures. Acute tissue slices of the hippocampus were prepared from Balb/c mice (*Mus musculus*) of both genders at postnatal days 7 to 8 (P7-8) using standard procedures. For some experiments, transgenic animals (FVB/N-Tg[GFAPGFP]14Mes/J) expressing green fluorescence protein (GFP) under the GFAP promoter were used (obtained from Jackson Laboratory; Harbor, USA). After decapitation of the animals, brains were quickly excised and hemisected in ice-cold artificial cerebrospinal fluid (ACSF) composed of (in mM) 125 NaCl, 2.5 KCl, 2 $CaCl_2$, 1 $MgCl_2$, 1.25 NaH_2PO_4, 26 $NaHCO_3$, and 20 glucose, bubbled with 95% O_2 and 5% CO_2, and adjusted to a pH of 7.4. Hemisections were trimmed, and transverse slices (200 μm) comprising the entorhinal cortex, hippocampus, fimbria, and thalamus were prepared using a vibratome (Microm HM650V, Thermo Fischer Scientific, Walldorf, Germany). Slices were transferred to ACSF at 35°C for 30 minutes.

Organotypic hippocampal slice cultures were prepared and cultured according to the protocol introduced by Stoppini et al. [28] with minor modifications. To this end, acute slices were transferred to a Millicell culture insert (PICM ORG 50, hydrophilized PTFE, pore size 0.4 μm; Merck Millipore, Darmstadt, Germany) and maintained at the interface of a serum-based culture medium free of antibiotics in a humidified incubator atmosphere of 5% CO_2 at 37°C. The culture medium was composed of 30% sterile filtered normal horse serum (NHS; GIBCO/Life Technologies, Darmstadt, Germany), 30% Dulbecco's modified eagle medium (DMEM; GIBCO/Life Technologies, Darmstadt, Germany), and 40% Hank's balanced salt solution (HBSS; GIBCO/Life Technologies, Darmstadt, Germany) supplemented with 38 mM glucose (pH adjusted to 7.3-7.4). The medium was changed three times a week, and the insert surface was washed with medium once a week.

After at least 12 days in culture, a mechanical lesion was performed using a sterile scalpel blade. The lesion was positioned in the CA1 area perpendicular to the *stratum pyramidale*, included the *strata oriens*, *pyramidale*, *radiatum*, and *lacunosum moleculare*, and spanned the entire depth of the slice (cf. Figure 2). After lesioning, slice cultures were maintained for another 6-7 days (designated as 6-7 days postlesion). Unlesioned control slices were cultured in parallel for a corresponding number of days.

For visualization of cell death, ACSF containing 0.5 μg/mL propidium iodide (PI) was applied to the slice surface and incubated for 3 hours at 37°C and 5% CO_2, followed by a wash with ACSF. Documentation was either accomplished with an epifluorescence microscope (Nikon Eclipse 90i; Nikon Instruments, Düsseldorf, Germany) or at an Olympus Fluoview300 laser scanning microscope (Olympus, Hamburg, Germany).

Astrocyte soma size in organotypic control and lesioned slices was calculated from images of GFP-fluorescence derived from GFP/GFAP mice which were obtained at a confocal microscope (Olympus Fluoview300; Olympus, Hamburg, Germany; see also below). To this end, a semiquantitative approach was used, in which somata of single cells were manually encircled (cf. Figure 4(b)), and the resulting area was calculated using ImageJ software (NIH, Bethesda, USA).

All chemicals were purchased from Sigma-Aldrich Chemical (Munich, Germany) unless stated otherwise.

2.3. Imaging Experiments. For imaging experiments, organotypic slices were excised from the Millicell inserts and incubated in ACSF containing 2.5 μM SR101 for 30 min at 35°C to stain astrocytes (see above). SR101 is a highly specific and widely used tool for the identification of mature astrocytes in many brain regions including the hippocampus

[29, 30]. It has recently been shown to be taken up into mature hippocampal astrocytes via an active transport mechanism involving organic anion transport polypeptides [31]. Widefield fluorescence imaging was performed using a variable scan digital imaging system (TILL Photonics, Martinsried, Germany) attached to an upright microscope (BX51Wi, Olympus Europe, Hamburg, Germany) and a CCD camera (TILL Imago VGA, Till Photonics, Martinsried, Germany). Images were collected with an Achroplan 40x objective (water immersion, N.A. 0.8, Zeiss, Göttingen, Germany). SR101 was excited at 575 nm, and emission was collected above 590 nm. Excitation wavelength for detection of GFP was 488 nm, and emission was collected above 510 nm.

For intracellular sodium imaging, slices were additionally incubated with the membrane permeable form of the sodium-sensitive fluorescent dye SBFI (SBFI-AM; sodium-binding benzofuran isophthalate-acetoxymethyl ester; Molecular Probes/Life Technologies, Darmstadt, Germany) as described earlier [32–34]. Ratiometric sodium imaging was performed by alternate excitation of SBFI at 340 nm (weakly sodium-sensitive wavelength) and at 380 nm (sodium-sensitive wavelength) at 4 Hz. Emission (>440 nm) was collected in defined regions of interest (ROI) representing cell bodies. Standard dynamic background correction was performed as described earlier [33, 34]. After background correction, the fluorescence ratio (F_{340}/F_{380}) was calculated for the individual ROIs and analyzed offline using OriginPro 8G Software (OriginLab Corporation, Northampton, MA, USA).

Changes in SBFI fluorescence ratio were expressed as changes in sodium concentration based on *in situ* calibrations as reported before [32, 33, 35]. To equilibrate extra- and intracellular Na^+-concentrations, SBFI-loaded slices were perfused with saline containing ionophores ($3\,\mu$M gramicidin D, $100\,\mu$M monensin) and the Na^+/K^+-ATPase blocker ouabain ($100\,\mu$M), as well as different concentrations of Na^+.

The glutamate transporter agonist D-aspartate was applied by a pressure application device (PDES-02D, NPI Electronic GmbH, Tamm, Germany) coupled to standard micropipettes (Hilgenberg, Waldkappel, Germany) placed 20–100 μm from cell bodies of selected cells.

2.4. Antibodies. Antibodies employed in this study are listed in Table 1. The following antisera were utilized, which represent well-established, commercially available standard markers: guinea-pig GLT-1 antiserum directed against the C-terminus of rat GLT-1 (Chemicon International/Millipore Corp., Carrigtwohill, Ireland; e.g., [36]) and guinea-pig GLAST antiserum directed against the C-terminus of rat GLAST (Chemicon International/Millipore Corp., Carrigtwohill, Ireland; e.g., [37]). Validation and a detailed characterization of both antibodies were provided before [38–40]. For identification of astrocytes, polyclonal rabbit antibodies against GFAP (GFAP-pAb; Dako Cytomation, Denmark; [40, 41]) and S100β (Abcam, United Kingdom; [42]) were employed. When double staining with the latter antibody was performed, a monoclonal mouse antibody detecting GFAP was used (GFAP-mAb; Sigma Aldrich, Germany; [40, 43]).

Standard fluorochrome-conjugated antibodies (AlexaFluor, Invitrogen/Life Technologies, Darmstadt, Germany) were employed as secondary antibodies for immunohistochemistry.

2.5. Immunohistochemistry. Prior to immunohistochemical processing, organotypic slices were immersion fixed for 30 min at RT in 4% paraformaldehyde (PFA) in phosphate-buffered saline (PBS) following three washes every 30 min with PBS. Cell membranes were permeabilized, and unspecific binding sites were blocked in PBS containing 0.25% triton-X100 (TX) and 2% normal goat serum (NGS; GIBCO/Life Technologies, Darmstadt, Germany) for 90 min at 4°C followed by incubation with the primary antibody GFAP-pAb (1 : 1000; Dako Cytomation, Glostrup, Denmark), diluted in the same solution over night at 4°C. In case of S100β/GFAP double stainings, slices were incubated with a mixture of the primary antibodies GFAP-mAb (1 : 1000, Dako Cytomation, Glostrup, Denmark) and rabbit-S100β (1 : 100, Abcam, United Kingdom). After five washes in PBS containing 0.25% TX and 2% NGS, slices were incubated either with guinea pig-anti-GLAST or with guinea pig-anti-GLT-1 (both 1 : 1000, diluted in 0.25% TX/2% NGS/PBS) for 4 hrs at RT. Excess primary antibody was removed with five washes using 2% NGS/PBS. Antirabbit-AlexaFluor594 and antiguinea pig-AlexaFluor488 or antimouse-AlexaFluor488 (1 : 100 in blocking solution) were used for visualization of antibody binding and incubated for 2 hrs at RT. The slices were subjected to DAPI staining ($4'$,6-diamidino-2-phenylindole; 0.5 μm; Invitrogen), washed three times, and mounted on glass slides with mowiol/DABCO (Calbiochem, Fluka, distributed by Sigma-Aldrich Chemical, Munich, Germany).

Identical conditions were applied to all performed stainings regarding tissue processing and staining procedure. Negative controls were run in parallel to each staining by either omitting all or just one of the primary antibodies. Control stainings in which one of the primary antibodies was omitted showed the identical labeling pattern for the remaining antibody as in the double stainings. Omitting both primary antibodies never resulted in a staining.

Documentation of immunofluorescence was either performed with an epifluorescence microscope (Nikon Eclipse 90i; Nikon Instruments, Düsseldorf, Germany) or a confocal laser scanning microscope (Olympus Fluoview300; Olympus, Hamburg, Germany). The epifluorescence microscope was equipped with a standard DAPI (EX 340–380; DM 400; BA 435–485), FITC (EX 465–495; DM 505; BA 515–555), and TRITC (EX 540/25; DM 365; BA 605/55) filter set. Illumination was provided by an Intensilight fiber lamp (C-GHFI; Nikon Instruments, Düsseldorf, Germany), and emission was detected with a monochrome digital camera (DS-QilMc; Nikon Instruments, Düsseldorf, Germany). Images were collected with either a 20x/0.75 (PlanApoVC, Nikon Instruments, Düsseldorf, Germany) air objective or a 60x/1.40 oil immersion objective (PlanApoVC, Nikon Instruments, Düsseldorf, Germany). NIS-Elements software (Nikon Instruments, Düsseldorf, Germany) was used for image acquisition. For confocal microscopy, an Olympus

Table 1: List of antibodies used.

Antibody	Structure of the immunogen	Company	Order number	Species	Type	Dilution
GLAST (EAAT1)	KPYQLIAQDNEPEKPV ADSETKM	Chemicon/Millipore	AB1782*	Guinea Pig IgG	Polyclonal	1:1000
GLT-1 (EAAT2)	AANGKSADCSVEEEPW KREK	Chemicon/Millipore	AB1783	Guinea Pig IgG	Polyclonal	1:1000/1:2000
GFAP	n.s. (full-length protein from cow spinal cord)	Dako Cytomation	Z 0334	Rabbit IgG	Polyclonal	1:1000/1:2000
GFAP	clone G-A-5 (LQSLTCDVESLRGTNE SLERQMREQEERHARE AASYQEALTRLEEEGQ SLKDEMARHLQEYQEL LNVKLALDIEIATY)	Sigma-Aldrich	G3893	Mouse IgG	Monoclonal	1:1000/1:2000
S100β	n.s. (recombinant full-length cow protein)	Abcam	ab868	Rabbit IgG	Polyclonal	1:100
Mouse IgG	AF488 conjugated	Invitrogen (Life Technologies)	A11029	Goat	—	1:100
Rabbit IgG	AF594 conjugated	Invitrogen (Life Technologies)	A11012	Goat	—	1:100
Guinea pig IgG	AF488 conjugated	Invitrogen (Life Technologies)	A11073	Goat	—	1:100

GLAST: glutamate aspartate transporter; GLT-1: glutamate transporter 1; GFAP: glial fibrillary protein; AF: AlexaFluor; appl.: application; IHC: immunohistochemistry; WB: western blot; n.s.: not specified.

*The manufacturer has lately stopped the sale and distribution of the GLAST antibody used here.

BX51WI microscope coupled to a confocal laser scanning system (FV300) equipped with a multiline argon (488 nm) and a helium-neon laser (543 nm, both Melles Griot, Bensheim, Germany) was used. Images were collected with either a 20x/0.50 (UMPlanFl, Olympus, Hamburg, Germany), a 40x/0.80 water immersion (LUMPlan, Olympus, Hamburg, Germany), or a 60x/1.40 oil immersion objective (PlanApoVC, Nikon Instruments, Düsseldorf, Germany). A Kalman filter 4 was employed at every scan. Simultaneous or sequential scanning of both fluorophores revealed no difference in their staining patterns, indicating absence of cross-excitation or spectral bleed through. The thickness of z-plane sections was 1 μm, and the number of optical sections varied depending on the preparation.

Figures show extended focus images as specified in the figure legends, which were calculated from z-stacks of optical sections using ImageJ software (NIH, Bethesda, USA). Images were overlaid employing Adobe Photoshop CS2 (Adobe Systems, Cologne, Germany).

2.6. Data Presentation and Statistics. Unless otherwise specified, data are expressed as means ± S.E.M. Data were statistically analyzed by Student's t-test employing the procedures implemented in OriginPro 8G Software (OriginLab Corporation, Northampton, MA, USA). A P value of <0.05 was considered significant. If not stated otherwise, n represents the number of analyzed cells and N the number of slices. Each set of experiments was performed on at least three tissue slices obtained from different animals.

3. Results

3.1. Identification of Astrocytes in Organotypic Slice Cultures. The aim of the present study was to analyze changes in glutamate transporter expression and function in astrocytes in response to a mechanical injury. To this end, we prepared organotypic tissue slice cultures of the mouse hippocampus, a well-established model system in which the layering and basic cellular organization of the neural network are maintained over time [28]. After 19–25 days in culture, organotypic tissue slices had flattened to a thickness of 40–50 μm and were composed of 3 to 4 cell layers. At this stage, propidium iodide assays detected only few dead cells dispersed throughout the slices (3 ± 0.6 cells per CA1 subfield; 18 ± 3.4 in entire preparation; $N = 6$; data not shown), indicating that the preparation was viable and in a stable condition.

To visualize astrocytes in cultured slices, we used hippocampi of transgenic mice in which green fluorescent protein (GFP) is expressed under the control of the promoter of the astrocyte-specific intermediate filament glial fibrillary acidic protein (GFAP; FVB/N-Tg[GFAPGFP]; "GFP/GFAP mice"). A visualization of the GFP fluorescence demonstrated that the general distribution and organization of astrocytes were preserved in the *strata pyramidale* and *radiatum* of the CA1 region of organotypic cultures, confirming earlier reports ($N = 3$; Figure 1(a); [44, 45]). The vast majority of GFP-expressing cells (~95%) also labeled with the astrocyte-specific vital marker SR101 in organotypic slices ($N = 3$; Figures 1(a) and 1(b)). Furthermore, immunohistochemical stainings for GFAP in slice cultures derived from wildtype

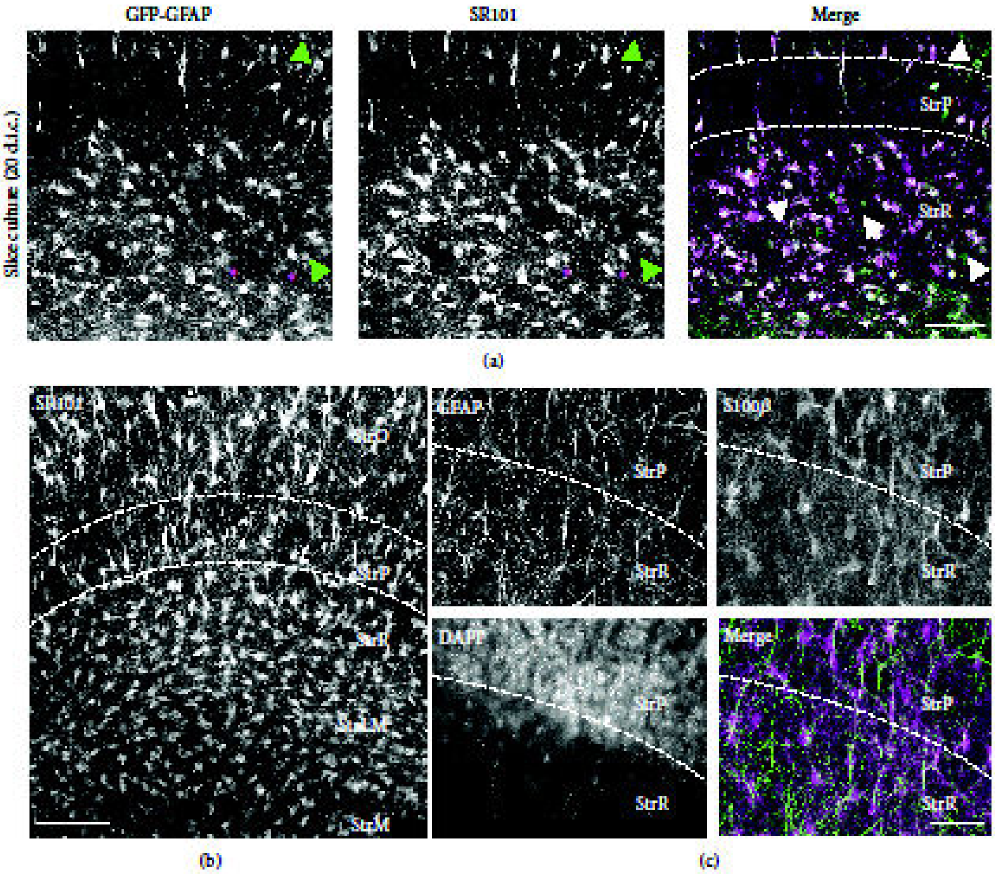

Figure 1: Astrocytes in organotypic hippocampal slice cultures. (a) Organotypic slice cultures at 20 days in culture (d.i.c.). Preparations were derived from animals in which GFP was expressed under control of the GFAP promoter. Shown is the expression of GFP (*left*), the labeling pattern of SR101 (*center*), and the corresponding merged image (GFAP: green, SR101: magenta). Asterisks point out SR101-labeled cells that do not express GFP; arrowheads point out GFP-positive, but SR101-negative cells. Images represent maximum intensity projections of 15 optical sections taken at 1 μm intervals. (b) SR101 fluorescence of an organotypic slice at 21 d.i.c. Image represents a stack of 20 optical sections taken at 1 μm intervals. (c) Immunohistochemical double staining for GFAP and S100β as well as DAPI fluorescence and merged image of the fluorescence of GFAP (green) and S100β (magenta) of part of the CA1 region encompassing the *strata pyramidale* and *radiatum* of an organotypic slice at 20 d.i.c. Note the radially oriented GFAP-positive fibers crossing the pyramidal cell layer. Images were taken at a wide-field microscope. ((a)–(c)): Dashed lines indicate the approximate boundaries of the *stratum pyramidale*. StrO, *stratum oriens*; StrP, *stratum pyramidale*; StrR, *stratum radiatum*; StrLM, *stratum lacunosum moleculare*; and StrM, *stratum moleculare*. Scale bars: (a) 50 μm, (b) 100 μm, and (c) 50 μm.

animals showed that the majority of GFAP-positive cells were also positive for S100β ($N = 12$; Figure 1(c)), a marker for mature astrocytes [46].

Taken together, the nearly complete overlap in the cellular staining pattern for the vital dye SR101 with the expression of GFP in GFP/GFAP mice, as well as the overlap in the immunofluorescence for GFAP and S100β in organotypic slices indicates that these markers are well suited to identify astrocytes in this preparation.

3.2. *Astrocyte Markers and Astrocyte Morphology following Mechanical Lesion.*

To induce astrogliosis in organotypic slice cultures, we used a scalpel blade and performed a scratch under semisterile conditions through the entire CA1 region oriented perpendicular to the *stratum pyramidale* (Figure 2(a)). 6-7 days after the lesion, a general enhancement of GFAP immunoreactivity was observed, indicating astrogliosis (Figure 2(b)). The greatest enhancement of GFAP immunoreactivity occurred within a distance of less than 100 μm along the lesion ($N = 26$; Figures 2(b) and 2(c)). Here, a dense meshwork of thick, GFAP-positive labels was present, indicative of the formation of a glial scar. Furthermore, the region close to the lesion site exhibited a discernible increase in S100β immunoreactivity ($N = 12$; Figure 2(c)). Both the prominent expressions of GFAP and S100β are characteristics of strongly reactive astrocytes, which represent the major

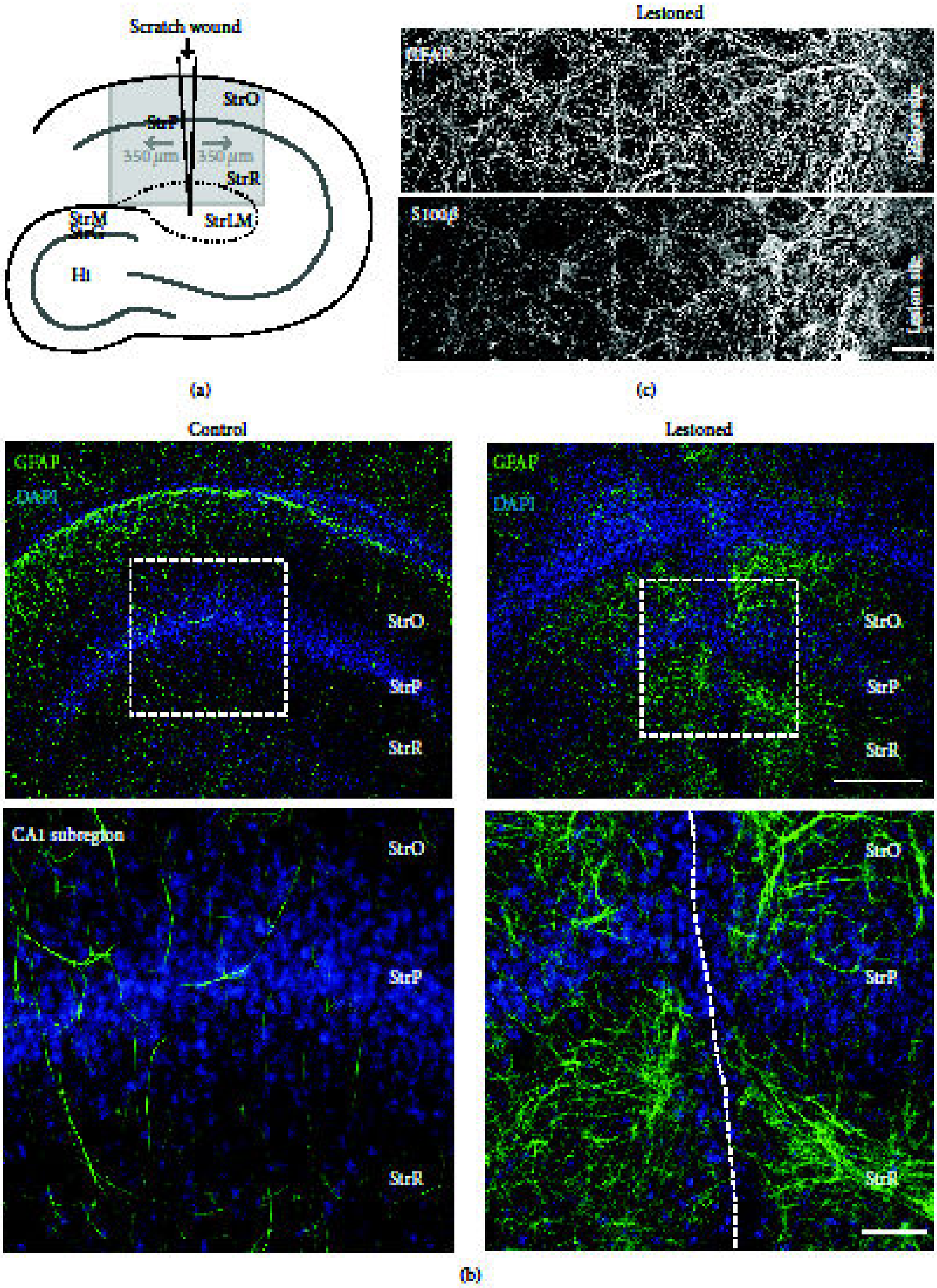

Figure 2: Lesion-induced reactive gliosis in organotypic slice cultures. (a) Schematic overview of the hippocampus indicating the position of the scratch wound. The box delineates the area primarily analyzed. (b) GFAP immunofluorescence and DAPI staining of the CA1 area in a control (*left*) and a lesioned (*right*) slice. The boxes indicate the areas enlarged below. The dashed line in the lower right indicates the lesion. (c) Double staining for GFAP (*top*) and S100β (*bottom*) adjacent to the lesion site. Note the gradual increase in GFAP and S100β expression towards the lesion. (b): widefield microscopy; (c): confocal microscopy (optical sections taken at 1 μm intervals). StrO, *stratum oriens*; StrP, *stratum pyramidale*; StrR, *stratum radiatum*; and StrLM, *stratum lacunosum moleculare*. Scale bars (b) 200 μm (*top*) and 50 μm (*bottom*); (c) 10 μm.

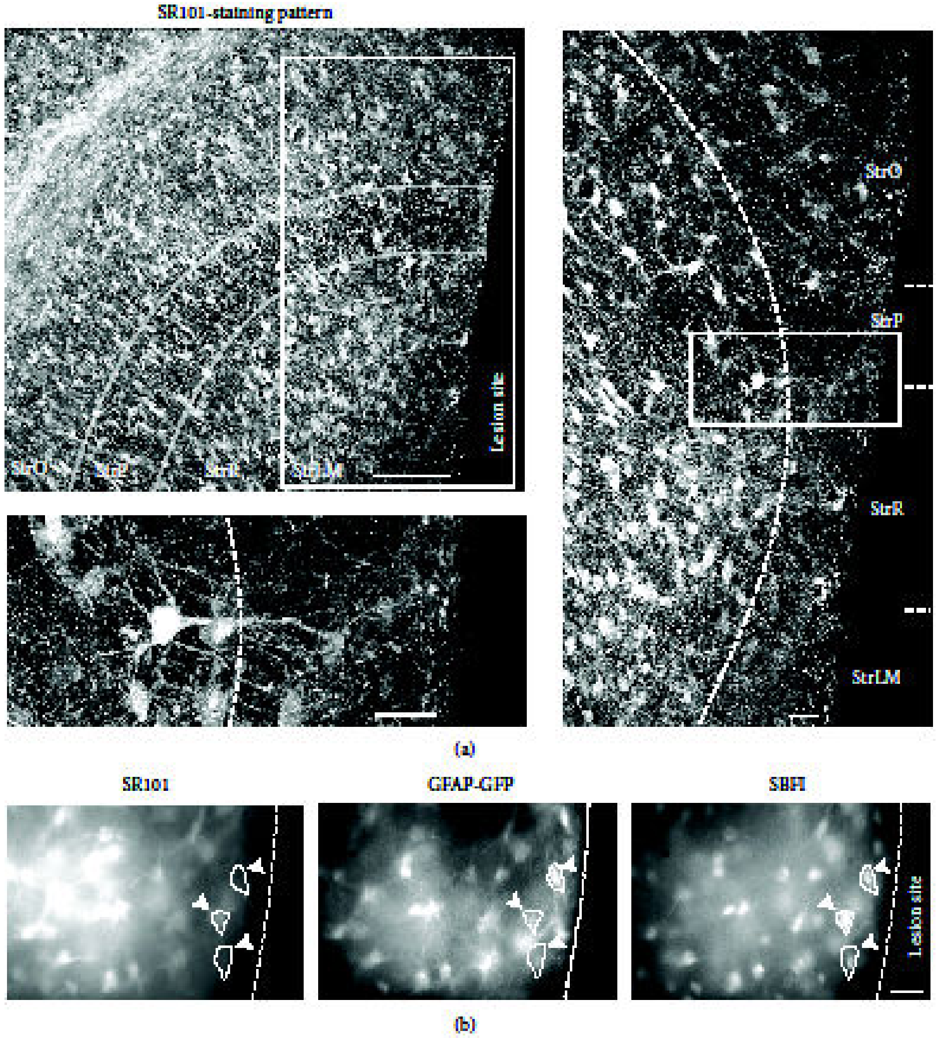

Figure 3: SR101 labeling in lesioned slices. (a) SR101 fluorescence in the CA1 area in a slice 7 days after lesion. The delineated area comprises the *stratum pyramidale*, and the box indicates the area enlarged on the right side. *Right*: SR101 fluorescence at the lesion site, illustrating that SR101 labeling is reduced along the lesion. The dotted line indicates the transition between the scar area and the adjacent, moderately reactive tissue. The boxed area is further enlarged at the bottom. (b) Image series obtained at a wide-field fluorescence microscope. The slice was prepared from a transgenic GFP/GFAP mouse, and the lesion site is indicated by the dotted line. *Left*: Image of SR101 fluorescence, *center*: GFP fluorescence indicating GFAP expression; and *right*: SBFI fluorescence. SR101 labeling is only weak in GFP/SBFI-positive cells in the scar region (see arrowheads). StrO, *stratum oriens*; StrP, *stratum pyramidale*; StrR, *stratum radiatum*, and; StrLM, *stratum lacunosum-moleculare*. Scale bars: 100 μm ((a), *upper left*) and 20 μm (other images).

cellular component of the glial scar forming after mechanical tissue injury [10]. More distal to the lesion (>100–350 μm), a less dramatic rearrangement of GFAP immunoreactivity was observed.

A clear difference in astrocyte properties between the scar region and its periphery was also seen following SR101 labeling. In the periphery of the scar (100–350 μm distance from the lesion), SR101 resulted in a reliable and bright cellular staining, similar to what had been observed in control, unlesioned slices ($N = 12$; Figure 3(a), cf. Figure 1). In contrast to this, cellular SR101 staining was detectable but only faint within a distance of less than 100 μm on both sides of the lesion (Figure 3(a); mean width of SR101-free area 111 ± 3 μm; $N = 5$). In slices from GFP/GFAP transgenic animals ($N = 5$; Figure 3(b)), GFAP-positive, weakly SR101-positive scar cells also stained with the sodium-sensitive fluorescence indicator SBFI-AM (acetoxymethyl ester of sodium binding benzofuran isophthalate; see below; $N = 3$), indicating that they were able to take up and de-esterify this dye (Figure 3(b)).

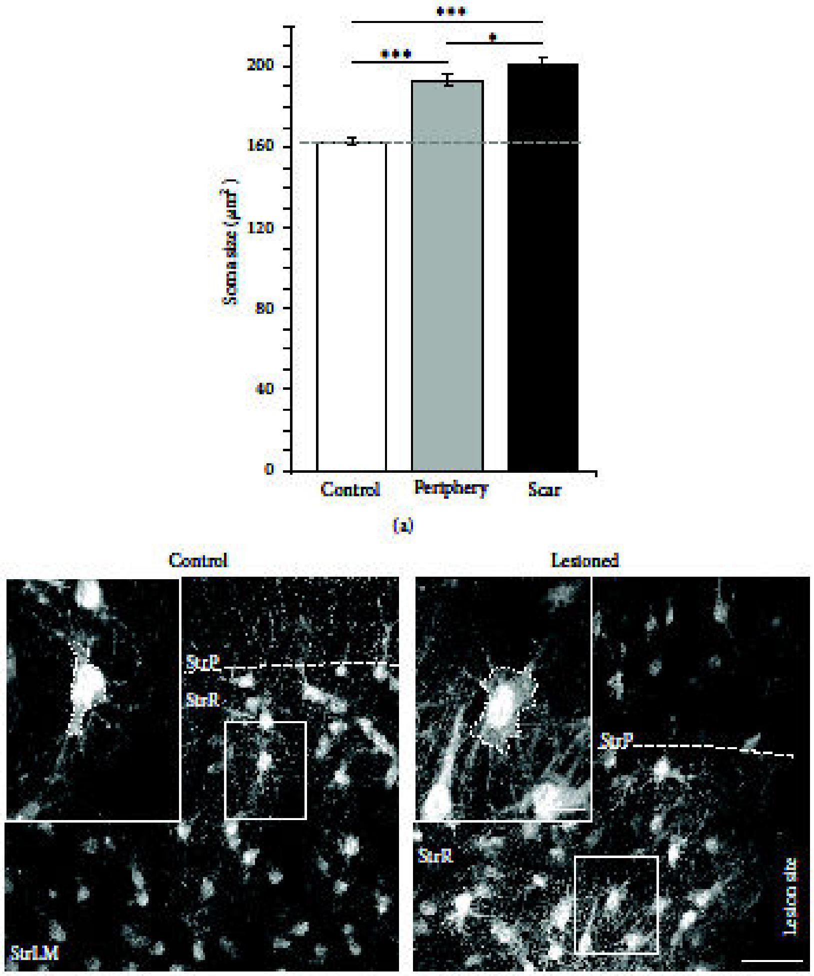

(a)

(b)

Figure 4: Lesion-induced changes in somatic area. (a) Quantification of somatic area based on GFAP/GFP fluorescence in control and lesioned slices. The soma size increased both in astrocytes in the scar region ("scar") and in astrocytes in the periphery of the lesion ("periphery"; $^{***}P < 0.001$; $^{*}P < 0.05$). (b) Confocal images of GFP fluorescence in cultured slices obtained from GFP/GFAP transgenic animals under control conditions (*left*) and subjected to a lesion (*right*). Cells surrounded by boxes are shown at higher magnification in the insets, and the dashed lines around the soma illustrate the areas which served to determine their size. StrP, *stratum pyramidale*; StrR, *stratum radiatum*; StrLM, *stratum lacunosum moleculare*; and scale bars: 40 μm and 10 μm (inset).

In addition to GFAP-positive cells, the scar region hosted microglial cells, identified by their vital staining with Texas Red-coupled lectin from *lycopersicon esculentum* (tomato lectin; $N = 4$; not shown). Tomato lectin-positive microglia, however, did not take up SBFI-AM ($N = 4$; not shown), confirming earlier reports that microglial cells do not incorporate AM-ester dyes *in situ* [47].

To further characterize reactive gliosis in response to the scratch wound, we determined the area of astrocyte somata in confocal images of the GFP fluorescence in control and lesioned slices obtained from GFP/GFAP transgenic animals. These measurements revealed that, compared to astrocytes in control slices, the soma area of astrocytes in the periphery of a lesion was increased by 18% and that of astrocytes in the scar region was increased by 24% (control: $163 \pm 2\,\mu m^2$; lesion periphery: $193 \pm 3\,\mu m^2$; scar tissue: $201 \pm 4\,\mu m^2$; $P < 0.001$; $n = 945$, 496, and 439 in 7 control and 9 lesioned slices; Figures 4(a) and 4(b)). Thus, astrocytes show a second hallmark of reactive gliosis after lesion, namely, a hypertrophy of their cell bodies, which is observed both in the scar tissue as well as in the periphery of the lesion.

Taken together, these data show that 6-7 days after the mechanical lesion, a glial scar has formed along the lesion site. This scar encompasses strongly activated astrocytes, characterized by a robust increase in GFAP and S100β expression. These proximal reactive astrocytes, located within a distance of less than 100 μm from the lesion, exhibit long GFAP-positive processes, have significantly swollen somata, and only weakly stain with SR101. Astrocytes in the periphery of the scar (100–350 μm from the lesion) display swollen cell bodies as well, but show only moderate upregulation of GFAP and maintain their ability to efficiently take up SR101.

3.3. *Expression Levels and Spatial Distribution of GLT-1 and GLAST.*

To determine the spatial distribution of the glutamate transporters GLAST and GLT-1 in organotypic slices and changes therein in response to the lesion, immunohistochemistry was employed. In control slices, GLAST ($N = 13$; Figure 5(a)) as well as GLT-1 immunoreactivity ($N = 11$; Figure 5(b)) appeared as punctate labeling throughout the entire CA1 area. The staining patterns for both transporters in the tissue slice cultures were thus similar to those reported from acute tissue slice preparations of the hippocampus [36, 48, 49].

The relatively homogeneous distribution of immunoreactivity throughout the preparation found in control slice cultures was abandoned following a lesion. Here, distinct accumulations of GLAST ($N = 17$; Figure 5(a)) and GLT-1 immunoreactivity ($N = 12$; Figure 5(b)) were found in the scar region. In both cases, these preferentially colocalized with thick GFAP-positive bundles running in parallel to the lesion (Figure 5). Apart from the marked accumulation of GLAST reactivity in parallel to the scar, GLAST immunoreactivity appeared generally increased in some lesioned slice preparations (Figure 5(a)) but unaltered in others both within the scar as well as in its periphery. For GLT-1, a decline in the intensity of immunoreactivity was observed with increasing distance from the lesion (Figure 5(b)).

In summary, these results reveal distinct alterations in the immunoreactivity of GLAST and GLT-1 following a mechanical lesion. In the scar region, clusters of GLT-1 and GLAST immunoreactivity are present, primarily colocalized with strongly GFAP-positive fibers. Apart from these distinct clusters, GLT-1 immunoreactivity appears to decline with distance from the scar, whereas GLAST immunoreactivity seems largely uniform throughout the preparation.

3.4. *Sodium Transients Induced by Activation of Glutamate Uptake.*

Glutamate uptake is accompanied by the inward flux of sodium, resulting in increase in the intracellular sodium concentration of astrocytes. To monitor its function, we assayed sodium increases induced by D-aspartate, a nonmetabolized substrate of sodium-dependent glutamate uptake which is also transported [1] in astrocytes in the *stratum radiatum* of organotypic slices. To this end, SR101-stained slices were additionally loaded with the sodium-sensitive fluorophore SBFI-AM (Figure 6(a), cf. Figure 3(b)). *In situ* calibrations of the SBFI fluorescence revealed a linear increase in its fluorescence ratio at intracellular sodium concentrations between 10 and 40 mM ($n = 107$; Figure 6(b)) as reported before [33].

Repetitive pressure application of D-aspartate for 500 ms induced reliable increases in the intracellular sodium concentration in astrocytes, indicating activation of sodium-dependent glutamate uptake ($n = 488$; Figure 6(c)). The experiments were performed in the presence of the sodium-channel blocker TTX (tetrodotoxin, 0.5 μM) to suppress action potential generation. The amplitude of D-aspartate-induced sodium increases was dependent on the concentration applied (Figure 6(c)) and saturated at about 2 mM ($n = 19$; Figure 6(d)), as reported before for mouse cortical astrocytes in culture [50]. At a concentration of 1 mM, the amplitude of D-aspartate-induced sodium transients was near maximum and amounted to 3.8 ± 0.2 mM ($n = 161$; Figures 6(c) and 6(d)), a value comparable to that in astrocytes in acute slices obtained in our lab [33].

To probe for changes in glutamate uptake, we compared sodium signals induced by 1 mM D-aspartate between control and lesioned slices (Figure 7). In lesioned slices, astrocytes located in the periphery of the lesion (100–350 μm distance) responded with a sodium transient to application of 1 mM D-aspartate (see cell 2 in Figures 7(a) and 7(b)). The amplitude of D-aspartate-induced sodium signals in cells in the lesion periphery was similar to that observed in control slices (3.8 ± 0.3 mM; $n = 111$; see cell 1 in Figures 7(a), 7(b), and 7(c)). Application of D-aspartate also evoked sodium transients in weakly SR101-positive, SBFI-filled astrocytes located in the glial scar area (<100 μm from the lesion; see cells 3–5 in Figures 7(a) and 7(b)). These cells, however, displayed significantly smaller peak amplitudes (1.6 ± 0.21 mM, $n = 26$; $P < 0.001$; Figures 7(b) and 7(c)) than astrocytes in the periphery and in control slices.

The kinetics of D-aspartate-induced sodium transients differed between all three groups. This was true for the slope of the sodium increase (10%–90% change), which was significantly reduced in astrocytes from lesioned slices versus astrocytes from control slices (0.9 ± 0.05 mM/s in control versus 0.6 ± 0.06 mM/s in the periphery and 0.2 ± 0.04 mM/s in the scar region; $n = 161$, 111, and 26, resp.; $P < 0.001$; Figures 7(b) and 7(c)). In addition, the decay back to baseline was significantly slower following lesion (Figures 7(b) and 7(c)). The time needed for the signal to decay by 67% was approximately doubled (decay time τ was 44 ± 2 s in control, $\tau = 81 \pm 4$ s in periphery of the lesion, and $\tau = 95 \pm 10$ s in scar cells; Figures 7(b) and 7(c)).

These results show that mechanical injury results in distinct alterations in the kinetics and/or amplitudes of D-aspartate-induced intracellular sodium transients in reactive astrocytes, depending on their distance to the lesion.

4. Discussion

Our results show that within 6-7 days after setting a scratch wound in organotypic hippocampal slices, a dense glial scar had formed along the lesion site. Up to approximately 100 μm distance from the lesion, the scar tissue was characterized by a substantial elevation of GFAP expression, a pronounced cellular hypertrophy, and reduced uptake of SR101 by astrocytes.

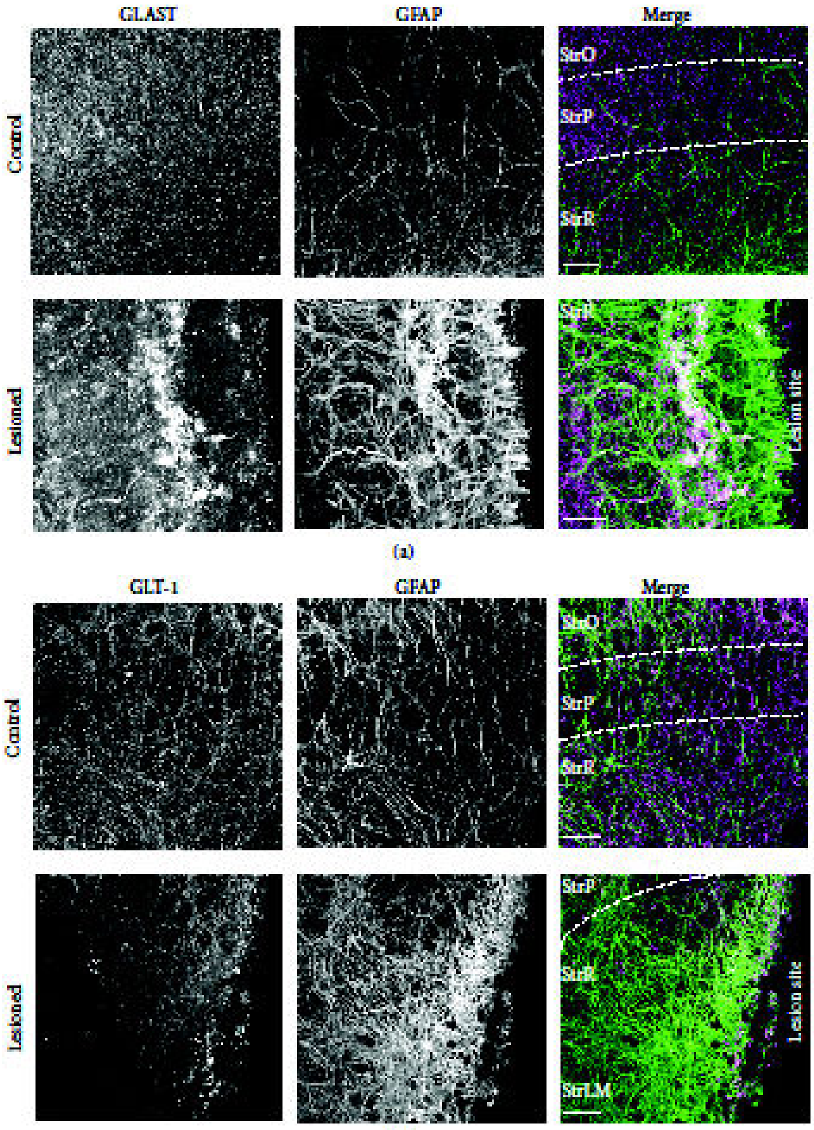

(a)

(b)

Figure 5: GLAST and GLT-1 immunoreactivity after mechanical injury. (a) Fluorescence images of immunohistochemical stainings detecting the glutamate transporters GLAST (*left*), GFAP (*center*) as counterstaining, and the corresponding merged image (GFAP: green, GLAST: magenta) in control (*top row*) and lesioned slice cultures (*bottom row*). (b) GLT-1 (*left*), GFAP (*center*) double labeling of a control (*top row*) and a mechanically lesioned slice (*bottom row*). The corresponding merge (GFAP: green, GLT-1: magenta) is found on the right. Note that after lesion, glutamate transporter immunoreactive clusters are accumulated in the direct vicinity of the lesion site (arrowheads). GFAP, glial fibrillary acidic protein; GLAST, glutamate aspartate transporter; GLT-1, glutamate-transporter-1; StrO, *stratum oriens*; StrP, *stratum pyramidale*; StrR, *stratum radiatum*; StrLM, *stratum lacunosum-moleculare*; and scale bars: (a) 20 μm, (b) 40 μm.

While prominent clusters of GLAST and GLT-1 immunoreactivity were observed along GFAP-positive structures in scar cells, D-aspartate-induced intracellular sodium signals were strongly dampened, indicating a significant reduction in glutamate uptake capacity close to the lesion. In the periphery of the lesion (100–350 μm), astrocytes showed less pronounced reactivity, maintained their ability to efficiently take up SR101, and displayed only minor changes in glutamate transporter immunoreactivity and function. Thus, depending on their distance from the lesion, astrocytes showed different grades of reactivity and displayed discrete changes in glutamate transporter immunoreactivity and uptake capacity.

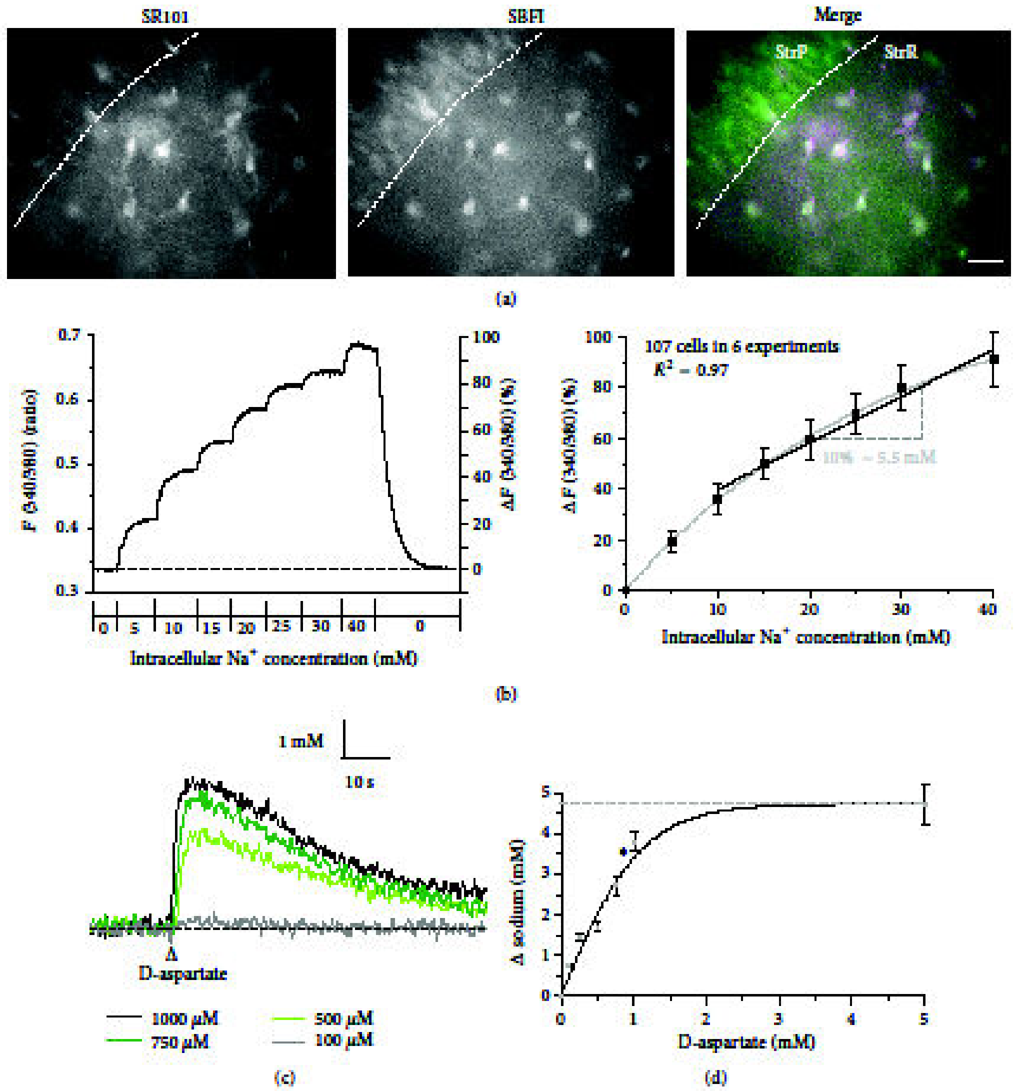

Figure 6: Sodium changes induced by activation of glutamate uptake. (a) Staining of astrocytes by colabeling with SR101 and SBFI. *Left*: epifluorescence image of the CA1-area of an SR101-loaded organotypic slice. *Center*: SBFI fluorescence taken from the same area. *Right*: overlay. SBFI-loaded, SR101-positive astrocytes appear in white (arrowheads). StrP, *stratum pyramidale*; StrR, *stratum radiatum*; scale bar: 20 μm. (b) *Left*: calibration of SBFI fluorescence in an astrocyte. Depicted is the change in intracellular SBFI fluorescence ratio in the calibration solutions containing ionophores and in response to stepwise changes in the sodium concentration. *Right*: mean values ± S.E.M. of the normalized changes in SBFI fluorescence at different sodium concentrations. The black line represents a linear fit of the data points between 10 and 40 mM sodium, illustrating that a 10% change in SBFI fluorescence represents a change in the sodium concentration by 5.5 mM. (c) Sodium transients in a single astrocyte induced by 500 ms applications of D-aspartate at different concentrations. (d) Mean values ± S. E. M. ($n = 19$) of the peak amplitude of sodium transients at different concentrations of D-aspartate. The curve represents a sigmoidal fit of the data.

4.1. Characteristics of Lesion-Induced Reactive Gliosis in Organotypic Cultures. Organotypic tissue slice cultures of the hippocampus represent a well-established model system, in which the basic tissue architecture is maintained, but which still hosts the major advantages of cell cultures such as good accessibility and control of experimental conditions. They have been used extensively for the analysis of neuronal properties and developing neuronal networks [28, 51, 52] or the study of excitotoxic neuronal damage (e.g., [53, 54]). Recent studies also demonstrated that basic morphological characteristics of astrocytes and the typical glia-synapse organization are well preserved in organotypic slice cultures (e.g., [44, 45, 55, 56]). In addition, we found a nearly complete overlap of SR101 staining with the expression of GFP in slice

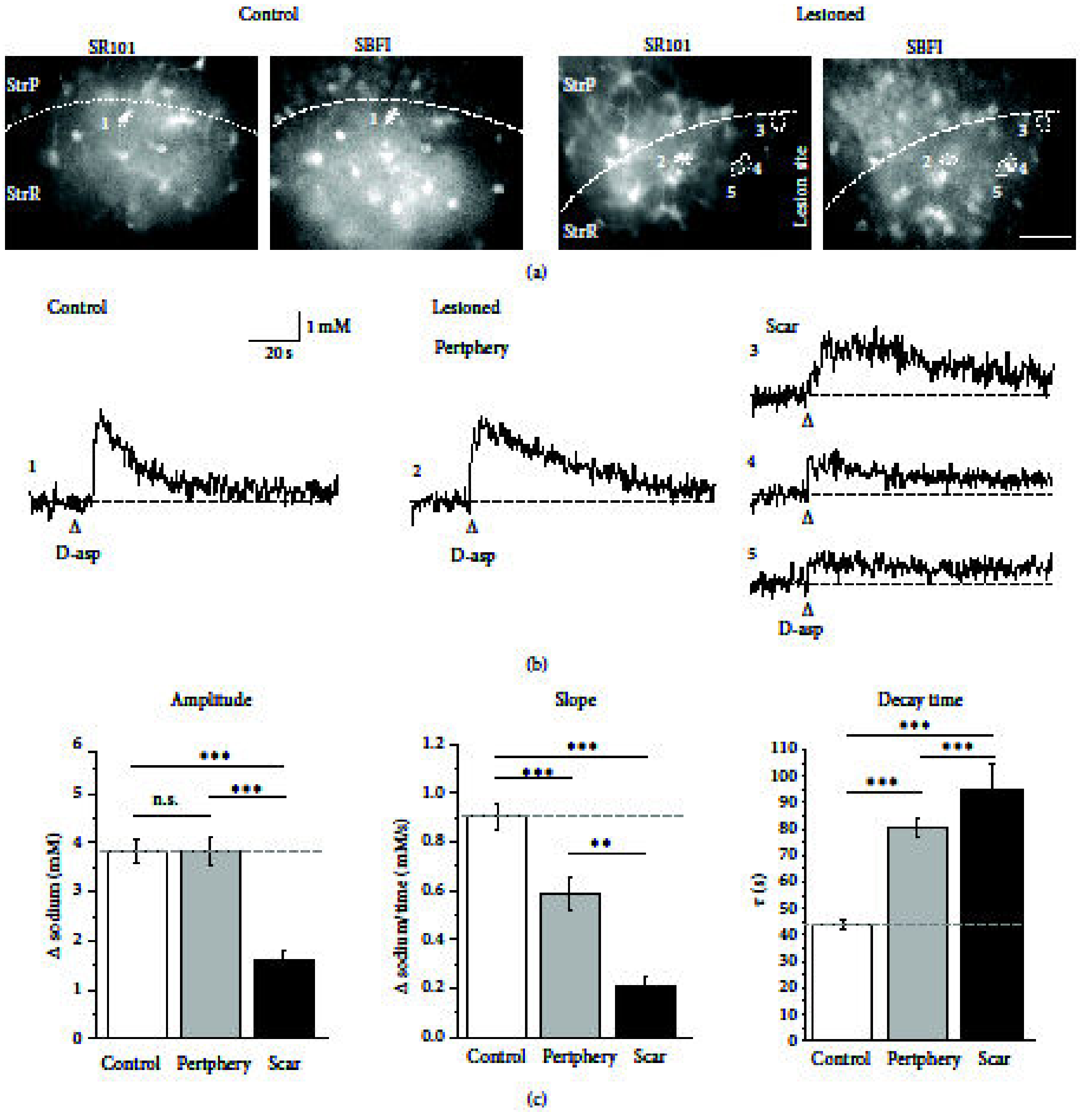

FIGURE 7: D-aspartate-induced astrocyte sodium transients following lesion. (a) CA1 area of a control (*left*) and a lesioned (*right*) slice preparation. Shown are epifluorescence images of SR101 and SBFI fluorescences. Circled areas and numbers indicate the regions of interest analyzed in the experiment depicted in (b). StrP, *stratum pyramidale*; StrR, *stratum radiatum*; and scale bar: 40 μm. (b) Sodium transients induced by pressure application of 1 mM D-aspartate (D-asp) for 500 ms in the different cells in the control and lesioned slice as indicated in (a). (c) Histograms showing mean values ± S. E. M. of the peak amplitude (*left*), slope (*center*), and decay time (*right*) of D-aspartate-induced sodium transients in astrocytes in control slices ($n = 161$) as well as in cells in the scar region and its periphery ($n = 111$ and $n = 26$, resp.). $^{**}P < 0.01$; $^{***}P < 0.001$. StrP, *stratum pyramidale*; StrR, *stratum radiatum*; and scale bar: 40 μm.

cultures obtained from GFP/GFAP mice, demonstrating that SR101 is well suited to identify astrocytes in this preparation as described before for acute tissue slices and *in vivo* [29, 30].

Performing a scratch through the CA1 region of organotypic slices resulted in the formation of a glial scar along the lesion site, as judged by the prominent increase in expression of GFAP and S100β. In addition, astrocyte cell bodies showed a significant hypertrophy. Furthermore, astrocytes in the periphery of the scar (100–350 μm from the lesion) showed mild to moderate reactivity, displaying swollen cell bodies, and only moderate upregulation of GFAP. These changes are hallmarks of reactive gliosis observed after tissue injury [10, 13, 57]. Generally, the degree of injury and the distance of the astrocytes from the site of injury define the degree of their activation [11, 13].

Our study also revealed that strongly reactive astrocytes in the scar region only weakly stain with SR101. The reduced ability of strongly activated astrocytes to accumulate SR101 indicates that strong glial activation is accompanied by a downregulation of the organic anion transporter responsible for uptake of SR101. This is reminiscent of immature astrocytes in the early postnatal hippocampus, which are SR101-negative [30] and in line with a wealth of experimental evidence suggesting that reactive gliosis represents a process comprising a dedifferentiation of astrocytes [17].

4.2. Changes in Glutamate Transporter Expression following Lesion. Glutamate uptake in the hippocampus is mainly achieved by the glial glutamate transporters GLT-1 and GLAST [1, 2]. A central factor in many brain pathologies, including traumatic brain injury, is an increase in extracellular glutamate and excitotoxicity; it has been suggested that a change in the expression levels of glial glutamate transporters might play a critical role in the failure of glutamate clearance [6, 58–60]. Earlier work has found an overall downregulation of protein levels of both GLAST and GLT-1 following astrocyte activation [22–27], indicating that this is causal to the elevation of extracellular glutamate. In contrast to this notion, other studies reported increased glutamate transport capacity of reactive astrocytes and suggested a protective influence [61, 62].

To visualize possible differences in the spatial expression profile of GLT-1 and GLAST in strongly reactive astrocytes along the scar as compared to moderately reactive astrocytes in its periphery, we performed immunohistochemical stainings. These revealed an accumulation of GLT-1 and GLAST immunoreactivity along thick GFAP-positive fibers, which was particularly pronounced for GLAST. Besides these clusters, overall GLAST immunoreactivity seemed unaltered as compared to unlesioned slices, whereas GLT-1 immunoreactivity seemed weaker and declined with increasing distance from the scar. Clustering of glutamate transporters has been described by several reports [48, 63, 64]. In developing hippocampal astrocytes, cluster formation was preferentially found in branches opposed to synapses and was increased with increased neuronal activity, indicating that it is necessary to cope with synaptic release of glutamate [36]. Along the same lines, it was observed that sustained astroglial activation by ciliary neurotrophic factor (CNTF) in the rat striatum induced a concentration of GLAST and GLT-1 into raft microdomains and improved glutamate clearance, indicating that cluster formation increased the cellular capacity for glutamate uptake [61]. However, another study found glutamate-induced clustering of GLT-1 that induced its endocytosis and intracellular trafficking without changing the total expression levels as detected by western blots, arguing for a decrease in functional glial glutamate uptake capacity [49]. In the present study, antibodies against GLT-1 and GLAST were employed for immunohistochemistry after permeabilization of the plasma membrane. The clusters of GLAST and GLT-1 along GFAP-positive fibers in the scar region (as GLAST and GLT-1 immunoreactivity in general) could thus represent glutamate transporters in the plasma membrane or in intracellular compartments or both. Consequently, the observed clustering does not allow a prediction about possible functional changes in glutamate uptake.

4.3. Lesion-Induced Changes in Functional Glutamate Uptake Capacity. We probed for the functional activation of glutamate transport by application of the transportable agonist D-aspartate, which results in an increase in the intracellular sodium concentration of astrocytes [8, 9]. The amplitudes of D-aspartate-induced sodium transients in astrocytes in control organotypic slices were similar to those reported from astrocytes in acute slices obtained in our lab [33], indicating similar cellular glutamate transport capacity in both preparations.

Following a lesion, D-aspartate-induced intracellular sodium signals were clearly dampened in scar cells. Moreover, the slope of the increase in sodium was significantly reduced, and the decay back to baseline was slowed. Because D-aspartate was applied at nearly saturating concentration, the reduction in peak amplitudes suggests a reduction in functional glutamate uptake capacity in cells close to the lesion, which might be mediated by a decrease in the overall number of glutamate transporters available at the plasma membrane. In contrast, the alteration in the kinetics of the D-aspartate-induced sodium signals can be explained by the cellular hypertrophy that was observed in reactive astrocytes. At an equal transport-mediated sodium influx across the membrane, the slope of resulting changes in the sodium concentration will be decreased in cells with a larger volume.

Furthermore, the decay of intracellular sodium transients back to baseline is mainly governed by the activity of the Na^+/K^+-ATPase as well as by diffusion [8]. The slower recovery is in line with earlier studies reporting a downregulation of the sodium pump following reactive gliosis [65, 66]. Moreover, sodium is not buffered in the cell and travels solely by means of diffusion in the cytoplasm. Hindered diffusion, resulting from increased cytoplasmic protein content or impaired gap junction coupling which both occur upon astrocytic activation, might thus also partially contribute to delayed sodium recovery [12, 34, 67].

In contrast to scar cells, the amplitude of D-aspartate-induced intracellular sodium signals was not significantly altered in moderately activated astrocytes in the periphery of the lesion, indicating that the overall number of functional glutamate transporters was not significantly altered. Because these cells showed hypertrophy as well, the slowed kinetics of the sodium transients are in line with an increased cellular volume as well as a possible downregulation of Na^+/K^+-ATPase and/or a slowed diffusion as argued above.

Taken together, our results indicate a significant reduction in glutamate uptake capacity in strongly activated astrocytes in the scar region. Thus, the prominent clustering of GLAST and GLT-1 immunoreactivity along GFAP-positive structures close to the lesion is likely to reflect a loss of glutamate transporters from the plasma membrane upon transporter internalization as reported by Nakagawa et al. [49]. The authors of the latter study speculated that large and prolonged increases in glutamate concentrations are necessary to induce such cluster formation and endocytosis in the tissue, as they would possibly only occur under pathological conditions. Indeed, ambient glutamate concentrations were shown to be significantly increased after traumatic brain injury [68–70]. Along these lines, it can be assumed that in our model system, extracellular glutamate concentrations rose less severely in the periphery of the lesion, preventing a comparable clustering and loss of functional glutamate transport activity in moderately activated astrocytes.

5. Conclusions

Our results show complex changes in glutamate transporter expression and function during astrocyte activation following mechanical injury. They confirm that the degree of astrocyte activation depends on the distance from the insult and comprises different endpoints regarding cellular morphology and physiology. Furthermore, our results highlight that astrocytes which show different grades of reactivity also display discrete changes in glutamate transporter expression and function. While immunohistochemistry revealed a prominent clustering of GLT-1 and GLAST immunoreactivity in the scar region, our functional assay clearly showed that glutamate uptake capacity is strongly reduced in scar cells, while it is largely maintained in moderately activated astrocytes in the periphery. Thus, mild-to-moderate astrogliosis in the periphery of a mechanical lesion does not necessarily seem to be accompanied by a significant change in glial glutamate uptake capacity. At the glial scar itself, in strongly reactive astrocytes, a clustering of glutamate transporters is observed that apparently goes along with a severe functional reduction in astroglial glutamate uptake, which may contribute to glutamate-mediated excitotoxicity in this region.

Conflict of Interests

The authors of the paper declare that they do not have any direct financial relation with the commercial identities mentioned in the paper that might lead to a conflict of interests.

Acknowledgments

This study was supported by the Deutsche Forschungsgemeinschaft (DFG Ro2327/4-3). The authors thank Simone Durry and Claudia Roderigo for expert technical help.

References

[1] N. C. Danbolt, "Glutamate uptake," *Progress in Neurobiology*, vol. 65, no. 1, pp. 1–105, 2001.

[2] A. V. Tzingounis and J. I. Wadiche, "Glutamate transporters: confining runaway excitation by shaping synaptic transmission," *Nature Reviews Neuroscience*, vol. 8, no. 12, pp. 935–947, 2007.

[3] D. E. Bergles, J. S. Diamond, and C. E. Jahr, "Clearance of glutamate inside the synapse and beyond," *Current Opinion in Neurobiology*, vol. 9, no. 3, pp. 293–298, 1999.

[4] C. M. Anderson and R. A. Swanson, "Astrocyte glutamate transport: review of properties, regulation, and physiological functions," *Glia*, vol. 32, no. 1, pp. 1–14, 2000.

[5] P. Marcaggi and D. Attwell, "Role of glial amino acid transporters in synaptic transmission and brain energetics," *Glia*, vol. 47, no. 3, pp. 217–225, 2004.

[6] N. J. Maragakis and J. D. Rothstein, "Glutamate transporters: animal models to neurologic disease," *Neurobiology of Disease*, vol. 15, no. 3, pp. 461–473, 2004.

[7] G. Gegelashvili and A. Schousboe, "Cellular distribution and kinetic properties of high-affinity glutamate transporters," *Brain Research Bulletin*, vol. 45, no. 3, pp. 233–238, 1998.

[8] J. W. Deitmer and C. R. Rose, "Ion changes and signalling in perisynaptic glia," *Brain Research Reviews*, vol. 63, no. 1-2, pp. 113–129, 2010.

[9] S. Kirischuk, V. Parpura, and A. Verkhratsky, "Sodium dynamics: another key to astroglial excitability?" *Trends in Neurosciences*, vol. 35, no. 8, pp. 497–506, 2012.

[10] M. V. Sofroniew, "Molecular dissection of reactive astrogliosis and glial scar formation," *Trends in Neurosciences*, vol. 32, no. 12, pp. 638–647, 2009.

[11] J. L. Ridet, S. K. Malhotra, A. Privat, and F. H. Gage, "Reactive astrocytes: cellular and molecular cues to biological function," *Trends in Neurosciences*, vol. 20, no. 12, pp. 570–577, 1997.

[12] J. Middeldorp and E. M. Hol, "GFAP in health and disease," *Progress in Neurobiology*, vol. 93, no. 3, pp. 421–443, 2011.

[13] M. Pekny and M. Nilsson, "Astrocyte activation and reactive gliosis," *Glia*, vol. 50, no. 4, pp. 427–434, 2005.

[14] A. Bordey, S. A. Lyons, J. J. Hablitz, and H. Sontheimer, "Electrophysiological characteristics of reactive astrocytes in experimental cortical dysplasia," *Journal of Neurophysiology*, vol. 85, no. 4, pp. 1719–1731, 2001.

[15] R. Jabs, G. Seifert, and C. Steinhäuser, "Astrocytic function and its alteration in the epileptic brain," *Epilepsia*, vol. 49, supplement 2, pp. 3–12, 2008.

[16] A. Buffo, I. Rite, P. Tripathi et al., "Origin and progeny of reactive gliosis: a source of multipotent cells in the injured brain," *Proceedings of the National Academy of Sciences of the United States of America*, vol. 105, no. 9, pp. 3581–3586, 2008.

[17] S. Robel, B. Berninger, and M. Götz, "The stem cell potential of glia: lessons from reactive gliosis," *Nature Reviews Neuroscience*, vol. 12, no. 2, pp. 88–104, 2011.

[18] H. Kawano, J. Kimura-Kuroda, Y. Komuta et al., "Role of the lesion scar in the response to damage and repair of the central nervous system," *Cell and Tissue Research*, vol. 349, no. 1, pp. 169–180, 2012.

[19] G. Yiu and Z. He, "Glial inhibition of CNS axon regeneration," *Nature Reviews Neuroscience*, vol. 7, no. 8, pp. 617–627, 2006.

[20] M. T. Fitch and J. Silver, "CNS injury, glial scars, and inflammation: inhibitory extracellular matrices and regeneration failure," *Experimental Neurology*, vol. 209, no. 2, pp. 294–301, 2008.

[21] L. Li, A. Lundkvist, D. Andersson et al., "Protective role of reactive astrocytes in brain ischemia," *Journal of Cerebral Blood Flow & Metabolism*, vol. 28, no. 3, pp. 468–481, 2008.

[22] F. K. H. van Landeghem, T. Weiss, M. Oehmichen, and A. Von Deimling, "Decreased expression of glutamate transporters in astrocytes after human traumatic brain injury," *Journal of Neurotrauma*, vol. 23, no. 10, pp. 1518–1528, 2006.

[23] V. L. Raghavendra Rao, M. K. Başkaya, A. Doğan, J. D. Rothstein, and R. J. Dempsey, "Traumatic brain injury downregulates glial glutamate transporter (GLT- 1 and GLAST) proteins in rat brain," *Journal of Neurochemistry*, vol. 70, no. 5, pp. 2020–2027, 1998.

[24] J.-C. Chen, H. Hsu-Chou, J.-L. Lu et al., "Down-regulation of the glial glutamate transporter GLT-1 in rat hippocampus and striatum and its modulation by a group III metabotropic glutamate receptor antagonist following transient global forebrain ischemia," *Neuropharmacology*, vol. 49, no. 5, pp. 703–714, 2005.

[25] S. D. Ginsberg, L. J. Martin, and J. D. Rothstein, "Regional deafferentation down-regulates subtypes of glutamate transporter proteins," *Journal of Neurochemistry*, vol. 65, no. 6, pp. 2800–2803, 1995.

[26] J. E. Springer, R. D. Azbill, R. J. Mark, J. G. Begley, G. Waeg, and M. P. Mattson, "4-Hydroxynonenal, a lipid peroxidation product, rapidly accumulates following traumatic spinal cord injury and inhibits glutamate uptake," *Journal of Neurochemistry*, vol. 68, no. 6, pp. 2469–2476, 1997.

[27] M. B. Moretto, N. S. Arteni, D. Lavinsky et al., "Hypoxic-ischemic insult decreases glutamate uptake by hippocampal slices from neonatal rats: Prevention by guanosine," *Experimental Neurology*, vol. 195, no. 2, pp. 400–406, 2005.

[28] L. Stoppini, P.-A. Buchs, and D. Muller, "A simple method for organotypic cultures of nervous tissue," *Journal of Neuroscience Methods*, vol. 37, no. 2, pp. 173–182, 1991.

[29] A. Nimmerjahn, F. Kirchhoff, J. N. D. Kerr, and F. Helmchen, "Sulforhodamine 101 as a specific marker of astroglia in the neocortex in vivo," *Nat Methods*, vol. 1, no. 1, pp. 31–37, 2004.

[30] K. W. Kafitz, S. D. Meier, J. Stephan, and C. R. Rose, "Developmental profile and properties of sulforhodamine 101-Labeled glial cells in acute brain slices of rat hippocampus," *Journal of Neuroscience Methods*, vol. 169, no. 1, pp. 84–92, 2008.

[31] C. Schnell, Y. Hagos, and S. Hulsmann, "Active sulforhodamine 101 uptake into hippocampal astrocytes," *PLoS One*, vol. 7, no. 11, Article ID e49398, 2012.

[32] S. D. Meier, Y. Kovalchuk, and C. R. Rose, "Properties of the new fluorescent Na$^+$ indicator CoroNa Green: comparison with SBFI and confocal Na$^+$ imaging," *Journal of Neuroscience Methods*, vol. 155, no. 2, pp. 251–259, 2006.

[33] J. Langer and C. R. Rose, "Synaptically induced sodium signals in hippocampal astrocytes in situ," *Journal of Physiology*, vol. 587, part 24, pp. 5859–5877, 2009.

[34] J. Langer, J. Stephan, M. Theis, and C. R. Rose, "Gap junctions mediate intercellular spread of sodium between hippocampal astrocytes in situ," *Glia*, vol. 60, no. 2, pp. 239–252, 2012.

[35] C. R. Rose and B. R. Ransom, "Intracellular sodium homeostasis in rat hippocampal astrocytes," *Journal of Physiology*, vol. 491, part 2, no. 2, pp. 291–305, 1996.

[36] A. M. Benediktsson, G. S. Marrs, J. C. Tu et al., "Neuronal activity regulates glutamate transporter dynamics in developing astrocytes," *Glia*, vol. 60, no. 2, pp. 175–188, 2012.

[37] M. Zhou, G. P. Schools, and H. K. Kimelberg, "Development of GLAST(+) astrocytes and NG2(+) glia in rat hippocampus CA1: mature astrocytes are electrophysiologically passive," *Journal of Neurophysiology*, vol. 95, no. 1, pp. 134–143, 2006.

[38] I. Suárez, G. Bodega, and B. Fernández, "Modulation of glutamate transporters (GLAST, GLT-1 and EAAC1) in the rat cerebellum following portocaval anastomosis," *Brain Research*, vol. 859, no. 2, pp. 293–302, 2000.

[39] X. Zhu, D. E. Bergles, and A. Nishiyama, "NG2 cells generate both oligodendrocytes and gray matter astrocytes," *Development*, vol. 135, no. 1, pp. 145–157, 2008.

[40] B. Brunne, S. Zhao, A. Derouiche et al., "Origin, maturation, and astroglial transformation of secondary radial glial cells in the developing dentate gyrus," *Glia*, vol. 58, no. 13, pp. 1553–1569, 2010.

[41] Y. Wu, A.-Q. Zhang, and D. T. Yew, "Age related changes of various markers of astrocytes in senescence-accelerated mice hippocampus," *Neurochemistry International*, vol. 46, no. 7, pp. 565–574, 2005.

[42] S. Magavi, D. Friedmann, G. Banks, A. Stolfi, and C. Lois, "Coincident generation of pyramidal neurons and protoplasmic astrocytes in neocortical columns," *Journal of Neuroscience*, vol. 32, no. 14, pp. 4762–4772, 2012.

[43] M. Olabarria, H. N. Noristani, A. Verkhratsky, and J. J. Rodriguez, "Concomitant astroglial atrophy and astrogliosis in a triple transgenic animal model of Alzheimer's disease," *Glia*, vol. 58, no. 7, pp. 831–838, 2010.

[44] A. M. Benediktsson, S. J. Schachtele, S. H. Green, and M. E. Dailey, "Ballistic labeling and dynamic imaging of astrocytes in organotypic hippocampal slice cultures," *Journal of Neuroscience Methods*, vol. 141, no. 1, pp. 41–53, 2005.

[45] I. Lushnikova, G. Skibo, D. Muller, and I. Nikonenko, "Synaptic potentiation induces increased glial coverage of excitatory synapses in CA1 hippocampus," *Hippocampus*, vol. 19, no. 8, pp. 753–762, 2009.

[46] E. Raponi, F. Agenes, C. Delphin et al., "S100B expression defines a state in which GFAP-expressing cells lose their neural stem cell potential and acquire a more mature developmental stage," *Glia*, vol. 55, no. 2, pp. 165–177, 2007.

[47] C. G. Schipke, C. Boucsein, C. Ohlemeyer, F. Kirchhoff, and H. Kettenmann, "Astrocyte Ca^{2+} waves trigger responses in microglial cells in brain slices," *The FASEB Journal*, vol. 16, no. 2, pp. 255–257, 2002.

[48] J. Zhou and M. L. Sutherland, "Glutamate transporter cluster formation in astrocytic processes regulates glutamate uptake activity," *Journal of Neuroscience*, vol. 24, no. 28, pp. 6301–6306, 2004.

[49] T. Nakagawa, Y. Otsubo, Y. Yatani, H. Shirakawa, and S. Kaneko, "Mechanisms of substrate transport-induced clustering of a glial glutamate transporter GLT-1 in astroglial-neuronal cultures," *European Journal of Neuroscience*, vol. 28, no. 9, pp. 1719–1730, 2008.

[50] J.-Y. Chatton, P. Marquet, and P. J. Magistretti, "A quantitative analysis of L-glutamate-regulated Na$^+$ dynamics in mouse cortical astrocytes: Implications for cellular bioenergetics," *European Journal of Neuroscience*, vol. 12, no. 11, pp. 3843–3853, 2000.

[51] E. Förster, S. Zhao, and M. Frotscher, "Laminating the hippocampus," *Nature Reviews Neuroscience*, vol. 7, no. 4, pp. 259–267, 2006.

[52] B. H. Gähwiler, M. Capogna, D. Debanne, R. A. McKinney, and S. M. Thompson, "Organotypic slice cultures: a technique has come of age," *Trends in Neurosciences*, vol. 20, no. 10, pp. 471–477, 1997.

[53] P. E. Kunkler and R. P. Kraig, "Reactive astrocytosis from excitotoxic injury in hippocampal organ culture parallels that seen in vivo," *Journal of Cerebral Blood Flow and Metabolism*, vol. 17, no. 1, pp. 26–43, 1997.

[54] I. E. Holopainen, "Organotypic hippocampal slice cultures: a model system to study basic cellular and molecular mechanisms of neuronal cell death, neuroprotection, and synaptic plasticity," *Neurochemical Research*, vol. 30, no. 12, pp. 1521–1528, 2005.

[55] M. Haber, L. Zhou, and K. K. Murai, "Cooperative astrocyte and dendritic spine dynamics at hippocampal excitatory synapses," *Journal of Neuroscience*, vol. 26, no. 35, pp. 8881–8891, 2006.

[56] H. Nishida and S. Okabe, "Direct astrocytic contacts regulate local maturation of dendritic spines," *Journal of Neuroscience*, vol. 27, no. 2, pp. 331–340, 2007.

[57] A. Buffo, C. Rolando, and S. Ceruti, "Astrocytes in the damaged brain: molecular and cellular insights into their reactive response and healing potential," *Biochemical Pharmacology*, vol. 79, no. 2, pp. 77–89, 2010.

[58] J.-H. Yi and A. S. Hazell, "Excitotoxic mechanisms and the role of astrocytic glutamate transporters in traumatic brain injury," *Neurochemistry International*, vol. 48, no. 5, pp. 394–403, 2006.

[59] C. Werner and K. Engelhard, "Pathophysiology of traumatic brain injury," *British Journal of Anaesthesia*, vol. 99, no. 1, pp. 4–9, 2007.

[60] G. Gegelashvili, M. B. Robinson, D. Trotti, and T. Rauen, "Regulation of glutamate transporters in health and disease," *Progress in Brain Research*, vol. 132, pp. 267–286, 2001.

[61] C. Escartin, E. Brouillet, P. Gubellini et al., "Ciliary neurotrophic factor activates astrocytes, redistributes their glutamate transporters GLAST and GLT-1 to raft microdomains, and improves glutamate handling in vivo," *Journal of Neuroscience*, vol. 26, no. 22, pp. 5978–5989, 2006.

[62] C. Vermeiren, M. Najimi, N. Vanhoutte et al., "Acute up-regulation of glutamate uptake mediated by mGluR5a in reactive astrocytes," *Journal of Neurochemistry*, vol. 94, no. 2, pp. 405–416, 2005.

[63] C. L. Poitry-Yamate, L. Vutskits, and T. Rauen, "Neuronal-induced and glutamate-dependent activation of glial glutamate transporter function," *Journal of Neurochemistry*, vol. 82, no. 4, pp. 987–997, 2002.

[64] P. M. Beart and R. D. O'Shea, "Transporters for L-glutamate: an update on their molecular pharmacology and pathological involvement," *British Journal of Pharmacology*, vol. 150, no. 1, pp. 5–17, 2007.

[65] F. D. Lima, M. A. Souza, A. F. Furian et al., "Na^+,K+-ATPase activity impairment after experimental traumatic brain injury: relationship to spatial learning deficits and oxidative stress," *Behavioural Brain Research*, vol. 193, no. 2, pp. 306–310, 2008.

[66] G. A. Gusarova, H. E. Trejo, L. A. Dada et al., "Hypoxia leads to Na,K-ATPase downregulation via Ca^{2+} release-activated Ca^{2+} channels and AMPK activation," *Molecular and Cellular Biology*, vol. 31, no. 17, pp. 3546–3556, 2011.

[67] S. S. L. Chew, C. S. Johnson, C. R. Green, and H. V. Danesh-Meyer, "Role of connexin43 in central nervous system injury," *Experimental Neurology*, vol. 225, no. 2, pp. 250–261, 2010.

[68] P. Nilsson, L. Hillered, U. Ponten, and U. Ungerstedt, "Changes in cortical extracellular levels of energy-related metabolites and amino acids following concussive brain injury in rats," *Journal of Cerebral Blood Flow and Metabolism*, vol. 10, no. 5, pp. 631–637, 1990.

[69] H. Katoh, K. Sima, H. Nawashiro, K. Wada, and H. Chigasaki, "The effect of MK-801 on extracellular neuroactive amino acids in hippocampus after closed head injury followed by hypoxia in rats," *Brain Research*, vol. 758, no. 1-2, pp. 153–162, 1997.

[70] H. Koizumi, H. Fujisawa, H. Ito, T. Maekawa, X. Di, and R. Bullock, "Effects of mild hypothermia on cerebral blood flow-independent changes in cortical extracellular levels of amino acids following contusion trauma in the rat," *Brain Research*, vol. 747, no. 2, pp. 304–312, 1997.

C Acknowledgement

Herewith I want to express my gratitude to Prof. Dr. Christine R. Rose to provide the opportunity to realize my doctoral thesis in her institute, for her guidance, encouragements and professional expertise, which were essential for the making of this work. I also want to thank Prof. Dr. Dieter Willbold for the revision of my work, giving me the possibility to defend my thesis. Furthermore I have to thank the DFG for funding the project.

I want to thank Prof. Dr. Olga Sergeeva for the provision of GFP-GFAP mice, and Prof. Dr. Carsten Korth and Dr. Alexander Müller-Schiffmann for the delivery of tgDimer mice.

I am indebted to Dr. Alexandra E. Schreiner and Dr. Julia Langer, whose data, published in Schreiner et al. (2013), are part of this work, as well as to Simone Durry and Claudia Roderigo for their professional support.

Of course, I want to thank Dr. Peter Hochstrate and Dr. Karl W. Kafitz for their constructive criticism on this work and the entire personnel for their help and all the unforgettable moments since beginning of my work at the Institute of Neurobiology.

My special thanks go to Nicole, for being my roommate and a good friend.

I finally want to thank my family and especially Julia for believing in me and for their patience especially during the final stages of my work. Without them, I could not have done this.

D Declaration

Die hier vorgelegte Dissertation habe ich eigenständig und ohne unerlaubte Hilfe angefertigt. Die Dissertation wurde in der vorgelegten oder in ähnlicher Form noch bei keiner anderen Institution eingereicht. Ich habe bisher keine erfolglosen Promotionsversuche unternommen.

Düsseldorf, den 23.03.2016

Eric Berlinger